Politecnico di Torino

ScuDo

Scuola di Dottorato ~ Doctoral School

WHAT YOU ARE, TAKES YOU FAR

Doctoral Dissertation

Doctoral Program in Electrical, Electronics and Communications Engineering (36th cycle)

Ge-on-Si photodetectors for silicon photonics: multiphysics modeling and design

Matteo G. C. Alasio

******

Supervisors:

Prof. Michele Goano, Supervisor

Dr. Marco Vallone, Co-supervisor

Prof. Francesco Bertazzi, Co-supervisor

Referees:

Prof. Giovanni Verzellesi, University of Modena and Reggio Emilia

Prof. Nicola Trivellin, University of Padova

Politecnico di Torino

June 14, 2024

This thesis is licensed under a Creative Commons License, Attribution - Noncommercial - No Derivative Works 4.0 International: see www.creativecommons.org. The text may be reproduced for non-commercial purposes, provided that credit is given to the original author.

I hereby declare that, the contents and organization of this dissertation constitute my own original work and does not compromise in any way the rights of third parties, including those relating to the security of personal data.

Matteo G. C. Alasio
June 14, 2024

Summary

In recent years, there has been a remarkable increase in the volume of information being transmitted, continuously expanding alongside the increasing complexity and quality of services offered to global users. The driving force behind this transformation has been the concept of *centralized computation*, where the majority of data processing takes place in data centers. These data centers are strategically located to handle the majority of traffic and subsequently deliver the processed data to end users. In this context, the importance of short-range interconnects is reaching a level equal to or greater than that of telecommunications, leading to a demand for effective and energy-efficient optoelectronic devices.

A fundamental limitation of this architecture is the boundary between the optical domain, which handles data communications, and the electrical domain, which focuses primarily on data processing. Until the technological feasibility of an all-optical computer is achieved, one of the most promising methods to overcome this limitation is through the use of silicon photonics (SiPh). SiPh provides a harmonious, cost-efficient, and completely CMOS-compatible integration of optical and electronic systems. Nevertheless, exploring new device ideas or improving current designs requires extensive and expensive prototyping efforts that involve multiple iterations.

The objective of this thesis is to create a computer-aided design framework for waveguide photodetectors that surpasses the current state of the art SiPh receiver. From a simulation perspective, it is challenging to deal with both the optical and electrical domains. This requires a multiphysics approach that involves solving Maxwell's equations and a carrier transport model. First, the spatially-resolved distribution of photogenerated carriers is determined by evaluating the absorbed photon density using a full-wave electromagnetic

simulation. Then, this distribution is used as a source term in an electrical simulation, which involves solving the electron and hole continuity equations with drift-diffusion constitutive relations, coupled to the quasistatic Poisson's equation.

The thesis is organized as follows:

- Chap. 1 introduces the goals set for the doctoral research at the beginning of the program. It then describes the context of silicon photonics, presenting its various components, and concludes with an explanation about waveguide photodetectors and their coupling configurations.
- Chap. 2 describes the operation of photodetectors. The crucial role played by these devices in converting the optical signal to the electrical signal is measured by figures of merit (or metrics) that are defined in this chapter. It is shown how the various figures of merit correspond to different measurable aspects of the device, such as the relationship between the input optical power and the electro-optical bandwidth. Also in this chapter are derived some simple analytical models, showing the main relationships between the electrical properties of materials, geometry, and figures of merit.
- Chap. 3 presents the state of the art of the photodetectors for silicon photonics that will be studied in the following chapters. The drift-diffusion model, the generation and recombination rates, and the Finite Difference Time Domain (FDTD) method, that are the main building blocks of the multiphysics simulation model, are then presented.
- Chap. 4 and Chap. 5 present the research results achieved for waveguide photodetectors having lateral and vertical configuration, where the difference is in the placement of silicon versus germanium. In fact, the vertical configuration has a contact on top of the Ge layer, while the lateral configuration has a fully intrinsic germanium absorber surrounded by two highly doped silicon regions. For both configurations, a study in dark is presented first, and then the performance under illumination and the device dynamics are addressed also through validation with experimental data. Chap. 6 finally presents the conclusions.

List of publications

Journal papers

[1] A. Tibaldi, J. A. Gonzalez Montoya, M. G. C. Alasio, A. Gullino, A. Larsson, P. Debernardi, M. Goano, M. Vallone, G. Ghione, E. Bellotti, and F. Bertazzi, "Analysis of carrier transport in tunnel-junction vertical-cavity surface-emitting lasers by a coupled nonequilibrium Green's function–drift-diffusion approach," *Phys. Rev. Appl.*, vol. 14, no. 2, p. 024037, Aug. 2020. doi: 10.1103/PhysRevApplied.14.024037

[2] M. Vallone, M. G. C. Alasio, A. Tibaldi, F. Bertazzi, S. Hanna, A. Wegmann, D. Eich, H. Figgemeier, G. Ghione, and M. Goano, "Exploring optimal dark current design in HgCdTe infrared barrier detectors: a TCAD and semianalytic investigation," *IEEE Photon. J.*, vol. 16, no. 1, p. 6800208, Feb. 2024. doi: 10.1109/JPHOT.2023.3345544

[3] M. G. C. Alasio, M. Vallone, A. Tibaldi, S. Namnabat, D. Adams, P. Gothoskar, F. Forghieri, G. Masini, F. Bertazzi, G. Ghione, M. Gioannini, and M. Goano, "TCAD-assisted progress on the Cisco platform towards low-bias 200 Gbit/s vertical-*pin* Ge-on-Si waveguide photodetectors," *J. Lightwave Technol.*, vol. 42, no. 9, pp. 3269–3276, May 2024. doi: 10.1109/JLT.2024.3352437

[4] M. G. C. Alasio, M. Zhu, M. Matsubara, M. Goano, and E. Bellotti, "*Ab initio* model of carrier transport in diamond," *Phys. Rev. Appl.*, vol. 21, no. 5, p. 054043, May 2024. doi: 10.1103/PhysRevApplied.21.054043

[5] D. Liu, L. F. Errico, M. G. C. Alasio, M. Zhu, and E. Bellotti, "Modeling the impact of fabrication variabilities on the performance of silicon

avalanche photodetectors," *IEEE Photon. J.*, vol. 16, no. 2, Apr. 2024. doi: 10.1109/JPHOT.2024.3393366

[6] M. Nicoletto, A. Caria, C. De Santi, M. Buffolo, M. G. C. Alasio, F. Mercinelli, X. Huang, H. Fu, H. Chen, Y. Zhao, G. Meneghesso, E. Zanoni, and M. Meneghini, "TCAD modeling and simulation of dark current-voltage characteristics in high-periodicity InGaN/GaN multiple-quantum-wells (MQWs) solar cells," *IEEE J. Photovoltaics*, vol. 14, 2024. doi: 10.1109/JPHOTOV.2024.3366710

Conference proceedings

[7] A. Palmieri, A. Shafiee, M. G. C. Alasio, A. Tibaldi, G. Ghione, F. Bertazzi, M. Goano, and M. Vallone, "Enhanced dynamic properties of Ge-on-Si mode-evolution waveguide photodetectors," in *20th International Conference on Numerical Simulation of Optoelectronic Devices (NUSOD 2020)*, online, Sep. 2020. doi: 10.1109/NUSOD49422.2020.9217719. ISBN 978-1-7281-6087-0 pp. 27–28.

[8] M. Vallone, M. Goano, A. Tibaldi, S. Hanna, D. Eich, A. Sieck, H. Figgemeier, G. Ghione, and F. Bertazzi, "Challenges in multiphysics modeling of dual-band HgCdTe infrared detectors," in *20th International Conference on Numerical Simulation of Optoelectronic Devices (NUSOD 2020)*, online, Sep. 2020. doi: 10.1109/NUSOD49422.2020.9217778. ISBN 978-1-7281-6087-0 pp. 19–20.

[9] M. G. C. Alasio, M. Goano, A. Tibaldi, F. Bertazzi, S. Namnabat, D. Adams, P. Gothoskar, F. Forghieri, G. Ghione, and M. Vallone, "Bias effects on the electro-optic response of Ge-on-Si waveguide photodetectors," in *IEEE Photonics Conference*, online, Oct. 2021. doi: 10.1109/IPC48725.2021.9592968. ISBN 978-1-6654-4676-1

[10] M. G. C. Alasio, M. Goano, A. Tibaldi, F. Bertazzi, S. Namnabat, D. Adams, P. Gothoskar, F. Forghieri, G. Ghione, and M. Vallone, "Ge-on-Si waveguide photodetectors: multiphysics modeling and experimental validation," in *21st International Conference on Numerical Simu-*

lation of Optoelectronic Devices (NUSOD 2021), online, Sep. 2021. doi: 10.1109/NUSOD52207.2021.9541424. ISBN 978-1-6654-4836-9 pp. 37–38.

[11] M. G. C. Alasio, M. Vallone, A. Tibaldi, F. Bertazzi, S. Namnabat, D. Adams, P. Gothoskar, F. Forghieri, G. Masini, G. Ghione, and M. Goano, "Modeling the frequency response of vertical and lateral Ge-on-Si waveguide photodetectors: Is 3D simulation unavoidable?" in *2022 Conference on Lasers and Electro-Optics (CLEO)*, San Jose, CA, May 2022. doi: 10.1364/CLEO_AT.2022.JW3A.28. ISBN 978-1-957171-05-0 p. JW3A.28.

[12] M. G. C. Alasio, P. Franco, A. Tibaldi, F. Bertazzi, S. Namnabat, D. Adams, P. Gothoskar, G. Masini, F. Forghieri, G. Ghione, and M. Goano, "3D multiphysics transient modeling of vertical Ge-on-Si *pin* waveguide photodetectors," in *22nd International Conference on Numerical Simulation of Optoelectronic Devices (NUSOD 2022)*, online, Sep. 2022. doi: 10.1109/NUSOD54938.2022.9894739. ISBN 978-1-6654-7898-4 pp. 5–6.

[13] M. G. C. Alasio, M. Zhu, A. Fronteddu, A. Cardinale, A. Ballarati, E. Bellotti, G. Ghione, A. Tibaldi, F. Bertazzi, M. Vallone, and M. Goano, "Modeling the electronic transport in FinFET-like lateral Ge-on-Si *pin* waveguide photodetectors for ultra-wide bandwidth applications," in *23rd International Conference on Numerical Simulation of Optoelectronic Devices (NUSOD 2023)*, Torino, Italy, Sep. 2023. doi: 10.1109/NUSOD59562.2023.10273560. ISBN 979-8-3503-1429-8 pp. 107–108.

[14] M. G. C. Alasio, P. Franco, A. Tibaldi, F. Bertazzi, S. Namnabat, D. Adams, P. Gothoskar, G. Masini, F. Forghieri, G. Ghione, and M. Goano, "Optical power screening effects in Ge-on-Si vertical *pin* photodetectors," in *Proceedings of SIE 2022. 53rd Annual Meeting of the Italian Electronics Society*, ser. Lecture Notes on Electrical Engineering, G. Cocorullo, F. Crupi, and E. Limiti, Eds. Cham, Switzerland: Springer Nature Switzerland AG, 2023, vol. 1005, pp. 155–159. ISBN 978-3-031-26065-0

[15] M. G. C. Alasio, M. Vallone, P. Molino, L. Errico, S. Hanna, H. Figgemeier, A. Tibaldi, F. Bertazzi, G. Ghione, and M. Goano, "Modeling the effects

of graded and abrupt mole fraction profiles in pBn and nBn HgCdTe barrier detectors," in *SPIE Optics+Photonics. Infrared Sensors, Devices, and Applications XIII*, vol. 12687, Proceedings of the SPIE, San Diego, CA, Aug. 2023. doi: 10.1117/12.2682206 p. 126870E.

[16] A. Tibaldi, A. Gullino, J. A. Gonzalez Montoya, M. G. C. Alasio, A. Larsson, P. Debernardi, M. Goano, M. Vallone, G. Ghione, E. Bellotti, and F. Bertazzi, "Modeling tunnel junctions for VCSELs: a self-consistent NEGF-DD approach," in *20th International Conference on Numerical Simulation of Optoelectronic Devices (NUSOD 2020)*, online, Sep. 2020. doi: 10.1109/NUSOD49422.2020.9217684. ISBN 978-1-7281-6087-0 pp. 67–68.

[17] M. Zhu, M. G. C. Alasio, and E. Bellotti, "Impact of fabrication variabilities on performance of avalanche photodetectors," in *23rd International Conference on Numerical Simulation of Optoelectronic Devices (NUSOD 2023)*, Torino, Italy, Sep. 2023. doi: 10.1109/NUSOD59562.2023.10273530. ISBN 979-8-3503-1429-8 pp. 109–110.

[18] M. Vallone, M. G. C. Alasio, A. Tibaldi, F. Bertazzi, S. Hanna, D. Eich, A. Wegmann, H. Figgemeier, G. Ghione, and M. Goano, "Different approximations for carriers lifetimes in HgCdTe quasi-neutral regions," in *23rd International Conference on Numerical Simulation of Optoelectronic Devices (NUSOD 2023)*, Torino, Italy, Sep. 2023. doi: 10.1109/NUSOD59562.2023.10273472. ISBN 979-8-3503-1429-8 pp. 25–26.

Book chapters

[19] M. Vallone, A. Tibaldi, F. Bertazzi, A. Palmieri, M. G. C. Alasio, S. Hanna, D. Eich, A. Sieck, H. Figgemeier, G. Ghione, and M. Goano, "Next-generation long-wavelength infrared detector arrays: Competing technologies and modeling challenges," in *Integrated Optics*, G. C. Righini and M. Ferrari, Eds. London: IET, 2020, vol. 2, ch. 9, pp. 265–294. ISBN 978-1-83953-343-3

Contents

List of Figures xi

List of Tables xx

1 Introduction, motivations and goals 1

1.1 Overview of silicon photonics 2

1.2 Waveguide photodetectors 7

2 Photodetectors and their metrics 13

2.1 Responsivity and quantum efficiency 18

2.2 Electro-optic (modulation) bandwidth 23

2.3 Circuit model and frequency response 25

2.4 Lateral vs vertical photodetectors: a matter of trade-offs 27

3 State-of-the-art and multiphysics modeling 31

3.1 Current status of WPDs 31

3.2 Drift-diffusion transport model 34

3.2.1 Generation and recombination rates 37

3.2.2 Mobility models 38

3.3 Finite-Difference Time-Domain method 39

3.4 Multiphysics model 42

4 Vertical *p-i-n* Ge-on-Si waveguide photodetectors 46

4.1 Device and geometrical quantities 47

4.2 Device in dark 48

4.3 Device under illumination 52

4.4 Validation of the model 57

4.5 Impact of implanted region 59

4.6 Electric field screening effect 59

4.7 Design guidelines 62

5 Lateral *p-i-n* Ge-on-Si waveguide photodetectors 66

5.1 Device in dark 68

5.2 Device under illumination 69

5.3 Ge width investigation 73

5.4 Carrier velocities and frequency response 75

6 Conclusions 80

References 82

Appendix A Semiconductor modeling 90

Appendix B Optical generation rate 98

Appendix C Material parameters 100

List of Figures

1.1 The different materials show a particular energy gap and a lattice constant based on the molar fraction chosen. Particularly, silicon and germanium can be used for wavelengths approximately up to 1.6 µm. This figure is taken from [1, Fig. 1.24]. 4

1.2 Qualitative Optical fiber attenuation in dB/km as a function of the wavelength λ, with enphasis on the main window for long range communications, i.e. O-band and C-band. 5

1.3 Example of different building blocks of a silicon photonics platform. Typical components are photodetector for optical-current conversion, modulators for modulating the optical signal,couplers and splitter for redirecting the light. Figure taken from [2]. . . . 6

1.4 Illustration describing the behavior of a *p*-*i*-*n* photodiode with qualitatively diagram of the band diagram, the net charge density and the electric field. This simple 1D device presents a uniform electric field across the intrinsic region, which is depleted under reverse bias condition. 8

1.5 On the left a typical photodetector with top illumination, which is absorbed exponentially in the absorber; on the right an evanescent coupling based on the input waveguide. The light is coupled with the absorption of the evanescent field in the absorber region. The lower plots report a qualitatively transversed averaged optical generation rate (typically expressed in $cm^{-3}s^{-1}$), along the light propagation direction. The optical generation rate represents the number of photogenerated carriers per unit volume and time. The top illuminated photodetector has the photogenerated carriers traveling in the same plane as the light propagation, while the evanescent coupled photodetector has the photogenerated carriers travelling in the transverse plane, orthogonal to the light propagation direction. 9

1.6 Possible configuration of WPDs. a) is a vertical configuration; b) and c) are two different variants of a lateral configuration. Blue, light blue and grey scale represent the doped silicon substrate. Figure taken from [2, Fig. 14]. 10

1.7 Perspective view of a waveguide photodetector. The input taper is employed for coupling the light from the input optical fiber; the output taper, that connects the waveguide to the silicon substrate, expand the mode to match the absorber width. Taken from [3, Fig. 1a]. 11

2.1 General structure of a communications network. A data center, server, or computer processes the signal, modulates it, and transmits it to the laser. An optical link, such as an optical fiber, transmits the light, which is then detected by a photodetector and turned back into digital information. 14

2.2 Qualitate electric field present in a 1D (a)p-i-n junction, and (b) a pn junction. 15

2.3 Schematic of e-h pair generation under incident light. The photon, with energy $E_{\text{ph}} = hf$ interact with the semiconductor promoting an electron from the top of the valence band to the minimum of the conduction band, leaving a hole behind. This process is its peak for $E_{\text{ph}} \approx E_g$. 16

2.4 Qualitatively correlation between output current and input optical power, for a given wavelength λ. For low input optical power the relationship is linear, with the slope defining the responsivity $\mathcal{R}$; while for $P > P_{\text{sat}}$ the output current remains constant. . . . 19

2.5 A photodetector exhibits responsivity $\mathcal{R}$ that varies with the energy of the photons of the incident light. The peak is present for photon energy $E_{\text{ph}} \approx E_g$, defining $\mathcal{R}_{\text{max}}$. As the photon energy increase the process lead to higher energy e-h pairs and it can lead to avalanche process as well. 22

2.6 Frequency response of a photodetector, normalized to the cutoff frequency. The response is similar (but not equal) to a low pass filter, and the electro-optic bandwidth is typically defined by the frequency f_{cutoff} for which the normalized response is equal to -3 dB. 23

2.7 Simplified circuit model of a photodetector, illustrating the key electrical components. The resistor R and the capacitor C_1 are intrinsic components of the device, with C_1 that can be approximated with a parallel plate capacitor. C_2 represents the parassitic external capacitor. 25

2.8 Analytic model implementing Eq. (2.28) and the *RC* simple model. H_{Ge} is used as an example of the width of the absorber region, with Ge referring to germanium, the material of the detector of the following chapters. The area is varying from low value (black curve) to high value (magenta curve), with significant reduction of the cutoff frequency. Dashed line in (a) represents the transit time limit, with the red dashed line indicating the maximum cutoff frequency; while dashed lines in (b) represnts the *RC* limitations of the cutoff frequency. This behavior is mainly due to the difference in the *RC* components and not to the transit time response. 29

3.1 PI curve and impulse response taken from [4]. This device is one of the first implementation and fabrication of Ge-on-Si photodetectors. 32

3.2 The device, taken from [5], is a device significantly different from common devices, with a lateral taper that evanescently couple the light to the absorber region. The space left between waveguide and absorber is a key factor to discribute the light along the device, allowing for high input optical powers. 33

3.3 (a) device structure and (b) frequency response for high power applications. Taken from [6]. 34

3.4 An innovative lateral *pin* waveguide Ge-on-Si photodetector, with fabrication (a) inspired by FinFET-like manufacturing processes. (b) The electro-optic frequency response shows an impressive cutoff frequency higher than 200 GHz. Taken from [7], this device will be used as reference structure in Chap. 5. . . 34

3.5 Perspective view of (a) the vertical waveguide photodetector, and (b) the lateral waveguide photodetector, studied in this dissertation. The computational box is also reported. The first copper metallic layer (orange) is connected with tungsten walls (light blue) to the silicon substrate and to germanium for the vertical case. Germanium is the central green block, with red and blue region indicating the p and n doping the the silicon substrate and at the germanium/top contact interface. 41

3.6 (a) normalized waveguide mode calculation for the input waveguide of the reference vertical photodetector presented in Chap. 4 (red rectangle), evaluated at the end of the taper with RSoft FullWave; (b) is a 1D horizontal normalized cut of (a) at the peak. 44

3.7 Schematic representation of the model used in TCAD Sentarus . 45

4.1 Perspective view of a vertical *p*-*i*-*n* waveguide photodetector. . 46

4.2 Transverse (xy, top) and longitudinal (yz, bottom) cross sections of the VPIN WPD structure under study with its most significant geometrical parameters. The Ge absorber is grown on top of the Si substrate; top and lateral metallic contacts are placed on the absorber and on the substrate, respectively. Ge is considered to be intrinsic (green), with the exception of a n^+ layer resulting from ion implantation below the Ge–metal contact (yellow), while Si is heavily *p*-doped (blue). A 40 µm-long tapered waveguide (not shown) injects light into the substrate. 48

4.3 Band diagram at equilibrium for reference device in (a) *p*-on-*n* (b) *n*-on-*p* configurations 50

4.4 Comparison of I-V characteristics in dark condition of p-on-n and n-on-p configuration. The blue curve, representing the p-on-n curve is lower than the orange n-on-p curve due to the difference in intrinsic carrier densities and the n-on-p graded interface. . . 51

4.5 Generation rates in dark of n-on-p configuration, avereged on the germanium region. The dominant effect is SRH, coincident with total rate, for the entire applied bias range by several order of magnitude 51

4.6 Real and imaginary part of the electrical small signal model evaluated with the model and fitting with an analytic model to extract R and C components. The circuit is reported in Fig. 4.7, with $R = 33\,\Omega, C_1 = 9.25\,\text{fF}, C_2 = 3.2\,\text{fF}$. 53

4.7 Small signal circuit model used to fit the numerical model. . . . 54

4.8 Experimental $I(V)$ characteristics of a sample of Device 2 (reference) in dark (blue line) and under 0 dBm illumination (orange line). 54

4.9 Optical generation rate $G_{\text{opt}}(x, y, z)$ ($\text{cm}^{-3}\text{s}^{-1}$) in the Ge absorber of Device 2 for an input optical power 200 µW. (Left) Transverse (xy) cross section for $z = 1.8$ µm, where z is measured from the beginning of the absorber. (Right) Longitudinal (yz) cross section for $x = 0$ (corresponding to the device center) and $z \in [0, 5]$ µm. 55

4.10 Magnitude of the electron drift velocity normalized with respect to the saturation velocity, $|v_n(x, y, z)|/v_{\text{sat}}$, in the transverse ($xy$) cross section of the Ge absorber of Device 2 at $z = 1.8$ µm for an input optical power 200 µW. (Left) -2 V bias voltage. (Right) Zero bias voltage. 55

4.11 Simulation (dashed blue curve) and measurements (black curves) of five nominally identical samples of reference device, for a bias voltage of -2 V. 56

4.12 Experimental values of f_{cutoff} as a function of the bias voltage for the six device variants whose geometry is reported in Table 4.2 (dashed lines), compared with the corresponding simulated curves obtained with calibrated P_{tot} (black solid lines). The horizontal red dashed lines correspond to the (bias-independent) transit-time limit according to the closed-form model of [1, Sec. 4.10.1]. 58

4.13 Variation of the electro-optical bandwidth as a function of the extension (width) of the germanium implanted region W_{doping}, for fixed doping implantation height $H_{\text{Ge}} = 50\,\text{nm}$ and two bias voltages. Both the $-0.8\,\text{V}$ (black) and $-2\,\text{V}$ (blue) curve shows significant bandwidth drop close to $W_{\text{doping}} = 3\,\mu\text{m}$. 60

4.14 Electro-optic cutoff frequency as a function of the optical power measured at the laser output. 60

4.15 Magnitude of the electric field in Ge along a 1D vertical cut between the center of the top metal contact and the silicon waveguide, at a distance of 1 µm from the front section of the absorber. 61

4.16 Dependence of f_{cutoff} on (a) W_{Ge} and (b) H_{Ge}, starting from Device 2 (vertical dashed-dotted line), for input optical power 200 µW and bias voltage $[-2, -1, 0]\,\text{V}$. The upper bound provided by the transit-time limit [1, Sec. 4.10.1] is reported as a reference (red dashed line). 64

4.17 Dependence of $\mathcal{R}$ on (a) W_{Ge} and (b) H_{Ge}, starting from Device 2 (vertical dashed-dotted line), for input optical power 200 µW and bias voltage $-2\,\text{V}$. On the present plot, the values of $\mathcal{R}$ at lower bias ($-1\,\text{V}$ and $0\,\text{V}$) would be superimposed to the reported data points. 65

5.1 Cross section of the lateral Ge-on-Si photodetector. The light is coupled with the absorber like for the vertical case, i.e. with a waveguide connected with a taper to the silicon substrate. . . . 67

5.2 Band diagram at equilibrium of the device in a 1D cut evaluated in 1D cut along the (n)silicon-germanium-(p)silicon junctions. (a) without graded interfaces, (b) adding a small linearly interpolated graded profile. The introduction of the graded profile remove the valence band discontinuity at $x \approx -50\,\text{nm}$, improving convergence. The other region are not affected by the graded region. 69

5.3 IV characteristics of the device simulated compared with [7] data. A difference of several orders of magnitude are present, but comparing with Fig. 5.4, it is clear that defects not included in the model are the responsible for the difference. 70

5.4 Generation and recombination rate evaluated in 1D cut along the (n)silicon-germanium-(p)silicon junctions under -2 V of applied bias. Solid lines represent recombination contribution, while dashed lines represents generative contribution. The depleted germanium shows high values of SRH generation, indicating that is the main actor also in the contribution of the IV curve. 70

5.5 Longitudinal cross section for the optical generation rate, with (top) a lateral cut, and (bottom) a top cut, aligned on the same axis.Even if there is an higher concentration of photogenerated carriers, the rate is distributed vertically and longitudinally more evenly with respecto to the VPIN. 71

5.6 PI curve for a bias of -2 V compared with data from [7]. The difference between the simulation and the measurement is dependent on the sensitivity of germanium to the absorption coefficient close to the cutoff of $\lambda = 1.55\,\mu m$. 72

5.7 Electro-optic frequency response at $V_{bias} = -2$ V compared with the literature [7]. The simulated response fit the measured data up to the cutoff frequency $f_{cutoff} \approx 265$ GHz. Despite the noise superimposed to the measurements, due to the ultrawide bandwidth of the device, make hard to extract the exact cutoff frequency. Simulation are performed at $\lambda = 1.31\,\mu m$ and $\lambda = 1.55\,\mu m$ but no significant difference has been observed, due to the low responsivity values and the strong dependance on the saturation velocity (indipendent of the wavelength). 73

5.8 Comparison on the quantum efficiency vs the Ge width. 74

5.9 Cutoff frequency as a function of the width of the device. 75

5.10 Quantum efficiency η as a function of the width of the device. . 76

5.11 Frequency response with different v_{sat} applied. 76

5.12 Cutoff frequency as a function of v_{sat}, set equal for electrons and holes. 77

5.13 Monte Carlo simulation of carriers in devices, comparing two cases fof electron and holes to the saturation velocity of drift diffusion. (a) electrons, (b) holes. 79

A.1 Electronic band structure of diamond, evaluated with DFT. . . . 91

A.2 Qualitative plot of the dependence of the density of states with respect to energy. 92

A.3 Fermi-Dirac Statistic for electrons with different temperature as a function of the difference between the energy of the particle and the Fermi level E_F. 93

A.4 Intrinsic carrier density for Silicon as a function of the temperature 95

List of Tables

3.1 Responsivity and cutoff frequency of representative VPIN and LPIN devices. 35

3.2 Typical computational costs for LPIN and VPIN, with cell size for uniform mesh of the FDTD method. 44

4.1 Summary of geometrical parameters of the reference device . . . 49

4.2 Geometrical parameters of the devices under study (see Fig. 4.2). Device 2 corresponds to the nominal geometry (reference). For all devices, $L_{\mathrm{Ge}} = 15\,\mu\mathrm{m}$ and $H_{\mathrm{Ge}} = 0.8\,\mu\mathrm{m}$, except for Device 6 where $L_{\mathrm{Ge}} = 18.5\,\mu\mathrm{m}$. The last column reports the simulated responsivity at a bias voltage of $-3\,\mathrm{V}$ and input optical power $200\,\mu\mathrm{W}$. 57

5.1 Main geometrical quantity 67

C.1 Material parameters for silicon and germanium in the drift-diffusion model 100

C.2 Wavelength, refractive index (n), and extinction coefficient (k) of Ge. 100

Chapter 1

Introduction, motivations and goals

The present chapter introduces the main motivations and the research goals addressed in this dissertation. The chapter also provides an overview of silicon photonic (SiPh) applications and of the research context.

The title of the dissertation may suggest several questions. Why is silicon photonics important, and how is it evolving? How the study of a single building block of the communications system, namely the photodetector in the receiver, may improve the current state of the art? Why to choose a multiphysics modeling approach? And what are the model primary applications? These are examples of the questions that this chapter will try to address.

The understanding of transport of photogenerated carriers in Ge-on-Si waveguide photodetectors (WPDs, introduced in Sec. 1.2), the development of a multiphysics model and the optimization of WPD design have been the main focus of my PhD activity and are the topics of this dissertation, that discusses the intricacies of the dynamic behavior of SiPh photodetectors and the prediction of the performance of conventional and novel WPD structures. This research activity received partial support from Cisco Systems[1], under the Sponsored Research Agreements TOSCA, CONCERTI and STACCATO, that also performed the measurements on the vertical devices presented in Chap. 4.

[1]Cisco Systems, Inc., San Jose, CA 95134, USA

1.1 Overview of silicon photonics

Silicon photonics is a broad industrial and academic research field that aims to leverage silicon technology towards the integration of photonic components, such as lasers, optical modulators, optical waveguides and photodetectors.

Instead of directly attempting an overview of silicon photonics, I will start with a brief bottom-up approach, providing some information regarding the purpose and operation of a photodetector, then contextualizing it within the other building blocks of the communication chain typically used in silicon photonics.

Photodetectors are photonic components that convert an optical signal into an electrical signal. The main applications of photodetectors are in communications and sensing. In communications, the information obtained from the electrical signal is subsequently decoded and processed by an electronic system, such as a digital signal processor (DSP). Fiber-optic long-range data links and intra-data center optical networks are just two important examples of this class of applications. In sensing, photodetectors are employed to detect the presence and intensity of light, down to the level of individual photons, for e.g. medical, industrial, security and environmental imaging and monitoring.

Silicon photonics deals primarily with communications, and the main difference between a conventional device and a silicon photonic device is the capability of the optoelectronic device to be integrated within CMOS compatible electronics. The emphasis of the present study pertains to a particular category of detectors based on germanium (Ge) as light-absorbing material. These devices are typically called Ge-on-Si photodetectors, referring to Ge being grown on top of a silicon wafer, and find their most common application in the field of integrated optics. Quantum communications with quantum key distribution, data centers, long-distance communications, and high-performance computing are a few of many that employ these photodetectors.

One can use several crucial metrics, also known as figures of merit, to evaluate a photodetector performance. These metrics comprise responsivity, quantum efficiency, and electro-optical bandwidth (or modulation bandwidth or simply bandwidth), and they are defined in Chap. 2. To facilitate the advancement of new semiconductor device generations, it is important to

enhance at least one of the metrics. In the field of communications, responsivity and modulation bandwidth are the most crucial, under the assumption of a good signal-to-noise ratio (or, equivalently, a low dark current). Indeed, the estimation of the photodetector “sensitivity” is based on the responsivity, which is defined as the ratio of input power to output current, expressed in A/W; while the photodetector “speed” is the modulation bandwidth, denoted by the $-3\,\mathrm{dB}$ [2] bandwidth and represents the highest light modulation frequency that the photodetector can accurately track. Typically, the $-3\,\mathrm{dB}$-bandwidth is also referred to as the cutoff frequency.

The photodetector active region, which is responsible for light absorption, is composed of semiconductors, and it is manufactured using an extensive range of materials, such as those classified as III-V, II-VI, and IV-group semiconductors. Choosing the material implies choosing the energy gap E_g and the wavelength λ range of the light that the photodetector is able to detect. The relation than links the range of wavelength that can be absorbed and the energy gap is:

$$E_\mathrm{g} \propto \frac{1}{\lambda}. \tag{1.1}$$

On the other hand, the performance of the material and the requirements of the application determine the fabrication process of photodetectors; in other words, distinct materials are used for distinct applications.

Fig. 1.1 shows the majority of the semiconductors and alloys used today in the semiconductor fabrication process. Si and Ge photodetectors are among the IV materials used in visible and near-infrared applications. InGaAs and InP photodetectors are two examples of III-V materials utilized in photonics, while II-VI materials include HgCdTe photodetectors that are utilized for infrared sensing.

Compatibility with the manufacturing process and integration with silicon-based electronic devices are two of the most important considerations when selecting the material for silicon-based photonics, defining the name silicon photonic.

The wavelength absorption range is chosen according to the application as well, and for instance, long-distance and data center communications generally

[2] rarely $-10\,\mathrm{dB}$

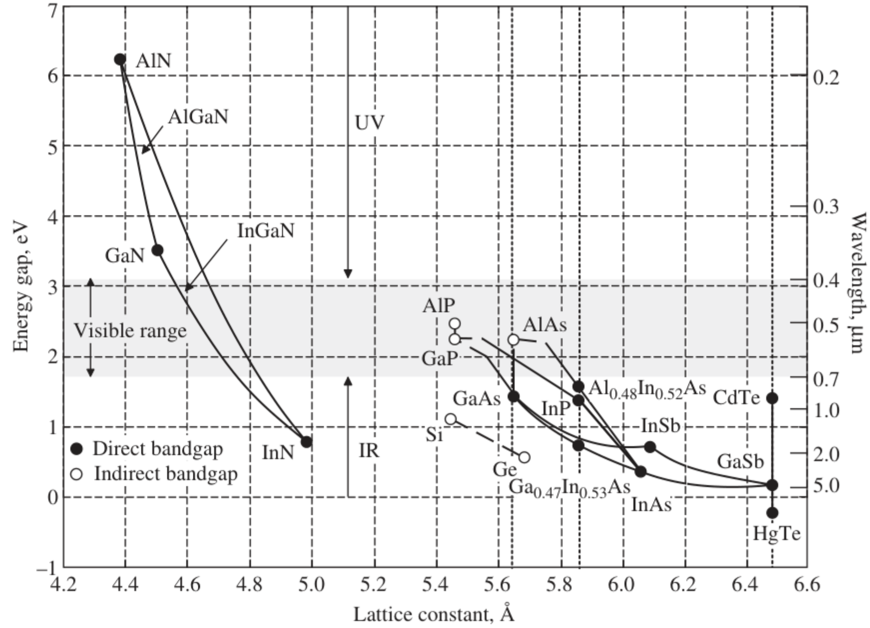

Fig. 1.1 The different materials show a particular energy gap and a lattice constant based on the molar fraction chosen. Particularly, silicon and germanium can be used for wavelengths approximately up to 1.6 µm. This figure is taken from [1, Fig. 1.24].

work within the wavelength range of 800 nm to 1.6 µm [8], with a specific emphasis on the O-band (with its center at 1.31 µm) and C-band (with its center at 1.55 µm). These bands are the most suitable for low optical loss in optical fibers, as shown in Fig. 1.2, which report the qualitatively attenuation spectrum for a generic optical fiber and show three minima, defining the so-called transmission windows.

Silicon photonics technology was created so that photonic technology could be used with silicon technology that was already in use [9–12]. With the need for faster communications, it became important to make photonic devices that can be completely built and integrated into the silicon platform. The technological advancements comprise waveguides, switches, photodetectors, and modulators, with Fig. 1.3 providing an illustration of various components forming a silicon photonics platform [2], while an example of the cross section of the detector is shown in Fig. 1.6.

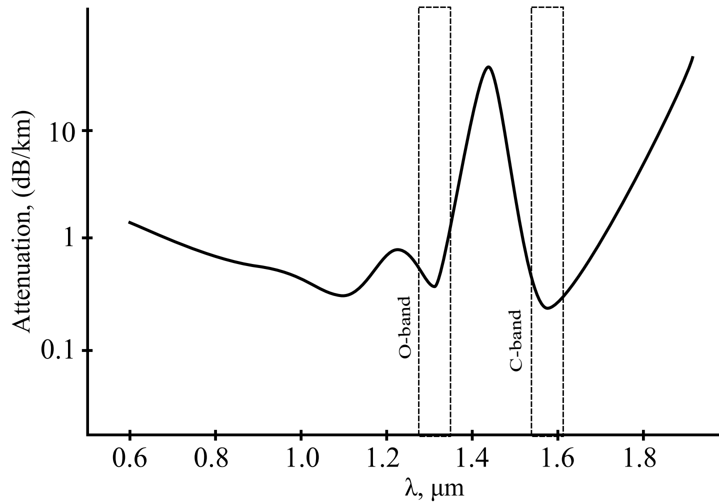

Fig. 1.2 Qualitative Optical fiber attenuation in dB/km as a function of the wavelength λ, with enphasis on the main window for long range communications, i.e. O-band and C-band.

In the past few years, germanium has become the standard material for photodetectors in the O and C bands. This is due to important improvements in the manufacturing process made by researchers such as Tada *et al.* (2010) [13] and Lim *et al.* (2014) [14]. They allow for lower-cost fabrication processes, and a fully integrated solution is easier to fabricate in complex electronic systems, extending the functionalities to their photonic capabilities.

In the last few years, a considerable quantity of research and development has been devoted to this field, with universities, companies, and researchers collaborating to advance the technology, and a literature review on Ge-on-Si photodetector, necessary for this work, is reported in Sec. 3.1. But, according to some forecasts, silicon photonic is expected to expand significantly over the coming years, The forecast taken from [15] refers to the silicon photonic market in the upcoming years, until 2030, and it showcases an industrial expansion in the next year, particularly in HPC, datacenters, and communications, motivating further research.

Specifically for photodetectors, the aim of silicon photonic research is to develop a device that has the potential to achieve a bit rate of 200 gbit/s and a bandwidth exceeding 60 GHz and beyond (see [7, 16, 17]). This is expected to be accomplished with few compromises on responsiveness and dark current. The demand for the next generation of data centers also requires innovation

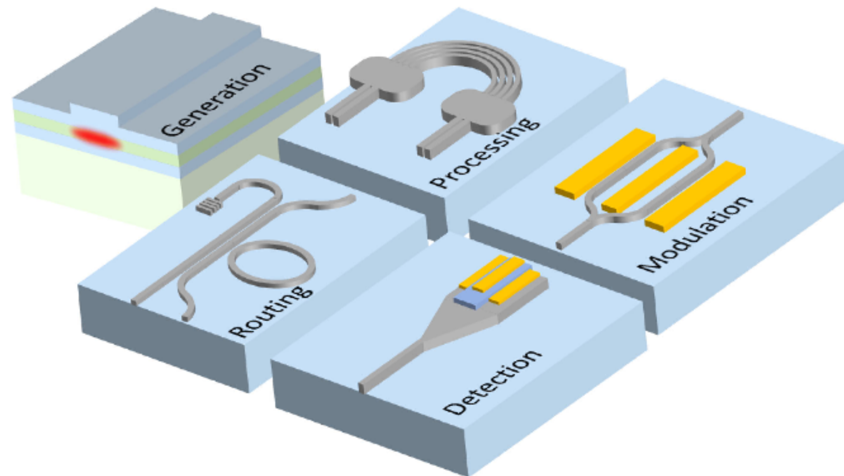

Fig. 1.3 Example of different building blocks of a silicon photonics platform. Typical components are photodetector for optical-current conversion, modulators for modulating the optical signal,couplers and splitter for redirecting the light. Figure taken from [2].

in the communication chain, with datacenters facing a growing volume of data processing due to the proliferation of cloud services driven by artificial intelligence, machine and deep learning, social media, cloud computing, and big data. Hence, it became significant to explore new possibilities like emerging photonic devices and silicon photonics, particularly in the context of advancing the next generation of data centers by significantly enhancing the bandwidth (or "speed") of photodetectors. This upgrade could potentially impact most of the optical link, and it has the capacity to considerably decrease power consumption and resource requirements associated with data center expansions and development.

My contributions to the field The motivation that has directed my research towards the Ge-on-Si waveguide photodetector is the requirement for a device that can be completely integrated into silicon with high responsivity and the largest bandwidth. This thesis describes and validates my goal to build a model for the multiphysics simulation of photodetectors, taking into account the complex electronic transport occurring within Ge-on-Si technology and the link with the optical world. A number of models for simulating the electronic transport in Ge-on-Si photodetectors have been published in the literature (e.g., [18]); however, only a limited number of these models can

accurately represent the multiphysics complexity in Ge-on-Si photodetectors. The implementation of a multiphysics model also presents challenges. To understand the photodetector parasitic effects and the input optical waveguide complex light coupling, one needs to use 3D simulations as well as Maxwell equations and electronic transport equations. The industrial sector is in need of a reliable framework to simulate and predict the photodetector performance, but using electronic transport models alone is inadequate, as is considering optical propagation within the device alone. By devoting research efforts to the development of a multiphysics model that accounts for electronic transport in Ge-on-Si photodetectors and a complete optical propagation model, progress is made in the field.

1.2 Waveguide photodetectors

This section provides an overview of the waveguide Ge-on-Si photodetectors and shows specific applications in which the integrated waveguide can be advantageous.

In this dissertation, all the devices will be p-i-n junctions, and Fig. 1.4 shows the qualitative behavior of the device.

Saleh *et al.* (2019) [19] report the benefits of using p-i-n photodiodes:

- The length of the device (intrinsic) depletion layer increases the region available for light absorption, where drift currents may extract the generated carriers.
- The RC parassitic components decrease as the depletion layer width increases, lowering the junction capacitance. Nevertheless, when the depletion layer widens, the transit time also lengthens.
- Decreasing the ratio of the device diffusion length to drift length causes more of the generated carriers to experience a more rapid drift process.

Waveguide photodetectors place a dielectric (in SiPh, silicon) waveguide next to the intrinsic region. The waveguide is not directly injecting light into the absorber (butt-coupling), but the light is evanescenlty coupled, reducing

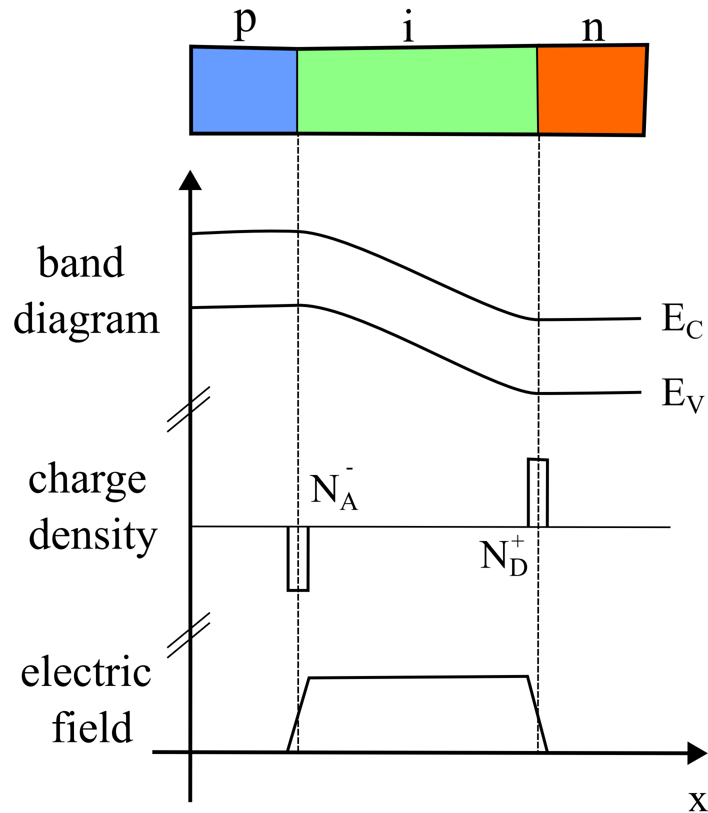

Fig. 1.4 Illustration describing the behavior of a *p*-*i*-*n* photodiode with qualitatively diagram of the band diagram, the net charge density and the electric field. This simple 1D device presents a uniform electric field across the intrinsic region, which is depleted under reverse bias condition.

coupling losses and/or optical power screening. Evanescent wave coupling in waveguides is defined as the coupling between two waveguides due to the overlap of evanescent fields of the propagating waves. Coupling between the silicon dielectric waveguide and the germanium absorber is obtained by placing the silicon waveguide aside from the germanium absorber so that the evanescent field propagated in the waveguide excites a wave in the germanium, absorbing it. Typical device designs include a photodiode positioned on top of a waveguide (silicon waveguide or substrate) and are suitable for being integrated into photonic circuits [19]. Fig. 1.5 reports a illustration with the configuration of illumination. ON the left the traditional illumination from the top of

the photodetector; on the right the evanescent coupling with input optical waveguide.

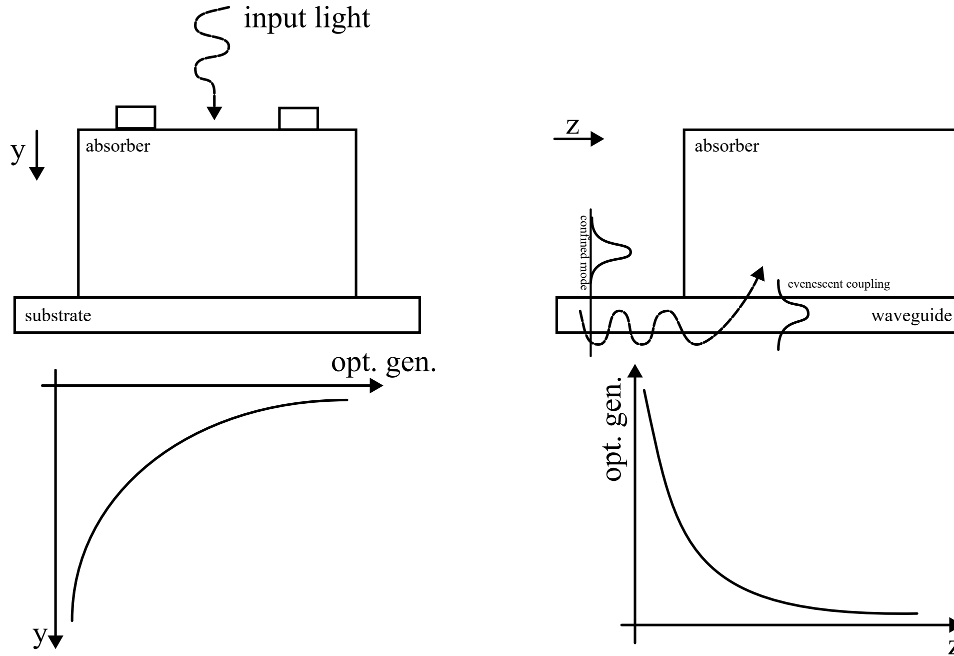

Fig. 1.5 On the left a typical photodetector with top illumination, which is absorbed exponentially in the absorber; on the right an evanescent coupling based on the input waveguide. The light is coupled with the absorption of the evanescent field in the absorber region. The lower plots report a qualitatively transversed averaged optical generation rate (typically expressed in $cm^{-3}s^{-1}$), along the light propagation direction. The optical generation rate represents the number of photogenerated carriers per unit volume and time. The top illuminated photodetector has the photogenerated carriers traveling in the same plane as the light propagation, while the evanescent coupled photodetector has the photogenerated carriers travelling in the transverse plane, orthogonal to the light propagation direction.

Ge-on-Si waveguide photodetectors (WPDs) are important parts of silicon photonics (SiPh), which makes it easier to combine electrical and photonic functions on a single silicon platform. WPDs are known for their high responsivity and quantum efficiency, which are crucial steps in the process of optical-electrical signal transmission. Their fast response makes them essential for applications that require large bandwidth. Furthermore, their integration with other photonic components on silicon substrates allows for the creation of small, cost-efficient optical systems that align with the objective of reducing the size of current electronics [20]. There are two main configurations of waveguide Ge-on-Si photodetectors: lateral (LPIN) and vertical (VPIN). The distinction

between the two is given by the placement of germanium with respect to the dopants. Fig. 1.6 shows a schematic of the possible configuration. The lateral configuration means that either germanium is doped and photogenerated carriers move between the n and p doped regions in a lateral direction, or germanium is intrinsic and silicon is doped around it. Vertical configuration implies that germanium is doped on top and that the transport of photogenerated carries occurs from top to bottom.

Chap. 4 will discuss my research on VPINs, while Chap. 5 will discuss my research on LPINs.

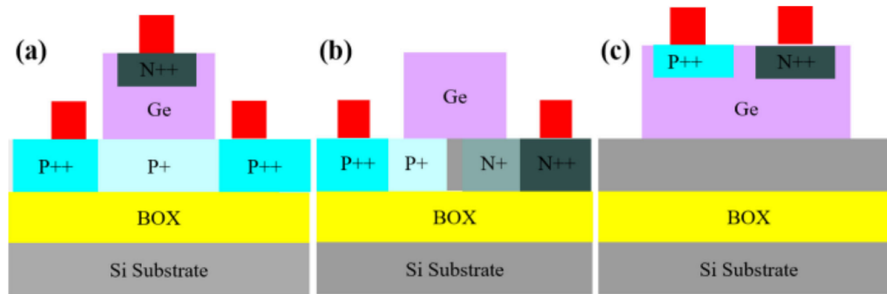

Fig. 1.6 Possible configuration of WPDs. a) is a vertical configuration; b) and c) are two different variants of a lateral configuration. Blue, light blue and grey scale represent the doped silicon substrate. Figure taken from [2, Fig. 14].

The compatibility between WPDs and CMOS production demonstrates their technological synergy, enabling them to utilize the innovations and scalability of semiconductor manufacturing. This compatibility not only decreases the costs linked to WPD production but also simplifies their integration into current electronic circuits, promoting a connection between the fields of photonics and electronics [21].

Various fields have utilized WPDs, each benefiting from their unique characteristics. Within data centers, where there is a growing need for fast data transmission, WPDs offer an energy-efficient option that decreases the need for power-hungry electronic connections. Wavelength-division multiplexing devices have the capability to transform optical signals from fiber optics into electrical signals, with channels divided in wavelengths, which are crucials for facilitating fast and long-range communication. This is particularly important for the core of worldwide networking infrastructures [22]. Furthermore, sensing

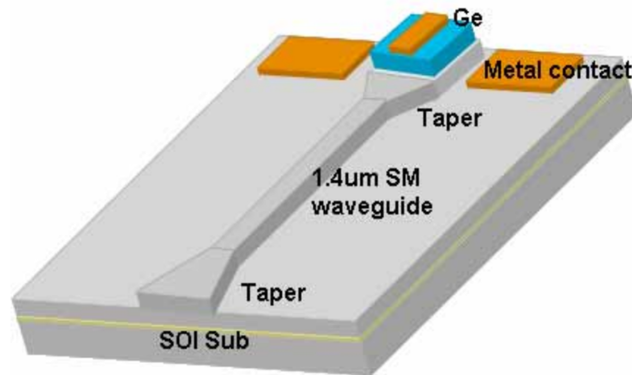

Fig. 1.7 Perspective view of a waveguide photodetector. The input taper is employed for coupling the light from the input optical fiber; the output taper, that connects the waveguide to the silicon substrate, expand the mode to match the absorber width. Taken from [3, Fig. 1a].

and metrology applications currently use WPDs. Their incorporation into photonic sensors enables detailed environmental monitoring and sophisticated biomedical diagnostics. WPDs are well-suited for these applications due to their high detectivity and speed, which are important for accurate detection. [23, 24] Finally, the relevance of WPDs in quantum computing and cryptography industries is fascinating. The capacity to detect individual photons is crucial in these applications, thanks to avalanche photodetectors, since it forms the basis for the functionality of secure quantum communication protocols.

Fig. 1.7 reports an a perspective view of a waveguide photodetector, with two taper at the beginning of the waveguide and before the input of the device. WPDs, due to their high quantum efficiency and operational speed, play a crucial role in extracting quantum information, thereby enabling quantum computation and error correction methods.

However, the progress of WPDs is not without obstacles. Relentless innovation is required to enhance even more the absorption efficiency of photonic circuits, ensuring maximal photon capture. Additionally, expanding their bandwidth to accommodate higher data rates and enhancing their integration density for more compact and sophisticated circuits are other crucial areas of focus. Upcoming research will investigate new materials, such as two-dimensional ma-

terials or nanostructured compounds, as well as sophisticated design processes that may involve complex nanostructures or hybrid integration approaches. These advances strive to surpass the current performance restrictions of WPDs, allowing for new possibilities and capabilities in SiPh.

WPDs are positioned at the intersection of fast communication, sensing, and quantum technologies. Their ongoing development, propelled by technological progress and rising application needs, highlights their crucial role in advancing integrated photonic systems. SiPh is continuously advancing the combination of photonic capabilities and electronic integration. Within this field, wavelength division multiplexers (WDMs) play a crucial role in driving its advancement. They are vital in creating the future of optical communication solutions and extending their impact to other areas as well.

Chapter 2

Photodetectors and their metrics

This chapter presents a summary of topics related to photodetectors and describes the performance metrics used later in the dissertation. I avoid making formal derivations of the quantities. Instead, I will simply outline the definitions and equations required for comprehending the concepts that will be necessary in the following chapters. The derivations and inspiration for this chapter are taken from [1, Ch. 1-4] and they will be frequently cited. Appendix A will conclude the discussion on semiconductor transport, including details on the mathematical model and some comments on heterostructures.

The diagram in Fig. 2.1 illustrates a general communications system and indicates the function of the photodetector in the communication network. To get insight into the functions of photodetectors in a generic communication system, I will begin by examining the fundamental elements of an optical communication system.

An optical communication system has essential components:

- The transmitter converts digital data from a system, such as a microprocessor or microcontroller, into an analog signal to modulate a light source, such as a laser. A modulator can be utilized to modulate the light.
- The link implements typically optical waveguides or optical fibers. It allows for guided light transmission from the transmitter to the receiver input port.

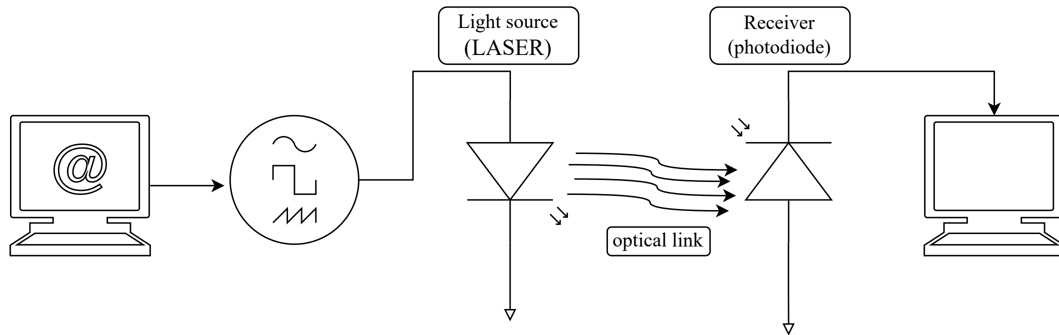

Fig. 2.1 General structure of a communications network. A data center, server, or computer processes the signal, modulates it, and transmits it to the laser. An optical link, such as an optical fiber, transmits the light, which is then detected by a photodetector and turned back into digital information.

- The receiver transforms modulated light into an electric current, conveying the information. This is where the photodetector is located, photogenerating carriers under incident light. This interaction results in the generation of electron-hole pairs, which collectively contribute to the overall current. A schematic representation of this process is depicted in Fig. 2.3. In subsequent blocks, high-speed electronic components like amplifiers and decoders process the photogenerated current.

The transmission process has several bottlenecks, one of which is the photodetector bandwidth. Therefore, photonic integrated circuit designers have the need for photodetectors with wide bandwidth. Photodetectors can be fabricated in various layouts, including simple *pn* junctions, *p*-*i*-*n* junctions and phototransistors. These examples represent only a fraction of the potential layouts documented in the literature. The photodetectors being examined in this study are all based on *p*-*i*-*n* junctions. The intrinsic *i*-region is used to create a wide electric field within the device active region, possibly enabling the photogenerated carriers to reach their saturation velocities and to be efficiently extracted. The electric field of a *p*-*i*-*n* junction is qualitatively represented in Fig. 2.2a. In contrast, the qualitative electric field of a simple *pn* junction is reported in Fig. 2.2b.

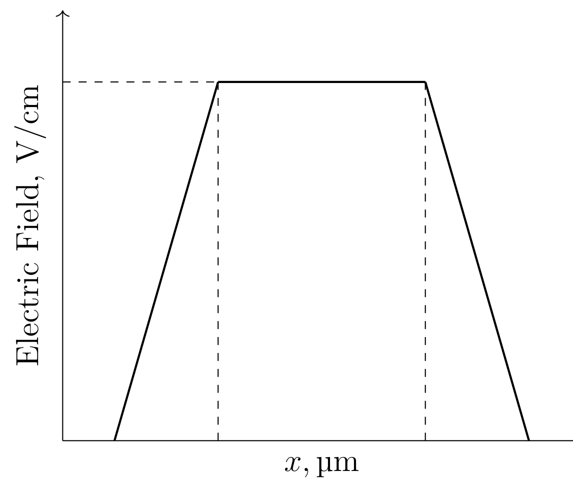

(a) Qualitative plot of the electric field in a *p*-*i*-*n* Junction.

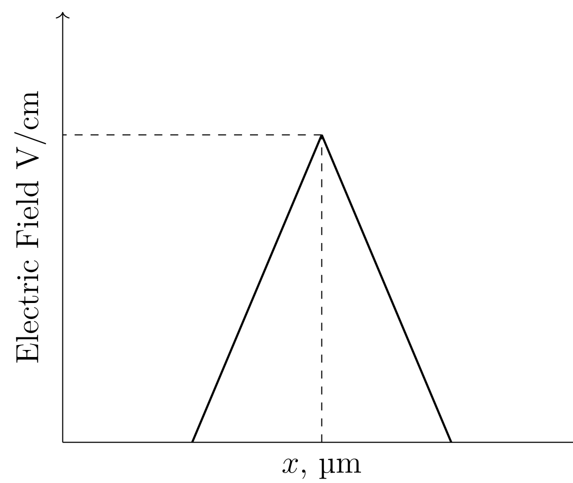

(b) Qualitative plot of the electric field in a p-n Junction.

Fig. 2.2 Qualitate electric field present in a 1D (a)*p*-*i*-*n* junction, and (b) a *pn* junction.

The cutoff wavelength of the absorption spectrum of a crystalline semiconductor is determined by its energy gap as [1]

$$E_\mathrm{g}[\mathrm{eV}] = hf = \frac{hc_0}{\lambda} \approx \frac{1.24}{\lambda[\mu\mathrm{m}]}. \tag{2.1}$$

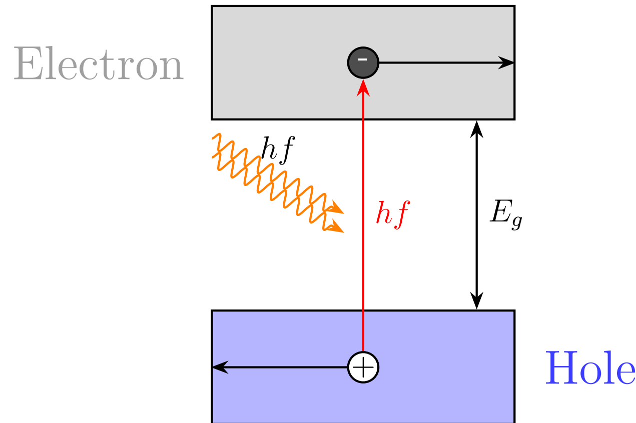

Fig. 2.3 Schematic of e-h pair generation under incident light. The photon, with energy $E_{\mathrm{ph}} = hf$ interact with the semiconductor promoting an electron from the top of the valence band to the minimum of the conduction band, leaving a hole behind. This process is its peak for $E_{\mathrm{ph}} \approx E_g$.

Based on this equation, the photon-semiconductor interactions can be divided into three scenarios related to the values of E_{ph} (or λ) and the energy gap E_{g}:

- If $E_{\mathrm{ph}} < E_{\mathrm{g}}$, then the photon does not have enough energy to promote an electron to the conduction band.
- If $E_{\mathrm{ph}} \gtrsim E_{\mathrm{g}}$ the interaction between light and matter is significant. Photons have enough energy to promote electrons from the valence band to the conduction band, leading to and electron and hole pair.[1] The generation process is a photon absorbed, while during a recombination process, a photon is emitted.
- If $E_{ph} \gg E_g$ leading to high energy interaction between the photons and the semiconductor. In this situation the photon can generate a high-energy electron-hole pair.

These interaction can be associated with different generation-recombination processes, described as:

- **Photon absorption**, the process used by photodetectors, generates an electro-hole pair. An electron in the valence band absorbs energy

[1] The extra energy is lost due to thermalization effect

through an interaction, causing it to transition to the conduction band, while simultaneously creating a hole (a positive charge) in the valence band. Due to the energy exchange, the amplitude and power of the electromagnetic wave diminish during the process.

- **Photon emission**, divided in two categories
  - *stimulated* emission is the process of recombination between an electron and a hole in a semiconductor. During this process, a photon interacts with the semiconductor and causes the emission of another photon with the same frequency and wavevector as the original photon. The new photon exhibits coherence with the initial one, meaning that it enhances both the amplitude of the field and the power. This is a gain process.
  - *spontaneous* emission occurs when an electron and a hole recombine, resulting in the emission of a photon. It differs from the stimulated case since it is not connected with another photon and it is incoherent, not increasing an existing wave.

Summarizing, absorption and emission are essentially the same process, but the time axis is reversed: in the absorption process, a photon is transformed into an electron-hole pair, whereas in stimulated emission process, an electron-hole pair is transformed into a photon.

This explanation of the interaction between light and semiconductors forms the basis for the metrics related to absorption. In fact, the performance of photodetector is optimized when it efficiently captures and extracts the electron-hole pairs generated by incident light in the device. Hence, to compare the effectiveness of different photodetector designs, the comparison is done with specific metrics.

The photodetector can be fully characterized by the following constitutive relation, takihng into account the wavelength λ, the input opticcal power $p_{\mathrm{in}}(t)$, the detector bias voltage $v_{\mathrm{PD}}(t)$, assuming constant temperature T:

$$i_{\mathrm{PD}}(t) = f\left(p_{\mathrm{in}}(t), v_{\mathrm{PD}}(t); \frac{\mathrm{d}}{\mathrm{d}t}, \lambda\right) \tag{2.2}$$

The temperature in communication applications is typically uniform within the device, since the typical input optical power reaching the device are close to 100 µW, resulting in a low power density.

with the expression for the output current i_{PD} is:

$$i_{\mathrm{PD}} = i_{\mathrm{L}} + i_{\mathrm{d}}. \tag{2.3}$$

Eq. (2.2) describes the input optical power $p_{\mathrm{in}}(t)$ at a specific wavelength λ and applied bias $v_{\mathrm{PD}}(t)$ to the output current i_{PD}. The output current consists of the photocurrent i_{L} and the dark current i_{d}, i.e., the reverse saturation current of the diode. If the input optical signal varies slower than the device electrical cutoff frequency, the impact of time derivative is negligible, signifying the absence of memory in photodetectors.

2.1 Responsivity and quantum efficiency

Starting from Eq. (2.2), the first two metrics are defined, the responsivity $\mathcal{R}$ and the quantum efficiency η.

In the general case, the correlation between the current of the photodetector and the optical power is non-linear and can also have significant memory effects. When the function $p_{\mathrm{in}}(t)$ changes gradually with respect to the RC constant of the device, and the input optical power is relatively low, the relationship that links input optical power and output current can be simplified to a linear memoryless relationship.

$$i_{\mathrm{PD}}(t) = i_{\mathrm{L}} + i_{\mathrm{d}} \approx \mathcal{R}\left(\lambda, v_{\mathrm{PD}}\right) p_{\mathrm{in}}(t) + i_{\mathrm{d}}\left(v_{\mathrm{PD}}\right), \tag{2.4}$$

where $\mathcal{R}\left(\lambda, v_{\mathrm{PD}}\right)$ represents the responsivity for a specific wavelength and applied bias.

Eq. (2.4) shows that $i_{\mathrm{PD}}(t)$ can be approximated as the sum of i_{L} and i_{d}, which is mainly proportional to the responsivity $\mathcal{R}\left(\lambda, v_{\mathrm{PD}}\right)$ and the input optical power $p_{\mathrm{in}}(t)$.

Both the dark current and the responsivity of many photodetectors remain in most case unaffected by the applied v_{PD}. The dark current, under good design assumption, is minimal, making it negligible in such situations. Then, the photocurrent $i_{\mathrm{PD}}(t)$ can be approximated as the product of the responsivity $\mathcal{R}(\lambda)$ and the input optical power $pin(t)$, neglecting the dark current i_{d}:

$$i_{\mathrm{PD}}(t) = \mathcal{R}(\lambda)p_{\mathrm{in}}(t) + i_{\mathrm{d}} \approx \mathcal{R}(\lambda)p_{\mathrm{in}}(t). \tag{2.5}$$

Eq. (2.5) is a linear relationship that links the photocurrent i_{L} to input optical powers $P_{\mathrm{in}} \ll P_{\mathrm{in,sat}}$, where $P_{\mathrm{in,sat}}$ represents the saturation optical power at which the photocurrent saturates at $I_{\mathrm{L,sat}}$. Fig. 2.4 present a visual representation of this assumption, reporting the input optical power on the x axis, the photocurrent on the y axis, with the slope being the responsivity, reporting the saturation effect after the saturation optical power.

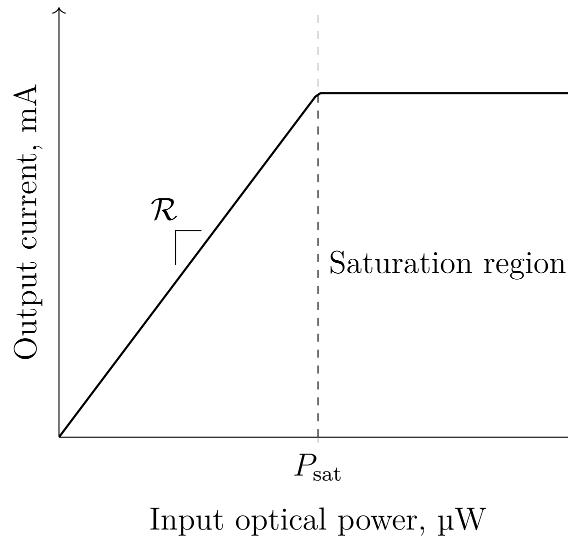

Fig. 2.4 Qualitatively correlation between output current and input optical power, for a given wavelength λ. For low input optical power the relationship is linear, with the slope defining the responsivity $\mathcal{R}$; while for $P > P_{\mathrm{sat}}$ the output current remains constant.

The responsivity $\mathcal{R}$ is the first metric presented and it assesses the effectiveness of converting incident optical power into an electrical signal. The responsivity is inherently connected to the process of generating photocurrent, which is determined by the optical generation rate G_{o}, that indicates the cre-

ation of photogenerated carriers based on volume and time. For a specific wavelength, this rate is obtained from the total absorbed optical power p_{in}. By integrating G_{o} over the entire active volume of the device, we may estimate the induced photocurrent I_{L} and, consequently, the responsivity $\mathcal{R}$ [1]:

$$I_{\mathrm{L}} = q \int_V G_{\mathrm{o}}(\underline{r}, p_{\mathrm{in}})\, \mathrm{d}\underline{r}, \tag{2.6}$$

with $\underline{r}$ being the spatial coordinate within the device domain.

This results in

$$\mathcal{R} = \frac{I_{\mathrm{L}}}{p_{\mathrm{in}}}. \tag{2.7}$$

In future simulations, the value of G_{o} is determined by a numerical solver of Maxwell equations that employs the Finite-Difference Time-Domain (FDTD) approach, introduced in Chap. 3.

For the estimation of the maximum responsivity $\mathcal{R}_{\mathrm{max}}$ at a given wavelength λ, employing a simple analytical model for G_{o} can provide the understanding of the theoretical limits of detector efficiency. Go can be simply derived from the input optical power:

$$\frac{\mathrm{d}\tilde{P}_{\mathrm{in}}(x)}{\mathrm{d}x} = -\alpha \tilde{P}_{\mathrm{in}}(x) \rightarrow \frac{\text{Energy absorbed}}{t \cdot V} = -\frac{\Delta \tilde{P}_{\mathrm{in}}}{\Delta x} = \alpha \tilde{P}_{in}, \tag{2.8}$$

where we have differentiated the power equation with respect to x and defined $\tilde{P}_{\mathrm{in}} = p_{\mathrm{in}}/A$ as the optical power density (W/m^2), A being the detection area [1]. Dividing by the photon energy $E_{\mathrm{ph}} = \hbar\omega$, and assuming for simplicity quantum efficiency $\eta = 1$: [2]

$$\begin{aligned} \frac{\alpha \tilde{P}_{\mathrm{in}}}{\hbar\omega} &= \frac{\text{Number of photons absorbed}}{t \cdot V} \\ &= \frac{\text{Number of e-h pairs generated}}{t \cdot V} = G_{\mathrm{o}}, \end{aligned} \tag{2.9}$$

hence

$$G_{\mathrm{O}} = \frac{\alpha \tilde{P}_{in}}{\hbar\omega}. \tag{2.10}$$

[2] This assumption can be safely done since we are assuming low injection condition, and almost all the photons are absorbed.

According to Beer-Lambert law the optical power density exponentially decreases with x, with L_α being the absorption length, with the optical generation rate following the same behavior:

$$G_\mathrm{o}(x) = \frac{\alpha \tilde{P}_\mathrm{in}(x)}{\hbar\omega} = \frac{\alpha \tilde{P}_\mathrm{in}(0)}{\hbar\omega} \exp\left(-x/L_\alpha\right) = G_\mathrm{o}(0) \exp\left(-x/L_\alpha\right). \tag{2.11}$$

The assumption that all the incoming optical power is absorbed is extended to all the generated electron hole pairs being collected. Thus the current can be computed as:

$$\frac{i_\mathrm{L}}{q} = A \int_0^\infty G_\mathrm{o}(x) \mathrm{d}x = A \int_0^\infty \frac{\alpha \tilde{P}_\mathrm{in}(x)}{\hbar\omega} \mathrm{d}x = -\frac{A}{\hbar\omega} \int_0^\infty \frac{\mathrm{d}\tilde{P}_\mathrm{in}(x)}{\mathrm{d}x} \mathrm{d}x \approx \frac{P_\mathrm{in}(0)}{\hbar\omega}, \tag{2.12}$$

and in conclusion

$$\frac{i_\mathrm{L}}{q} = \frac{P_\mathrm{in}(0)}{\hbar\omega}, \tag{2.13}$$

where $P_\mathrm{in}(0)$ is the incident power on the semiconductor. In this simple model the photocurrent indeed depends linearly on $P_\mathrm{in}(0)$ with responsivity $\mathcal{R}$ as the slope:

$$i_\mathrm{L} = \frac{q}{\hbar\omega} P_\mathrm{in}(0) = \mathcal{R} P_{in}(0). \tag{2.14}$$

With the tools to link the current to the input optical power, the responsivity can be computed as:

$$\mathcal{R} = \frac{q}{\hbar\omega} = \frac{q}{E_{ph}}, \tag{2.15}$$

Ideally, the responsivity is a function of the photon energy, and it has a maximum $\mathcal{R}_\mathrm{max}$. The photon energies below the absorption threshold, that is given by the energy gap of the material, gives a responsivity equals to zero; just above the threshold a sharp increase of α is present, and the $\mathcal{R}$ have its maximum for $E_\mathrm{ph} \approx E_\mathrm{g}$,:

$$\mathcal{R}_{max} \approx \frac{q}{E_\mathrm{g}} = \frac{1}{E_\mathrm{g}[\mathrm{eV}]} \approx \frac{\lambda[\mu\mathrm{m}]}{1.24}. \tag{2.16}$$

Conbining Eq. (2.15) and Eq. (2.16) it is possible to rewrite the equations as+

$$\mathcal{R}(E_{\text{ph}}) \approx \mathcal{R}_{max}\frac{E_{\text{g}}}{E_{\text{ph}}} \tag{2.17}$$

showing that for $E_{\text{ph}} > E_{\text{g}}$, the responsivity ideally decreases with increasing E_{ph}, as qualitately reported in Fig. 2.5.

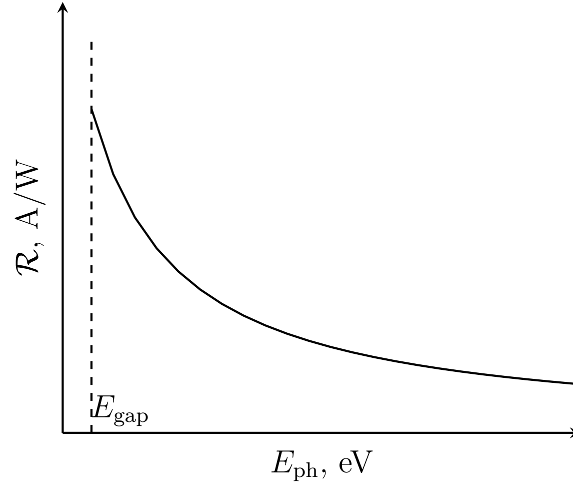

Fig. 2.5 A photodetector exhibits responsivity $\mathcal{R}$ that varies with the energy of the photons of the incident light. The peak is present for photon energy $E_{\text{ph}} \approx E_g$, defining $\mathcal{R}_{\text{max}}$. As the photon energy increase the process lead to higher energy e-h pairs and it can lead to avalanche process as well.

Once the responsivity is defined, the quantum efficiency (η) measures the photodetector ability to generate electron-hole pairs in response to incoming photons, representing the ratio of the generated carriers to the incident photons.

$$\eta = \frac{N_{\text{carriers}}}{N_{\text{photons}}}. \tag{2.18}$$

N_{carriers} represents the amount of carriers that are generated, while N_{photons} represents the quantity of photons that are incident. The quantum efficiency η is generally less than 1, but the closer to 1 indicates a more effective generation of carriers.

2.2 Electro-optic (modulation) bandwidth

After discussing the relation between the input optical power and the output current, linked by the responsivity, it is clear the need of a metrics that describes the "speed" of the photodetector. The electro-optic frequency response, or modulation bandwidth links the input modulated optical signal to the output modulated current. Fig. 2.6 illustrate a qualitative response of a *p*-*i*-*n* photodetector, highlighting the $-3\,\mathrm{dB}$ cutoff frequency f_{cutoff} that define the bandwidth of the detector.

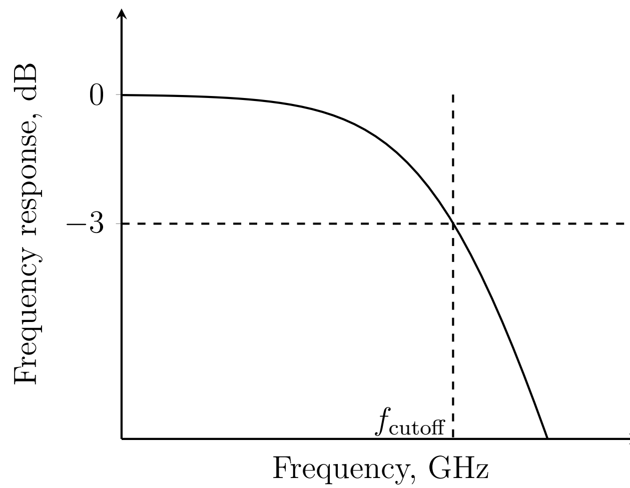

Fig. 2.6 Frequency response of a photodetector, normalized to the cutoff frequency. The response is similar (but not equal) to a low pass filter, and the electro-optic bandwidth is typically defined by the frequency f_{cutoff} for which the normalized response is equal to $-3\,\mathrm{dB}$.

As for the previous section, the output current of the photodetector may be expressed as:

$$i_{\mathrm{PD}}(t) = f\left(p_{\mathrm{in}}(t), v_{\mathrm{PD}}(t), \frac{d}{dt}, \lambda\right). \tag{2.19}$$

This relation, with the use of small signal analysis technique, can be split in three parts, a direct current (DC) and a alternating current (AC) components for each variable, for a fixed λ:

$$p_{\text{in}} = P_{\text{in},0} + \hat{p}_{\text{in}}(t), \quad v_{\text{PD}} = V_{\text{PD},0} + \hat{v}_{\text{PD}}(t), \quad i_{\text{PD}} = I_{\text{PD},0} + \hat{i}_{PD}(t). \tag{2.20}$$

$\hat{p}, \hat{v}, \hat{i}$ denote the small signal contribution. Assuming sinusoidal modulation, phasors can represent the photodetector response to harmonic modulation.

$$\hat{p}_{in}(t) = \Re\left(\hat{P}_{in}e^{j\omega t}\right) = \hat{P}_{\text{in}}(\omega), \tag{2.21}$$

$$\hat{v}_{PD}(t) = \Re\left(\hat{V}_{PD}e^{j\omega t}\right) = \hat{V}_{\text{PD}}(\omega), \tag{2.22}$$

$$\hat{i}_{PD}(t) = \Re\left(\hat{I}_{PD}e^{j\omega t}\right) = \hat{I}_{\text{PD}}(\omega), \tag{2.23}$$

with $\omega = 2\pi f$ representing the light angular modulation frequency. Following the same steps as for the responsivity, and linearizing around the DC working point, the small-signal photocurrent and dark current components can be computed as

$$\hat{i}_{\text{PD}}(t) = \hat{i}_L(t) + \hat{i}_{\text{d}}(t) = \Re\left(\mathcal{R}(\omega)\hat{P}_{in}e^{j\omega t}\right) + \Re\left(Y_{\text{PD}}(\omega)\hat{V}_{\text{PD}}e^{j\omega t}\right), \tag{2.24}$$

with the complex small-signal responsivity defined as $\mathcal{R}(\omega)$, and the small-signal admittance of the photodetector as $Y_{\text{PD}}(\omega)$. The small-signal detector current $\hat{i}_{\text{PD}}$ is affected by both the optical power and the voltage modulation as:

$$\hat{i}_{\text{PD}}(\omega) = Y_{\text{PD}}(\omega)\hat{V}_{\text{PD}}(\omega) + \hat{I}_{\text{L}}(\omega) = Y_{\text{PD}}(\omega)\hat{V}_{\text{PD}}(\omega) + \mathcal{R}(\omega)\hat{P}_{\text{in}}(\omega). \tag{2.25}$$

The responsivity $\mathcal{R}(\omega)$ of the system usually shows a low-pass filter like bode plot, as shows in Fig. 2.6. The bandwidth is the range of frequencies, defined by the $-3\,\text{dB}$ frequency f_{cutoff}, at which the responsivity decreases to $\frac{1}{\sqrt{2}}$ of its direct current (DC) value.

$$20\log_{10}\left|\frac{\mathcal{R}(\omega_{\text{cutoff}})}{\mathcal{R}(0)}\right| = -3 \quad \Rightarrow \quad \mathcal{R}(f_{\text{cutoff}}) = \frac{\mathcal{R}(0)}{\sqrt{2}}. \tag{2.26}$$

2.3 Circuit model and frequency response

The electric model of the photodetector consists of a current generator that is connected with intrinsic parasitic resistance and capacitance, reported in Fig. 2.7. The capacitance and parasitic resistances of the device play a crucial role in determining its performance. In fact, these factors mainly limit the bandwidth of the output current.

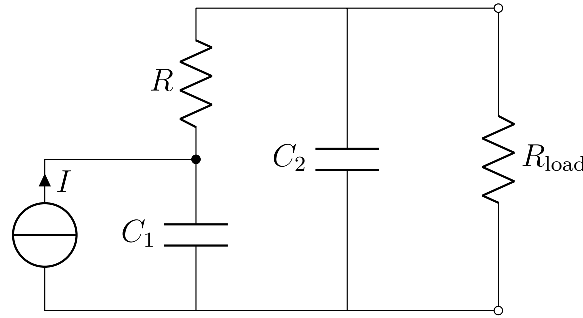

Fig. 2.7 Simplified circuit model of a photodetector, illustrating the key electrical components. The resistor R and the capacitor C_1 are intrinsic components of the device, with C_1 that can be approximated with a parallel plate capacitor. C_2 represents the parassitic external capacitor.

In Chap. 4, this equivalent circuit can be employed to extract the values of parasitic capacitance and resistance from numerical simulations. Then, these values can be utilized to compute the overall device bandwidth, splitting in the two main contribution: the transit time bandwidth of the photogenerated carriers and the RC bandwidth.

As for previous sections, a simple model can be helpful to understand the behavior of the device. Neglecting diffusion currents and assuming a constant electric field and $v_{n,\mathrm{sat}}$ and $v_{h,\mathrm{sat}}$[3] defined as the electron and hole saturation velocites, respectively, the system of drift diffusion photocurrent equations is simply:

$$\frac{\partial p}{\partial t} = G_o(x,t) - \frac{1}{q}\frac{\partial J_h}{\partial x},$$
$$\frac{\partial n}{\partial t} = G_o(x,t) + \frac{1}{q}\frac{\partial J_n}{\partial x},$$

[3] The saturation velocity of carriers is the ideal condition, influencing the transit time, that we will see in the derivation is one of the limiting factor of the bandwidth.

where the hole and electron current densities are given by:

$$J_h = qv_{h,\mathrm{sat}}p, \quad J_n = qv_{n,\mathrm{sat}}n.$$

We set $x = 0$ at the $p^+ - i$ junction and $x = W$ at the $i - n^+$ junction. With harmonic optical incident power at modulation angular frequency ω, the input power can be expressed as:

$$p_{\mathrm{in}}(t) = P_{\mathrm{in}}(\omega)e^{\mathrm{j}\omega t}.$$

Using the method described in [1, Sec 4.9.3], the total photocurrent density $J_t(\omega)$ can be calculated as:

$$J_t(\omega) = \frac{1}{W}\frac{qv_{h,\mathrm{sat}}G_o}{\mathrm{j}\omega - \alpha v_{h,\mathrm{sat}}}e^{-\alpha W}\left(\frac{e^{\alpha W}-1}{\alpha} + \frac{1-e^{\frac{\mathrm{j}\omega W}{v_{h,\mathrm{sat}}}}}{\mathrm{j}\omega/v_{h,\mathrm{sat}}}\right) + \frac{qv_{n,\mathrm{sat}}G_o}{\mathrm{j}\omega + \alpha v_{n,\mathrm{sat}}}\left(\frac{1-e^{-\alpha W}}{\alpha} + \frac{1-e^{\frac{\mathrm{j}\omega W}{v_{h,\mathrm{sat}}}}}{\mathrm{j}\omega/v_{h,\mathrm{sat}}}\right). \quad (2.27)$$

with e-h transit times defined as:

$$\tau_{dr,n} = \frac{W}{v_{n,\mathrm{sat}}}, \quad \tau_{dr,h} = \frac{W}{v_{h,\mathrm{sat}}}.$$

With the definition of Eq. (2.11), we can define $G_o(0,\omega)$, taking into account surface reflection R and quantum efficiency η:

$$G_o(0,\omega) = \eta\frac{(1-R)}{Ahf}\alpha P_{in}(\omega).$$

Finally, the total photodiode current I_t can be expressed as:

$$\begin{aligned} I_t(\omega) = \alpha W \frac{q}{hf}\eta(1-R)P_{in}(\omega) \\ \times \left\{ \frac{e^{-\alpha W}-1}{\alpha W(\alpha W - \mathrm{j}\omega\tau_{dr,h})} + e^{-\alpha W}\frac{e^{\mathrm{j}\omega\tau_{dr,h}}-1}{\mathrm{j}\omega\tau_{dr,h}(\alpha W - \mathrm{j}\omega\tau_{dr,h})} \right. \\ \left. + \frac{1-e^{-\alpha W}}{\alpha W(\mathrm{j}\omega\tau_{dr,n}+\alpha W)} + \frac{1-e^{\mathrm{j}\omega\tau_{dr,n}}}{\mathrm{j}\omega\tau_{dr,n}(\mathrm{j}\omega\tau_{dr,n}+\alpha W)} \right\}. \end{aligned} \quad (2.28)$$

In the frequency-domain analysis, the photocurrent derived can be associated with a photocurrent generator in the detector equivalent circuit as shown in Fig. 2.7. From this equivalent circuit, the RC-limited cutoff frequency can be estimated. Consider C_2 as the external diode parasitic capacitance, R as the diode resistance. The intrinsic capacitance C_1, primarily dominated by the intrinsic layer capacitance, also plays a role. The 3 dB RC-limited photodiode bandwidth is given by

$$f_{3\mathrm{dB},RC} \approx \frac{1}{2\pi RC}, \quad (2.29)$$

where

$$R \approx R + R_L, \quad C \approx C_1 + C_2, \quad C_1 \approx \frac{\epsilon_s A}{d}.$$

The total cutoff frequency, accounting for both the transit time and RC effects, can be evaluated with an approximate expression for the total 3 dB cutoff frequency

$$f_{3\mathrm{dB}} \approx \frac{1}{\sqrt{f_{3\mathrm{dB},RC}^{-2} + f_{3\mathrm{dB},tr}^{-2}}}. \quad (2.30)$$

2.4 Lateral vs vertical photodetectors: a matter of trade-offs

This work is focused on the O-band of optical communications, centered around $\lambda = 1.31\,\mu\mathrm{m}$, where the absorption of Ge is higher [25] and the device performance is expected to be significantly more sensitive to the input optical power than in the C-band.

Ge-on-Si waveguide photodetectors (WPDs) are classified into vertical (VPIN) and lateral (LPIN) variants based on their structural configurations. LPIN-WPDs have high bandwidth, while their responsivity may be far from the ideal value, necessitating careful consideration of the trade-off. VPIN photodetectors are widely recognized instead for their optimal combination of bandwidth and responsivity.

In the LPIN configuration, the germanium absorption region is positioned between two highly doped silicon regions, one of n-type and the other of p-type. In a recent study Lischke et al. (2021) [7] introduced a novel approach where thin FinFET-like LPIN WPDs demonstrated the capability to achieve bandwidths f_{cutoff} exceeding 200 GHz. However, this improvement comes at the cost of reduced responsivity $\mathcal{R}$.

In VPIN configurations, the substrate is the the bottom contact, with a small portion of Ge highly doped used as contact. Previous studies have reported VPIN WPDs with bandwidths exceeding 50 GHz in both O- and C-band. These achievements were primarily made possible through extrinsic parameter engineering, specifically inductive gain peaking. This technique, as demonstrated in various references, can enhance the intrinsic frequency response of the VPIN drastically [26–28].

Optimizing WPDs to achieve better performance by exploiting the strong absorption properties of germanium presents several challenges. This task is further complicated by the strong electric field screening effects that results under conditions of high optical injection. To address these problems, it is necessary to develop a multiphysics model that integrates electromagnetic and carrier transport phenomena. This model will focus on the complex computational operations required to improve the efficiency of SiPh systems.

For an illuminated photodiode, it is recommended to optimize the quantum efficiency by ensuring that the width is much more than the absorption length $L_\alpha = 1/\alpha$. Also, it is useful to have a wide A detection area to improve the connection with an external source, such as an optical waveguide. However, as the value of W decreases, the bandwidth limited by RC increases due to the decrease of the junction capacity, while the bandwidth limited by the transit time decreases. Expanding the area of the device does not affect the bandwidth limited by transit time, but increases the capacity, resulting in a decrease in

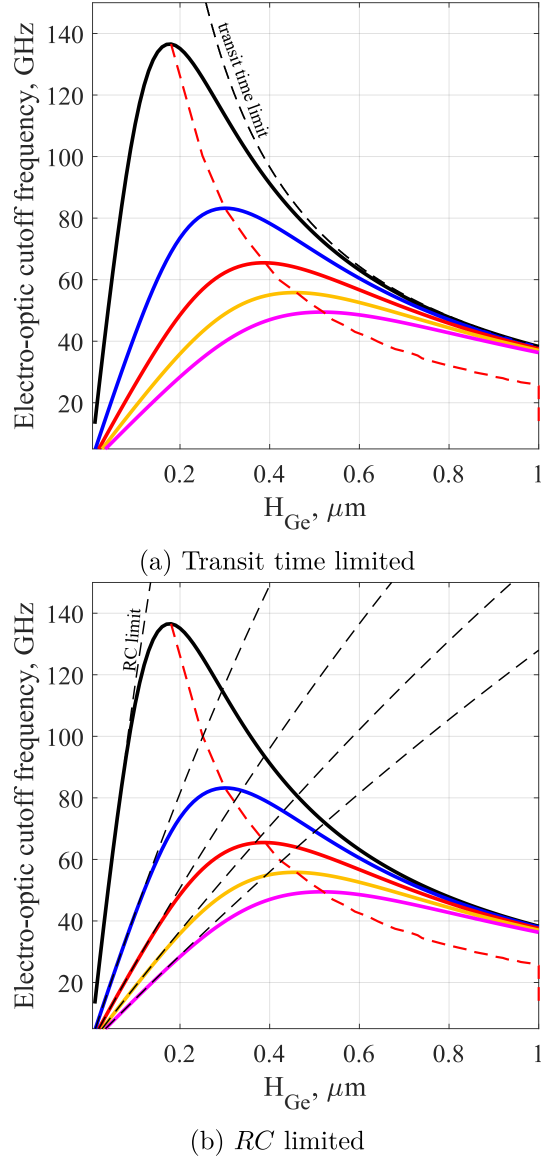

(a) Transit time limited

(b) RC limited

Fig. 2.8 Analytic model implementing Eq. (2.28) and the RC simple model. H_{Ge} is used as an example of the width of the absorber region, with Ge referring to germanium, the material of the detector of the following chapters. The area is varying from low value (black curve) to high value (magenta curve), with significant reduction of the cutoff frequency. Dashed line in (a) represents the transit time limit, with the red dashed line indicating the maximum cutoff frequency; while dashed lines in (b) represnts the RC limitations of the cutoff frequency. This behavior is mainly due to the difference in the RC components and not to the transit time response.

the bandwidth limited by RC. Holding the device area A constant, we can observe that the 3-dB frequency $f_{3\ \mathrm{dB},RC}$ is directly proportional to the width

W, while the 3-dB frequency $f_{3\text{ dB},tr}$ is inversely proportional to W. Since $f_{3\text{ dB}}$ is less than the minimum of $f_{3\text{ dB},RC}$ and $f_{3\text{ dB},tr}$, the total bandwidth is mainly determined by $f_{3\text{ dB}RC}$, which is proportional to W for low values of W, or by $f_{3\text{ dB},tr}$, which is proportional to $1/W$ for high values of W. The total bandwidth initially increases with the variable W, but eventually decreases. Consequently, the maximum value of $f_{3\text{ dB}}$ fluctuates toward smaller values of W and higher cutoff frequencies as A decreases. At the same time, the efficiency increases steadily with the variable W. Therefore, in order to achieve high-frequency operation (high $f_{3\text{ dB}}$), it is necessary to use diodes with small area, small W and decreasing efficiency.

Fig. 2.8 presents an analytical study that is based on the concepts and terminology just outlined, inspired by [1, Sec. 4.9]. The plot is based on parameters from the reference device in Chap. 4, a Ge-on-si p-i-n photodetector.

The graph is separated into two distinct sections. When the height exceeds 0.4 microm, the device is limited by the transit time (Fig. 2.8a), which means that the behavior of the device is not significantly affected by the R and C components. In contrast, when the heights are lower than 0.3 microm, the bandwidth is significantly reduced due to the combined effects of resistance (R) and capacitance (C) (Fig. 2.8b). The different curves, from magenta to black, denoted different areas, ranging from 60 µm^2 to 15 µm^2. It should be noted that as the area decreases, the potential for larger bandwidths increases.

Chapter 3

State-of-the-art and multiphysics modeling

This chapter provides an overview of the current state of the art on Ge-on-Si photodetectors, comparing the two configurations described in section Sec. 2.4 with also the results described in Chap. 4 and Chap. 5. Next, I will go into the multiphysics model using Synopsys TCAD Sentarus suite (Sentaurus Device N-2017.09 [29]) as a tool.

3.1 Current status of WPDs

The goal of higher data bitrates in silicon photonics is demonstrated by the recent increase in publications focused on achieving 200 Gbit/s operation, while also aiming to minimize power consumption in data communication systems [8, 30, 31].

An extensive assessment of the present situation indicates that WPD technologies have made significant advancements. Michel et al. (2010) [32] present one of the first and most complete review of the state of the art of silicon phtonics. Pavesi et al. (2004, 2016) [9, 10] in two separate books reports the comprehansive status of all the components in silicon photonics; and Thomson et al. (2016) [11] describe the roadmap of the development of new device generation. Vivien et Pavesi [12] and Boeuf et al. [33] have highlighted as well the advancements in silicon phtonics, setting the stage for further innovation.

Siew et al. (2021) [2] and Margalit et al. (2021) [34] provided insights into emerging SiPh technologies, paving the way for the development of WPDs suitable for next-generation data transmission rates.

VPINs and LPINs[1] were studied already in the early 2000's by Colace et al. [35], but for many years their bandwidth was limited around 20 GHz. This limitation induced by an integration of germanium on silicon not yet ready, was faced by Tada et al. (2010) [13], with a research to develop high quality thin film germanium on a silicon substrate. Only ten years later the barrier of 40 Gbit/s was overcome [36]

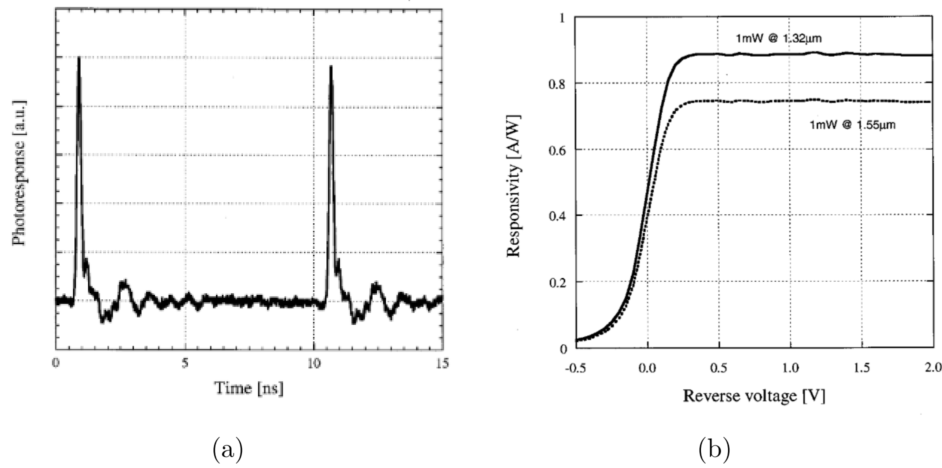

(a) (b)

Fig. 3.1 PI curve and impulse response taken from [4]. This device is one of the first implementation and fabrication of Ge-on-Si photodetectors.

There has been then a substantial increase in the research on both (VPIN) and (LPIN) Ge-on-Si WPDs. Benedikovic et al. (2019) [37] and Zuo et al. (2019) [38] have investigated the LPIN architecture, whereas Shi et al. (2022)[39] and Chen et al. (2022) [17] have concentrated on VPIN devices, showcasing notable improvements in bandwidth and efficiency. Lischke et al. (2021) [7] presented a novel thin FinFET-like LPIN WPD that achieved bandwidths above 200 GHz. This design demonstrated a trade-off with responsivity. Other examples based on differenct configurations or approach are [40–42, 23], or high power application [6] and [43, 5] with the characteristic plots reported in Fig. 3.2. [44] report of an example of tensile strained Ge. and [21] describes CMOS silicon photonics.

[1] Vertical *p-i-n* (VPIN) and lateral *p-i-n* (LPIN) waveguide Ge-on-Si photodetector

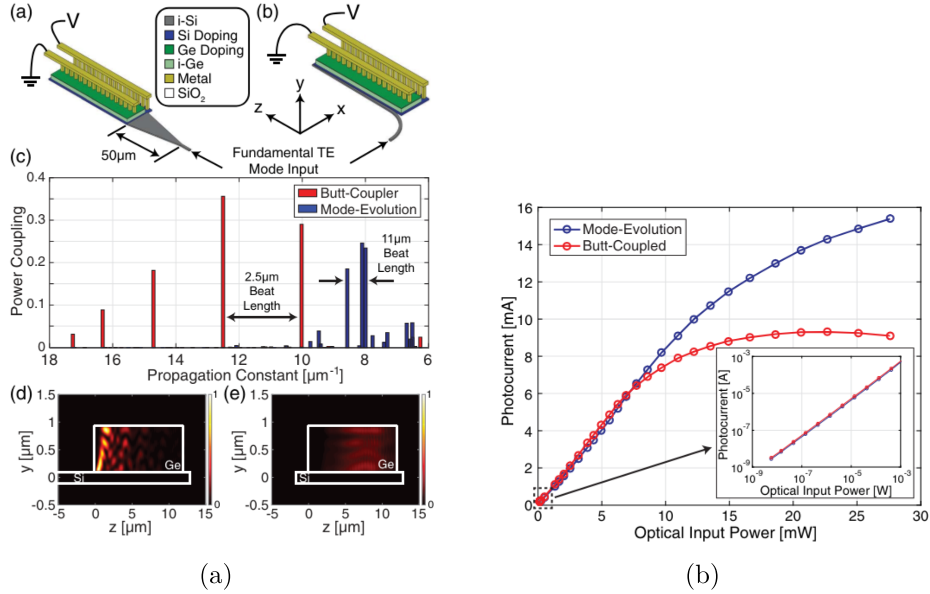

(a) (b)

Fig. 3.2 The device, taken from [5], is a device significantly different from common devices, with a lateral taper that evanescently couple the light to the absorber region. The space left between waveguide and absorber is a key factor to discribute the light along the device, allowing for high input optical powers.

The prevalent VPIN setup utilized in present SiPh platforms, including those developed by Cisco, need more investigation due to its extensive adoption. Devices with a bandwidth exceeding 50 GHz have been successfully developed using techniques such as inductive peaking [27, 28, 26], which can greatly enhance the performance of the device itself. This technique is used to introduce an integrated inductor to compensate and enhance the bandwidth, but the uncertanty of the fabrication process of such component makes this solution not ready yet for commercial purposes.

Regarding the multiphysics model, only a few researchers, particularly Fard et al. [18] and Chang et al. [45], have explored the complexities of the interactions between electromagnetic and carrier transport phenomena. These researchers have made significant contributions to the field.

Finally, Table 3.1 reports a comparison of some literature device with the one reported in Chap. 4.

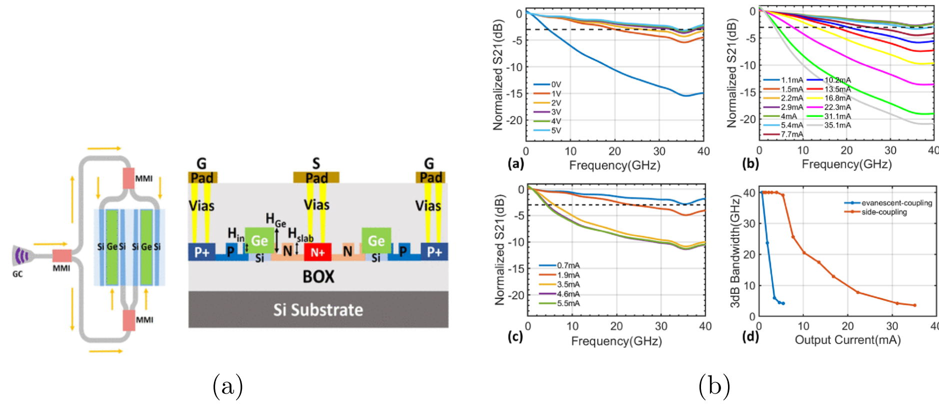

(a) (b)

Fig. 3.3 (a) device structure and (b) frequency response for high power applications. Taken from [6].

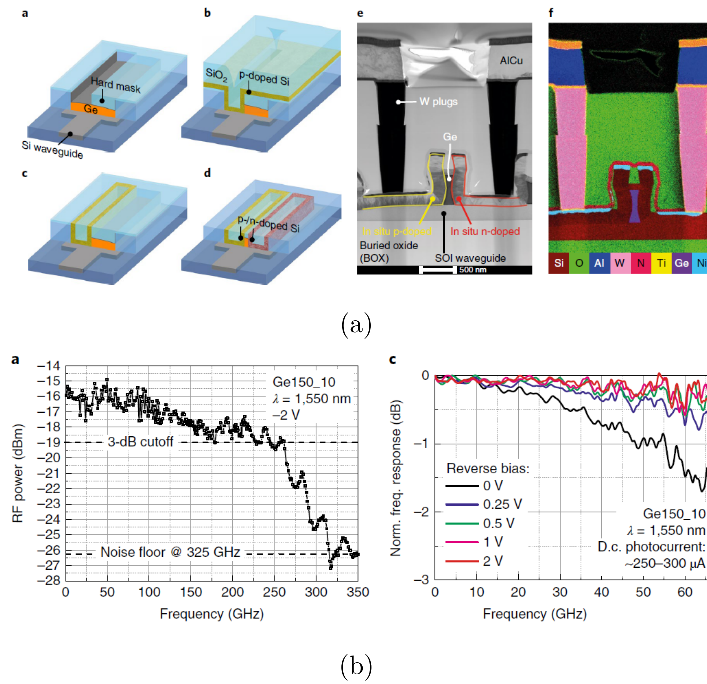

(a)

(b)

Fig. 3.4 An innovative lateral *pin* waveguide Ge-on-Si photodetector, with fabrication (a) inspired by FinFET-like manufacturing processes. (b) The electro-optic frequency response shows an impressive cutoff frequency higher than 200 GHz. Taken from [7], this device will be used as reference structure in Chap. 5.

3.2 Drift-diffusion transport model

The Drift-Diffusion model (DD) is the most established electronic transport model in the simulation of semiconductor devices. This approach can be

Table 3.1 Responsivity and cutoff frequency of representative VPIN and LPIN devices.

Reference	**Structure**	**Band**	$\mathcal{R}$, **A/W**	f_{cutoff}, **GHz**
[18]	VPIN	C-band	1.09	42.5
[46]	VPIN	C-band	0.80	49.5
[47]	VPIN	C-band	0.95	103
this work, experiments	VPIN	O-band	0.9	39.8
this work, optimized	VPIN	O-band	0.76	64
[37]	LPIN	C-band	0.6	30
[7]	LPIN	C-band	0.3	265
[48]	LPIN	C-band	0.63–0.74	51

derived from the semi-classical Boltzmann transport equation [49], assuming quasi-equilibrium and defining the contributions of electrons and holes in terms of drift and diffusion currents:

$$\vec{J}_n = qn\mu_n\vec{E} + qD_n\nabla n, \tag{3.1a}$$

$$\vec{J}_p = qp\mu_p\vec{E} - qD_p\nabla p, \tag{3.1b}$$

Where q is the electron charge, n and p are the electron and hole carrier concentrations respectively, $\vec{E}$ the electric field, while μ_n, μ_n and D_n, D_n being the mobility and diffusivity of electrons and holes respectively. The drift current for both equations is driven by the applied electric field $\vec{E}$. Spatial variation in the carrier concentration generates diffusion current.

D_n and D_p are related to μ_n and μ_p with the Einstein relations:

$$D_n = V_T\mu_n, \quad D_p = V_T\mu_p, \tag{3.2}$$

with $V_T = \frac{k_bT}{q} \approx 26\,\text{mV}$ being the thermal voltage at room temperature.

But to have a complete system of equations, the drift diffusion model takes into account charge conservation with continuity equations for electrons and holes. They describe the temporal evolution of carrier concentration as a

function of spatial flux variations and net generation-recombination within the material:

$$\frac{\partial n}{\partial t} = \frac{1}{q}\nabla \cdot \vec{J}_n - (R_n - G_n), \tag{3.3a}$$

$$\frac{\partial p}{\partial t} = -\frac{1}{q}\nabla \cdot \vec{J}_p - (R_p - G_p), \tag{3.3b}$$

with recombination rates denoted by R, and generation rates denoted by G.

ρ, the net charge density, is conneted to the spatial electric field with Gauss law:

$$\nabla \cdot (\epsilon \vec{E}) = \rho, \quad \rho = q(p - n + N_D^+ - N_A^-), \tag{3.4}$$

Finally, Poisson's equation can be derived substituting the electric potential $\vec{E} = -\nabla\phi$:

$$\nabla \cdot (-\epsilon \nabla \phi) = \rho. \tag{3.5}$$

Continuity equations Eq. (3.3), Poisson's equation Eq. (3.5), and the current density definitions Eq. (3.1) define the Drift-Diffusion model. Eq. (3.6) reports the static Drift Diffusion model. This model approximates with significant accuracy the electrical behavior in semiconductors and semiconductor devices [50]. In steady-state condition (without the thine dependency), the system can be written as

$$\begin{cases} \nabla \cdot (-\epsilon \nabla \phi) = q(p - n + N_D^+ - N_A^-) \\ \frac{1}{q}\nabla \cdot \vec{J}_n = (R_n - G_n) \\ -\frac{1}{q}\nabla \cdot \vec{J}_p = (R_p - G_p) \\ \vec{J}_n = -qn\mu_n \nabla \phi + qD_n \nabla n \\ \vec{J}_p = -qp\mu_p \nabla \phi - qD_p \nabla p \end{cases} \tag{3.6}$$

In Appendix A a more comprehensive description of the drift diffusion model is reported.

Two of the authors that impacted the most were Scharfetter and Gummel [51], suggesting the numerical approach for the bipolar transistor. In fact, the standard discretisation methods (like finite difference method) suited for the analysis of small semiconductor devices, lead to instabilities and significant amount of computational resources are needed in order to obtain acceptable results. Scharfetter and Gummel developed a more sophisticated discretization method, which is still in use nowadays, solving the instability problem [52]. This foundational approach is still used nowadays in most of the commercial tools present, and it defined the simulation gold standard for solving drift-diffusion equations.

3.2.1 Generation and recombination rates

Eq. (3.3) contains in both equation a term dedicated to that are defined as the rates of generation and recombination. These processes can be splitted in two categories: intrinsic processes, and extrinsic processes. The intrinsic processes contain thermal, radiative, and Auger processes. This mechanisms take place even in ideal crystals. The extrinsic processes contain mainly Shockley-Read-Hall (SRH) G-R model, with generation and recombination due to defects in the fabrication process.

Radiative recombination is the process by which a particle interacts with another particle, emitting electromagnetic radiation. The radiative recombination mechanism is a process where photons may be emitted by combining electrons and holes. The model used is:

$$U^{rad} = r^{opt}(np - n_i^2), \tag{3.7}$$

with r^{opt} denoting the optical recombination coefficient. Optical generation may occur if photons with energies equal to or greater than the bandgap are absorbed, leading electrons to migrate to the conduction band.

Auger Recombination is a phenomenon where the energy of one excited electron in a semiconductor material is transferred to another electron, leading

to the emission of a third electron. This many-body interaction involves the participation of an electron, a hole, and a third carrier that facilitates the process of recombination and generation of carriers. The rate is defined as:

$$U^{Au} = (r_{cn}^{Au} n + r_{cp}^{Au} p)(np - n_i^2), \tag{3.8}$$

with Auger coefficients r_{cn}^{Au} and r_{cp}^{Au} for electrons and holes, respectively.

Shockley-Read-Hall (SRH) recombination is the mechanism in which electrons and holes recombine again in a semiconductor material because of the existence of imperfections or impurities. The G-R process occurs with the presence of energy states caused by impurities or defects, "lowering" the energy difference between the conduction and valence bands. The rate is:

$$U^{SRH} = \frac{np - n_i^2}{\tau_p(n + n_1) + \tau_n(p + p_1)}, \tag{3.9}$$

with lifetimes of the carriers defined as τ_p and τ_n, n_1 and p_1 indicates parameters linked to those states being occupied.

3.2.2 Mobility models

Carrier mobility models describe how carrier "speed" within the material. There are several models, but for high bandwidth communication applications, high electric field dependency is essential for accurate modeling.

The Canali model [53] describes the impact of the electric field on the mobility, with a parameter called saturation velocity v_{sat}, linking the low field mobility μ_{low} to the total new mobilit μ.

$$\mu_{field}(E) = \frac{(\alpha + 1)\mu_{\text{low}}}{\alpha + \left[1 + \left(\frac{(\alpha+1)\mu_{\text{low}} E}{v_{sat}}\right)^{\beta}\right]^{1/\beta}}, \tag{3.10}$$

with α and β are the fitting parameters related to temperature.

3.3 Finite-Difference Time-Domain method

This section describes the numerical approach, included in Synopsys TCAD Sentaurus and RSoft FullWave tool, that solve Maxwell equations with a finite difference approach, used in this thesis coupled with the drift diffusion model. It is called Finite-Difference Time-Domain (FDTD) approach and it is widely used to solve Maxwell's equations in two or three dimensions in small devices [54].

The method obtains approximate solutions to the system of partial differential equations connected with the electromagnetic problem.

The Maxwell equations can be expressed as

$$\begin{aligned} \frac{\partial \mathcal{D}}{\partial t} &= \nabla \times \mathcal{H} - J && \text{(Faraday's Law)}, \\ \frac{\partial \mathcal{B}}{\partial t} &= -\nabla \times \mathcal{E} && \text{(Ampère's Law)}, \\ \nabla \cdot \mathcal{B} &= 0 && \text{(Gauss's Law for magnetism)}, \\ \nabla \cdot \mathcal{D} &= \rho && \text{(Gauss's Law for electric fields)}. \end{aligned} \tag{3.11}$$

with constitutive relations

$$\begin{aligned} \mathcal{D} &= \epsilon_0 \mathcal{E} \\ \mathcal{H} &= \tfrac{1}{\mu_0} \mathcal{B} \end{aligned} \tag{3.12}$$

The FDTD method calculates the numerical solutions using a finite difference approximation for spatial and temporal derivatives. This method has been first proposed by [55]. A first assumption then, is that the wavelength and the size of the domain should not differ too much one for the other. Since it is a simulation in time, the light has to travel in the device domain, then reflect and diffract, to finally get convergence, i.e. a steady state solution.

In order to use the method, the first step is to approximate the first order derivatives, so for a generic function f and step δ:

$$\frac{f\left(x + \frac{\delta}{2}\right) - f\left(x - \frac{\delta}{2}\right)}{\delta} = f'\left(x_0\right) + O\left(\delta^2\right), \tag{3.13}$$

hence,

$$f'(x_0) \approx \frac{f\left(x+\frac{\delta}{2}\right) - f\left(x-\frac{\delta}{2}\right)}{\delta}. \tag{3.14}$$

Notice that such approximation is δ^2 -accurate.

Yee's Algorithm The first implementation of the method, presented by [55], takes advantages of second-order centered differences. The algorithm can be divided in the following steps:

1. discretise space and time for the electric and magnetic fields;
2. replace all the derivatives in Ampere's and Faraday's laws with finite differences;
3. use the current values of the electric fields to compute the magnetic fields one time-step into the future;
4. use the values of the magnetic fields obtained in previous step to compute the electric field one time-step into the future;
5. iterate the previous two steps until the fields have been obtained over the desired time interval.

The comprehensive technique, together with several implementations can be seen for example in [54].

Fig. 3.5 shows the reference device for Chap. 4 and Chap. 5 with the boundary of the computational box, where 16 perfect matched layer (PML) boundary condition cells are applied.

One-dimensional example In a 1D example, consider a plane wave in the z direction in "free space".

E_x and H_y are the only non-zero components of Maxwell equations, with:

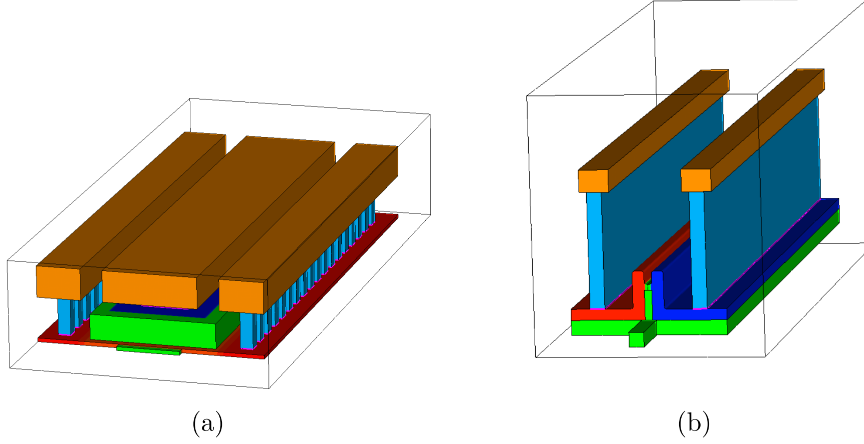

(a) (b)

Fig. 3.5 Perspective view of (a) the vertical waveguide photodetector, and (b) the lateral waveguide photodetector, studied in this dissertation. The computational box is also reported. The first copper metallic layer (orange) is connected with tungsten walls (light blue) to the silicon substrate and to germanium for the vertical case. Germanium is the central green block, with red and blue region indicating the p and n doping the the silicon substrate and at the germanium/top contact interface.

$$
\begin{aligned}
\frac{\partial E_x}{\partial t} &= -\frac{1}{\epsilon_0}\frac{\partial H_y}{\partial z},\\
\frac{\partial H_y}{\partial t} &= -\frac{1}{\mu_0}\frac{\partial E_x}{\partial z},
\end{aligned}
\tag{3.15}
$$

Considering a centred difference scheme, E_x and H_y are evaluated at the midpoints, i.e. in the half point of the mesh chosen ($\Delta x/2$), same for time ($\Delta t/2$):

$$
\begin{aligned}
\frac{E_x^{n+\frac{1}{2}}(k) - E_x^{n-\frac{1}{2}}(k)}{\Delta t} &= -\frac{1}{\epsilon_0}\frac{H_y^n\left(k+\frac{1}{2}\right) - H_y^n\left(k-\frac{1}{2}\right)}{\Delta z},\\
\frac{H_y^{n+1}\left(k+\frac{1}{2}\right) - H_y^n\left(k+\frac{1}{2}\right)}{\Delta t} &= -\frac{1}{\mu_0}\frac{E_x^{n+\frac{1}{2}}(k+1) - E_x^{n+\frac{1}{2}}(k)}{\Delta z},
\end{aligned}
\tag{3.16}
$$

with k the discretised space index and n the discretised time index. Rearranging the equations, the explicit FDTD equations are:

$$\begin{aligned} E_x^{n+\frac{1}{2}}(k) &= E_x^{n-\frac{1}{2}}(k) + \frac{\Delta t}{\epsilon_0 \Delta z}\left(H_y^n\left(k-\tfrac{1}{2}\right) - H_y^n\left(k+\tfrac{1}{2}\right)\right) \\ H_y^{n+1}\left(k+\tfrac{1}{2}\right) &= H_y^n\left(k+\tfrac{1}{2}\right) + \frac{\Delta t}{\mu_0 \Delta z}\left(E_x^{n+\frac{1}{2}}(k) - E_x^{n+\frac{1}{2}}(k+1)\right) \end{aligned} \tag{3.17}$$

to these equations suitable boundary conditions (PEC, PML, . . .) must be applied.

Stability of the method The method presents instabilities that have been extensively studied in the literature and that can be solved with a relation between the time step and the space step.

It is reasonable to assume that

$$c\Delta t < \Delta z, \tag{3.18}$$

with c being the speed of light. Typically, in 3D, $\Delta x = \Delta y = \Delta z$, and we safely set Δz to be:

$$\Delta z < \frac{\lambda_{min}}{10}. \tag{3.19}$$

Peculiarities and remarks The FDTD method, if applied correctly, is reliable and robust. Systematic errors are mostly due to space or time discretization. A suitable choice of mesh grid is then mandatory to improve the stability of the results, at the cost of increasing the computation costs. This demonstrates that the method is not recommended for studying diffraction due to large objects.

Boundary conditions are important and must be carefully chosen based on the specific problem at hand because the simulation domain is inevitably bounded.

3.4 Multiphysics model

In this section report the multiphysics model that is used in Chap. 4 and Chap. 5. The challenge is the integration of different solvers that interact on a

single device one with the other. In other words, a multiphysics model is linking in some way (either self-consistently or open-loop) the solution of one model to the other. The two models that have been chosen are the optical model, based on the numerical solution of Maxwell equation with FDTD method (Sec. 3.3) and the Drift-Diffusion model (Sec. 3.2, Appendix A, Eq. (3.6)). The framework chosen is Synopsys TCAD Sentaurus, with a focus on Synopsys RSoft FullWave for the optical problem [56], and Synopsys TCAD sDevice [29] for the electrical problem. The solution is carried out in steady state.

RSoft FullWave is used to evaluate the optical field within the specified domain and then, accounting for various material properties, converted into a generation rate. RSoft FullWave computes the spatial distribution of the optical generation rate $G_{\text{opt}}(x, y, z)$ from the time-averaged divergence of the Poynting vector, the calculation are reported in Appendix B.. For an input optical power of 200 µW, two examples of G_{opt} in the Ge absorber are reported in Fig. 5.5 and Fig. 4.9. An intricate interference pattern with notable local variations can be seen.

The optical input is the waveguide mode that propagates along a tapered waveguide and enters the photodetector, and an example of this mode is reported in Fig. 3.6. Fig. 3.6a shows a normalized 2D mode evaluated with RSoft at the end of the tapered waveguide, before the silicon substrate; 3.6b shows a 1D horizontal normalized cut at the peak value.

After the RSoft computations, G_{opt} enters as a source term in the continuity electron and hole equations (Eq. (3.3)), solved self-consistently with the Poisson equation taking into account Fermi-Dirac statistics and incomplete dopant ionization.

Fig. 3.7 shows a schematic based on Synopsys TCAD Sentaurus and Synopsys RSoft FullWave of the steps required for the simulation. Finally Table 3.2 reports comparisons of the typical computational costs associated with simulations of VPIN and LPIN.

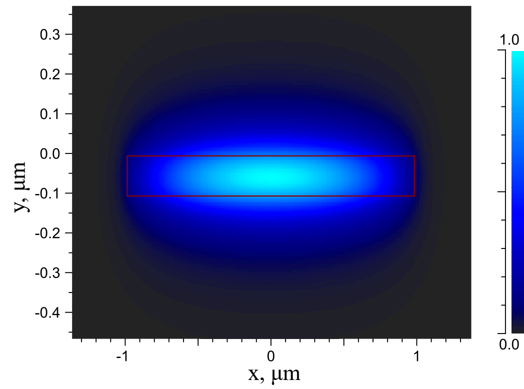

(a)

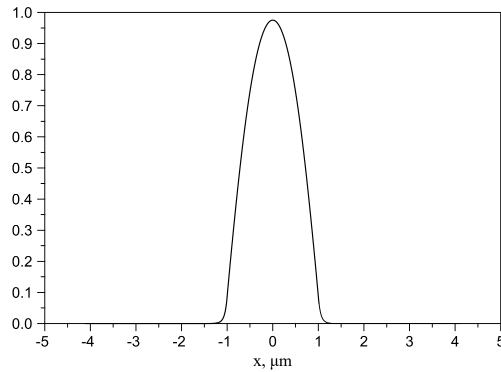

(b)

Fig. 3.6 (a) normalized waveguide mode calculation for the input waveguide of the reference vertical photodetector presented in Chap. 4 (red rectangle), evaluated at the end of the taper with RSoft FullWave; (b) is a 1D horizontal normalized cut of (a) at the peak.

Table 3.2 Typical computational costs for LPIN and VPIN, with cell size for uniform mesh of the FDTD method.

Process	**VPIN**	**LPIN**
Optical Simulation (FDTD)	3.0h	5.0h
with mesh	25 nm	5 nm
Drift Diffusion (Bias)	2.0h	2.0h
Drift Diffusion (Frequency Response)	6.0h	6.0h
Total	11h	13h

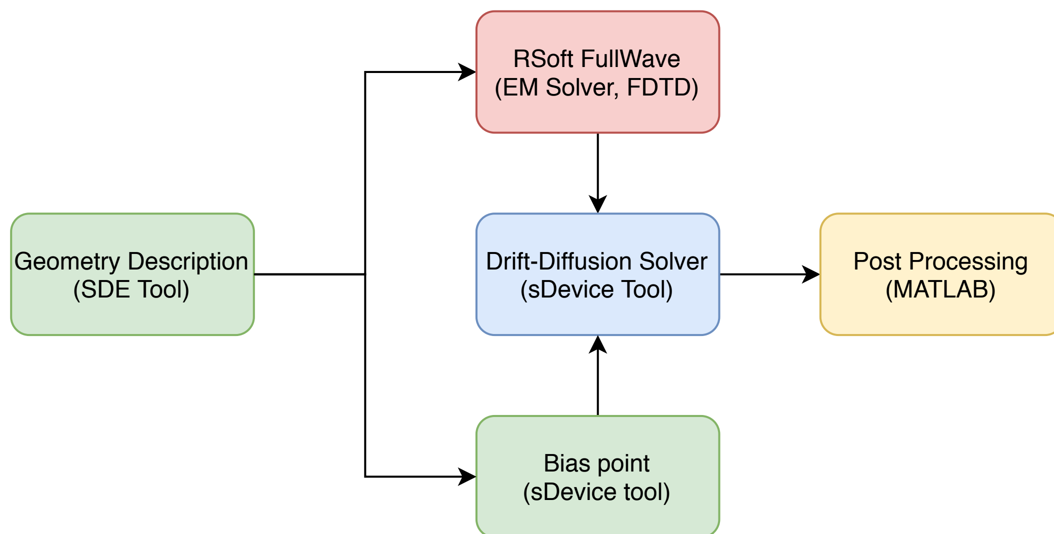

Fig. 3.7 Schematic representation of the model used in TCAD Sentarus

Chapter 4

Vertical *p-i-n* Ge-on-Si waveguide photodetectors

This chapter analyzes vertical *p-i-n* Ge-on-Si waveguide photodetectors using the metrics discussed in Chap. 2. A perspective view is shown in Fig. 4.1.

The results presented here have been already reported, in part, in several research papers published during my PhD [57–61].

The chapter is structured as follows. After a description of the geometry, the simulations conducted in dark are reported, followed by those performed under illumination. The model is validated against dynamic measurements, and the effects of the electric field screening arising from strong optical injection are addressed. The final section of the chapter presents guidelines for the design of the next generation of VPIN WPDs.

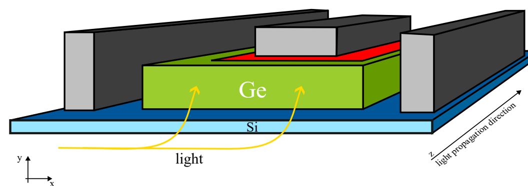

Fig. 4.1 Perspective view of a vertical *p-i-n* waveguide photodetector.

4.1 Device and geometrical quantities

The device under study consists of two primary components: the silicon substrate and the germanium absorber. The Si substrate is heavily doped, causing the semiconductor to become degenerate, whereas the Ge absorber is mainly intrinsic, except for a small layer that has been implanted at the interface with the metal contact layer on the top. The doping values employed in this study exceed $10^{19}\,\mathrm{cm}^{-3}$ in both areas. The metal contacts are positioned above and adjacent to the germanium absorber, creating a vertical *p-i-n* junction. The elements silicon, germanium, the implanted region, and metals are all aligned in relation to each other.

The key geometric characteristics of this device are the width (W_{Ge}), height (L_{Ge}), and depth (H_{Ge}) of the Ge absorber, as well as the width (W_{Si}), height (H_{Si}), and depth (L_{Si}) of the silicon region. Additionally, it is crucial to consider the width of the implanted doped region, represented as W_{doping}, as it directly impacts the electric field within the device and, consequently, the speeds of the carriers. It is important to highlight that in this device it is possible to switch the doping configuration, resulting in two different arrangements of dopants. When n-type dopants are added to silicon, the implanted region will become p-type, and vice versa. This determines whether it is a p-on-n or n-on-p configuration.

In Fig. 4.2, two cross-sections, transverse and longitudinal, are shown, along with important geometrical quantities. This chapter's reference structure has a germanium width of $W_{\mathrm{Ge}} = 4\,\mu\mathrm{m}$, a height of $H_{\mathrm{Ge}} = 0.8\,\mu\mathrm{m}$, and a length of $L_{\mathrm{Ge}} = 15\,\mu\mathrm{m}$. The germanium has a doped region and a guard ring measuring $0.5\,\mu\mathrm{m}$ on both sides. This gives a total width of $W_{\mathrm{doping}} = 3\,\mu\mathrm{m}$, and $W_{\mathrm{metal}} = 1.5\,\mu\mathrm{m}$.

The final quantity that will be discussed is the height of the doped region in Ge. The low electric field in this region determines the absorber's effective active height.

A waveguide coupling the input light connects with a long taper ($> 40\,\mu\mathrm{m}$) the silicon substrate. The taper is long and wide enough to have no noticeable effect on the figures of merit. The light that enters the substrate is then evanescently coupled into the Ge absorber. Metals, typically tungsten, serve

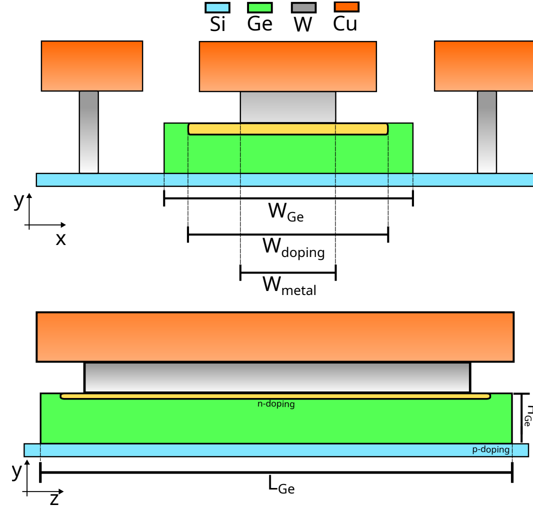

Fig. 4.2 Transverse (xy, top) and longitudinal (yz, bottom) cross sections of the VPIN WPD structure under study with its most significant geometrical parameters. The Ge absorber is grown on top of the Si substrate; top and lateral metallic contacts are placed on the absorber and on the substrate, respectively. Ge is considered to be intrinsic (green), with the exception of a n^+ layer resulting from ion implantation below the Ge–metal contact (yellow), while Si is heavily p-doped (blue). A 40 µm-long tapered waveguide (not shown) injects light into the substrate.

an important optical function, i.e. the metal surface reflects incident light, making the width of the metal, represented as W_{metal}, the least influential factor. Finally, the model accounts also for the first metal layer of copper (Cu).

Table 4.1 provides a list of geometric reference values.

4.2 Device in dark

This section focuses on examining the device in the dark and start with describing the equilibrium condition without any applied bias. Here, a comparison is conducted between the two potential options, p-on-n and n-on-p. An analysis is then performed to determine the impact of the generation and recombination rates for different reverse bias, as well as the IV curve. Ultimately, the analysis of small electrical signals is presented, with the goal of determining the impedance of the device.

Table 4.1 Summary of geometrical parameters of the reference device

Parameter	**Symbol**	**Reference Value**
Width of germanium	W_{Ge}	4 µm
Height of germanium	H_{Ge}	0.8 µm
Length of germanium	L_{Ge}	15 µm
Width of silicon	W_{Si}	9 µm
Height of silicon	H_{Si}	0.12 µm
Length of silicon	L_{Si}	15.5 µm
Width of implanted region	W_{doping}	3 µm
Width of metal	W_{metal}	1.5 µm

In Fig. 4.3, you can see the equilibrium energy band diagrams for the reference device in two different configurations: n-on-p (a) and p-on-n (b). The diagrams represent a vertical cut from the top metallic contact, via the germanium layer, to the silicon substrate. The x-axis reflects the position within the device, where $y = 0$ indicates the junction interface between the Ge and Si. The y-axis represents the energy levels in eV. The removal of the valence band discontinuity between germanium (Ge) and silicon (Si) has been achieved by including a thin graded interface, measuring a few nanometers, between the two materials. This aspect was reported in a study by VandeWall et al. in 1986 [62] and further confirmed by Palmieri et al. in 2018 [63].

The current-voltage (I-V) characteristics for two different junction topologies, p-on-n and n-on-p, are observed in Fig. 4.4 under dark conditions. The blue curve represents the p-on-n configuration, whereas the orange curve corresponds to the n-on-p configuration. The n-on-p configurations shows an higher dark current due to the higher intrinsic carrier density at the graded interface. If the values are compared to literature values[1], there are several order of magnitude difference. Modeling and matching the dark current requires a deep knowledge of the device compared to, about the defects, SRH lifetimes, traps, other effects like interface defects [64–66].

This behavior of defects impacting the I-V curve is clear if we compare the different generation and recombination mechanism averaged in germanium as a function of the bias, reported in Fig. 4.5. All the rates represent the averaged

[1] Literature devices, both simulated and experimental, agreed on responsivity close to the theoretical limit of the device.

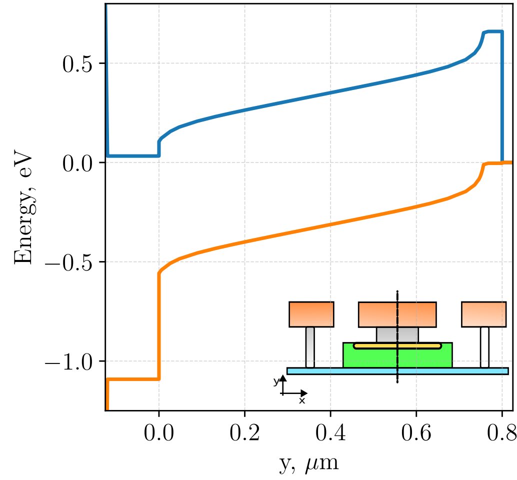

(a)

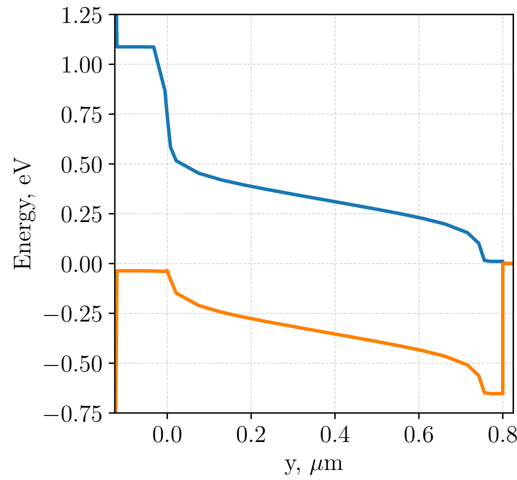

(b)

Fig. 4.3 Band diagram at equilibrium for reference device in (a) p-on-n (b) n-on-p configurations

rate over the germanium region, for the n-on-p configuration. The absolute value is reported and they are all generating carriers, in particular SRH, which is the highest among them. This dominant effect can be effectively modeled by introducing traps and changing the lifetime of the material, impacting in this way by several order of magnitude on the dark current.[2]

[2]This modeling choice implies a deep knowledge of the technology and the fabrication process.

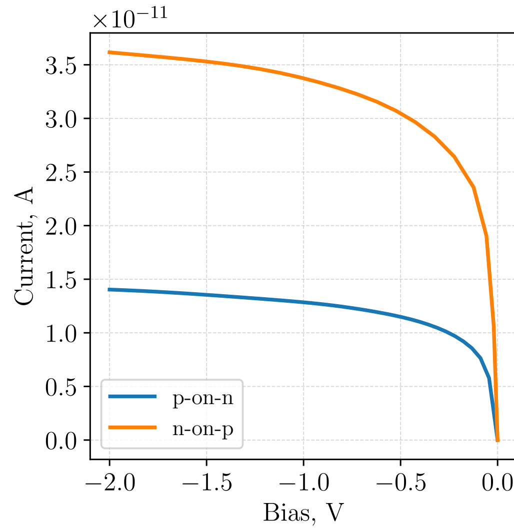

Fig. 4.4 Comparison of I-V characteristics in dark condition of p-on-n and n-on-p configuration. The blue curve, representing the p-on-n curve is lower than the orange n-on-p curve due to the difference in intrinsic carrier densities and the n-on-p graded interface.

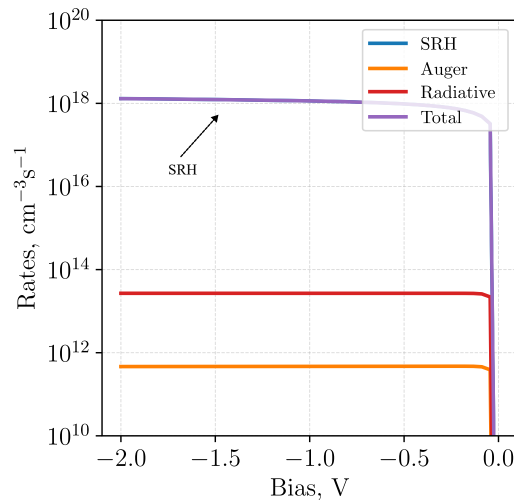

Fig. 4.5 Generation rates in dark of n-on-p configuration, avereged on the germanium region. The dominant effect is SRH, coincident with total rate, for the entire applied bias range by several order of magnitude

The last aspect to be discussed before illuminating the device is to extract the small signal parameter, to understand the RC limitation introduced in the design. Fig. 4.6 reports the real (Fig. 4.6a) and imaginary (Fig. 4.6b) part of the magnitude of the tranfer function. The simulations have been computed

both with and without the first Cu metal layer. Then, the circuit shown in Fig. 4.7 is used to fit and extract the parameters. The Cu layer has almost no effects on the real part, while there is a significant difference for the imaginary part. In fact, the imaginary part is the reactance, connected to the capacitances present in the device. In order to extract the parameters, the simulation must be carried out for high frequencies, where the effect of the pole can be clearly seen. The small signal equivalent circuit model is inspired by [1, Ch. 4], as describe also in Sec. 2.4, and reports two capacitor C_1 and C_2 and a resistor R. C_1 and R can be considered "intrinsic" components, while C_2 is the parasitic contribution. For low frequency, the impedance is affected by both capacitor, while for very high frequency only C_2 still contributes.

Fig. 4.6 also report the analytic fitting, and from this the parameter used were $R = 33\,\Omega, C_1 = 9.25\,\text{fF}, C_2 = 3.2\,\text{fF}$. Removing Cu, R remains the same, but $C_1 = 9.25\,\text{fF}, C_2 = 2.03\,\text{fF}$, indicating a significant impact of the first metal layer as well. While R is almost constant, C_1 can be safely approximated to a parallel plate capacitor:

$$C_1 \approx \varepsilon_0 \varepsilon_r \frac{A}{H_{\text{Ge}}} = 8.85 \times 10^{-16}\,\text{F/µm} \cdot 16.2 \cdot \frac{15\,\text{µm} \cdot 4\,\text{µm}}{0.8\,\text{µm}} = 10.7\,\text{fF} \tag{4.1}$$

In Fig. 4.6, C_1 can also be easily extracted by subtracting the two plateau values.

4.3 Device under illumination

The I(V) characteristics presented in Figure Fig. 4.8 shows the response of the measured reference structure when subjected to bias in dark conditions and under illumination of 0 dBm[3], measured at the input optical waveguide, before coupling. The blue curve is the dark current, which remains substantially constant (in the µA range) as the reverse bias increases. The flat response under illumination across the applied bias range suggests that the photo-generated carriers are efficiently collected, leading to a saturated photocurrent. The

[3] $x[\text{dBm}] = 20\log(\frac{x}{1\,\text{mW}})$

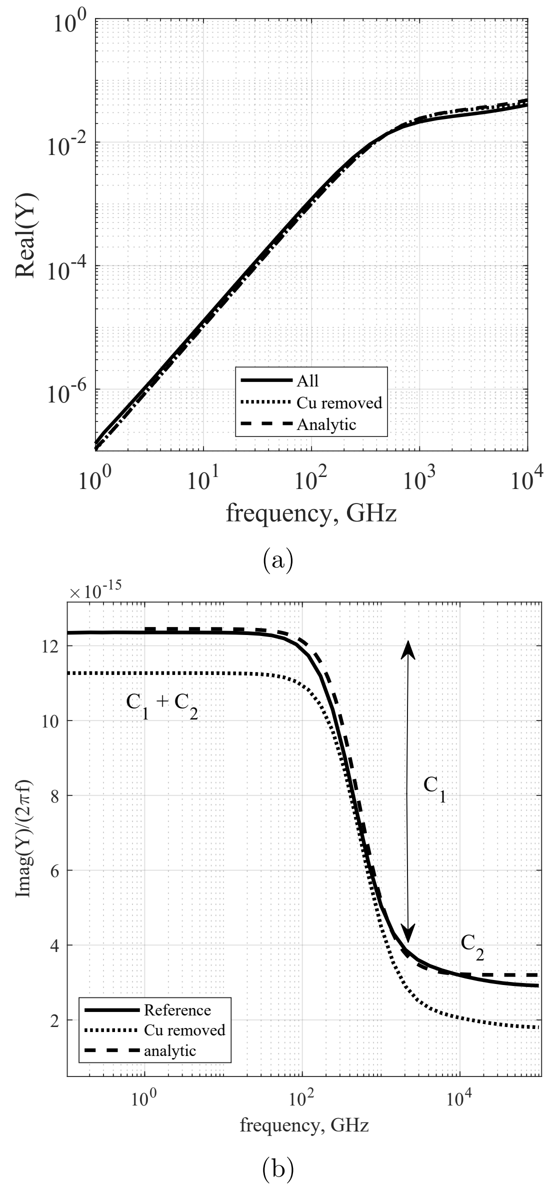

Fig. 4.6 Real and imaginary part of the electrical small signal model evaluated with the model and fitting with an analytic model to extract R and C components. The circuit is reported in Fig. 4.7, with $R = 33\,\Omega, C_1 = 9.25\,\mathrm{fF}, C_2 = 3.2\,\mathrm{fF}$.

difference of several order of magnitude between the measured dark current and the photocurrent, shows that this design present a good signal to noise ratio, with high responsivity.

Fig. 4.9 shows the calculated optical generation rate within the germanium absorber layer of the Device 2 under investigation. The color maps depict the

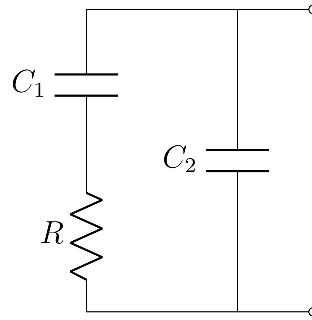

Fig. 4.7 Small signal circuit model used to fit the numerical model.

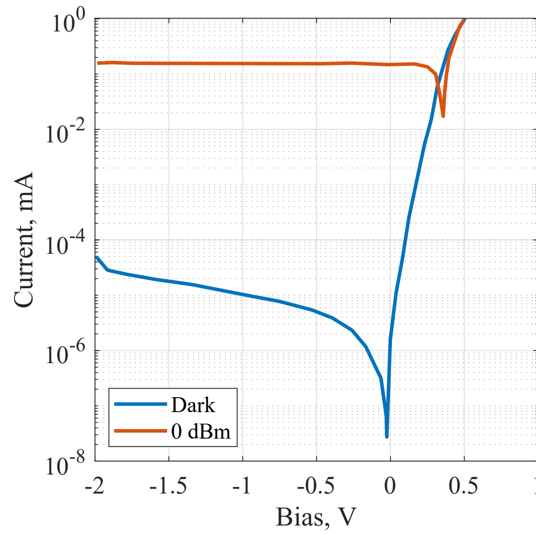

Fig. 4.8 Experimental $I(V)$ characteristics of a sample of Device 2 (reference) in dark (blue line) and under 0 dBm illumination (orange line).

number of electron-hole pairs generated per cubic centimeter per second as a function of position within the absorber, for an input optical power of 200 µW. On the left, the transverse (xy) cross-section at $z = 1.8$ µm from the waveguide entrance illustrates the light distribution profile, indicating strong confinement and intensity peaks within the waveguide. On the right, the longitudinal (yz) cross-section at the device center shows how the light intensity diffuses and diminishes along the propagation direction (z), with notable variations in generation rate. These patterns are critical for understanding how light is absorbed in the device and how it impacts carrier dynamics and device performance. The variation in G_{opt} along the propagation direction, especially the attenuation and interference effects, underlines the necessity of optimizing

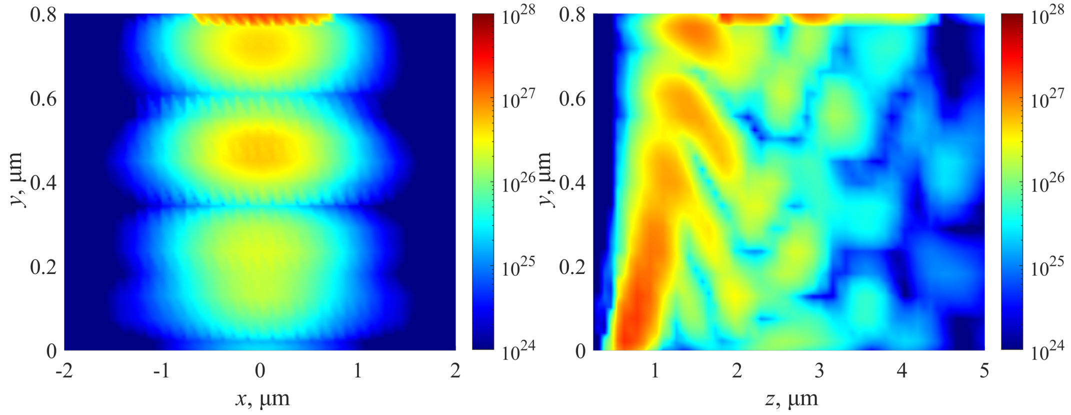

Fig. 4.9 Optical generation rate $G_{\mathrm{opt}}(x, y, z)$ ($\mathrm{cm}^{-3}\mathrm{s}^{-1}$) in the Ge absorber of Device 2 for an input optical power 200 µW. (Left) Transverse (xy) cross section for $z = 1.8$ µm, where z is measured from the beginning of the absorber. (Right) Longitudinal (yz) cross section for $x = 0$ (corresponding to the device center) and $z \in [0, 5]$ µm.

waveguide design for efficient light coupling and absorption in waveguide photodetectors.

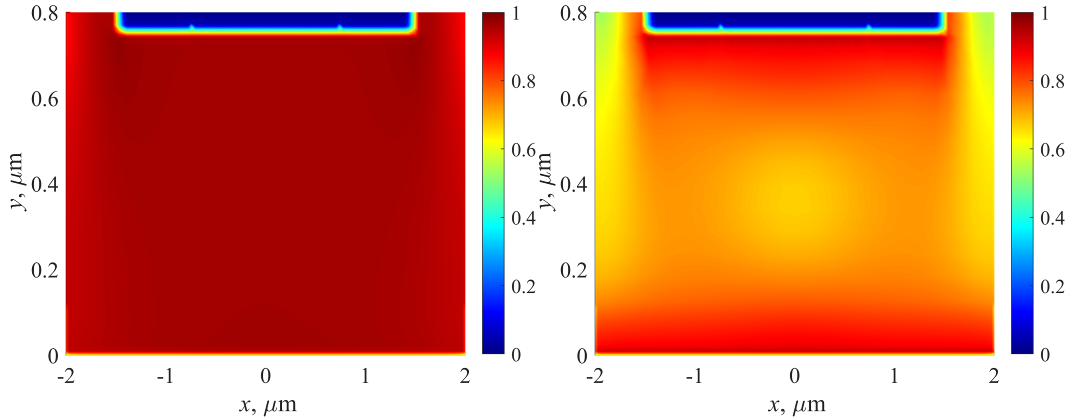

Fig. 4.10 Magnitude of the electron drift velocity normalized with respect to the saturation velocity, $|v_n(x, y, z)|/v_{\mathrm{sat}}$, in the transverse ($xy$) cross section of the Ge absorber of Device 2 at $z = 1.8$ µm for an input optical power 200 µW. (Left) -2 V bias voltage. (Right) Zero bias voltage.

Fig. 4.10 displays the relative electron drift velocity across the transverse (xy) cross-section of the Ge absorber in Device 2, for an input optical power of 200 µW at a depth of $z = 1.8$ µm. The velocity is normalized to the saturation velocity v_{sat}, which is the maximum velocity electrons can attain under the influence of an electric field in Ge. The image on the left reports the electron velocity distribution under a reverse bias voltage of -2 V. The high electric field

results in high drift carrier velocity. The right image illustrates the distribution at zero bias voltage, where diffusion plays a more dominant role due to the low value of the electric field. The differences between these two conditions highlight the impact of biasing on carrier transport within the device. Such visualizations are vital for optimizing the device structure to maximize carrier extraction and minimize recombination, which can improve the speed and efficiency of photodetectors.

Fig. 4.11 illustrates the electro-optic frequency response of Device 2 under a bias of −3 V. The dashed blue curve represents the simulation results, while the solid black curves are the experimental measurements of five nominally identical samples. The close agreement between simulation and measurements suggests that the model captures the essential physics governing the device behavior up to frequencies of about 50 GHz. All curves show a 3 dB bandwidth well above 30 GHz, confirming the high-speed capability of the device. The slight deviations between different samples may be attributed to manufacturing variances, which affect the high-frequency performance to a certain extent. The consistent rolloff beyond the 3 dB point underscores the importance of parasitic effects and carrier transit times in limiting the response at higher frequencies.

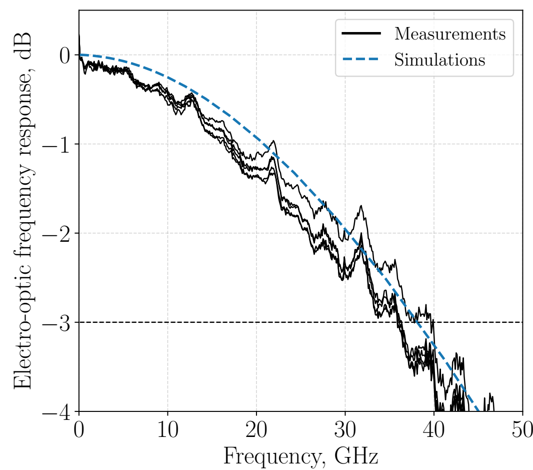

Fig. 4.11 Simulation (dashed blue curve) and measurements (black curves) of five nominally identical samples of reference device, for a bias voltage of −2 V.

4.4 Validation of the model

The multiphysic model is validated against several different device variants, which are fabricated and characterized. The reference geometry and its variants, depicted in Table 4.2 and Fig. 4.2 shows the influence of geometric parameters on device performance. Through a series of carefully crafted device variants, we examine the impact of varying the absorber width, W_{Ge}, and doping profiles W_{doping} on the device's "speed", thus providing insights into the electro-optic bandwidth optimization for high-speed photonic applications. Device 2 is the reference device described in Sec. 4.1,

Table 4.2 Geometrical parameters of the devices under study (see Fig. 4.2). Device 2 corresponds to the nominal geometry (reference). For all devices, $L_{\mathrm{Ge}} = 15\,\mu\mathrm{m}$ and $H_{\mathrm{Ge}} = 0.8\,\mu\mathrm{m}$, except for Device 6 where $L_{\mathrm{Ge}} = 18.5\,\mu\mathrm{m}$. The last column reports the simulated responsivity at a bias voltage of $-3\,\mathrm{V}$ and input optical power $200\,\mu\mathrm{W}$.

Device	W_{Ge}	W_{doping}	W_{metal}	W_{taper}	$\mathcal{R}$
1	4.0 µm	3.5 µm	1.5 µm	3.0 µm	0.84 A/W
2 (Reference)	4.0 µm	3.0 µm	1.5 µm	2.0 µm	0.89 A/W
3	3.0 µm	2.5 µm	2.0 µm	3.0 µm	0.76 A/W
4	3.0 µm	2.0 µm	1.5 µm	2.0 µm	0.79 A/W
5	1.5 µm	1.3 µm	1.0 µm	1.5 µm	0.79 A/W
6	1.0 µm	0.8 µm	0.5 µm	0.8 µm	0.81 A/W

The responsivity is reported in Table 4.2. The difference between the samples is due to the difference in the width of the taper and the width of the germanium absorber, that is not kept constant due to technological limitation.

As seen in Fig. 4.12, the multiphysics model captures the intricate behavior of various device configurations under different bias voltages. Each sub-figure illustrates the relationship between the cutoff frequency and the bias voltage, with experimental data shown in dashed lines and simulations in solid black lines. From the figure we can observe that the theoretical limit predicted in Sec. 2.4 is 10 GHz higher that most of the devices, resulting in possible further optimization of the device. Device 1 and 2 have the same germanium width, but Device 1 has wider implanted region, resulting in a wider bandwidth. The same happen for Device 3 and 4.

Voltage scaling is critical in minimizing power consumption for low-power applications, but it can adversely impact device performance. To tackle this,

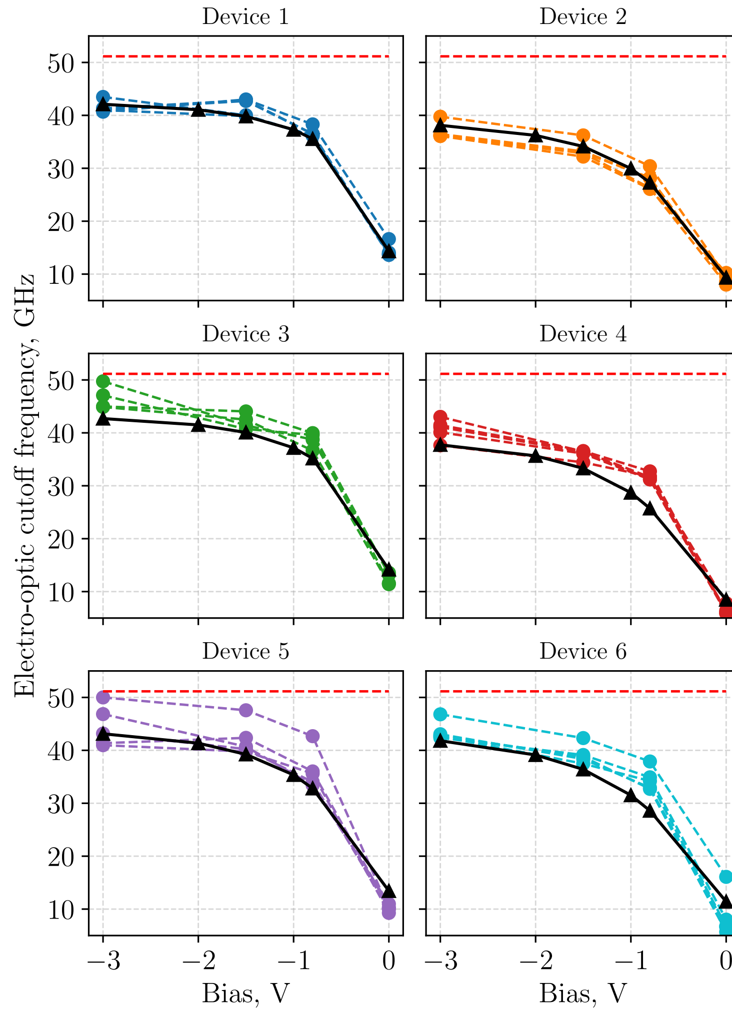

Fig. 4.12 Experimental values of f_{cutoff} as a function of the bias voltage for the six device variants whose geometry is reported in Table 4.2 (dashed lines), compared with the corresponding simulated curves obtained with calibrated P_{tot} (black solid lines). The horizontal red dashed lines correspond to the (bias-independent) transit-time limit according to the closed-form model of [1, Sec. 4.10.1].

our multiphysics model has been rigorously validated against experimental data, focusing on the bias voltage influence on device operation. Notably, all devices maintain a cutoff frequency close to or above 10 GHz even at zero bias, validating our model's ability to predict device performance accurately, which is crucial for designing low-power waveguide photodetectors.

Lastly, Device 5 and 6 are the smallest devices. They have they highest uncertainty in the measurements with high variability in the measured cutoff frequency, suggesting a lower yield in the fabrication process.

4.5 Impact of implanted region

This section illustrates how variations in the width of the germanium implanted doping region affect the bandwidth in the reference device. The electric field is more uniformly distributed in the larger implanted region and more concentrated within the device with the smaller implanted region, with corner with reduce value of the electric field. Fig. 4.13 shows the cutoff frequency as a function of implanted region width W_{doping}, maintaining a constant doping layer height of 50 nm and applied bias values of -2 V and -0.8 V. In both scenarios, we see an abrupt decrease from about 35 GHz to below 10 GHz in the smallest case. In the -2 V case the impact is noticeable below $W_{\text{doping}} = 3\,\mu\text{m}$. The impact is greater for the -0.8 V case, where the maximum bandwidth is already constrained by the lower electric field, that is just enough to allow the carriers to reach saturation velocity. This results in a low bandwidth even with the maximum extent of the doped region, with a noticeable change already at 3.5 µm.

It is not possible to cover the doped region entirely to the width of the germanium due to the need for a guard ring for manufacturing purposes, but this illustrates how the more doped region there is, the greater performance the device may provide.

4.6 Electric field screening effect

The experimental setup used in Cisco Systems is based on a Keysight LCA [67], which allows electro-optic measurements up to 50 GHz. Five nominally identical photodetectors, taken from different wafer regions, were characterized, determining mean value and standard deviation of the electro-optic cutoff frequency at different input optical powers for all the samples.

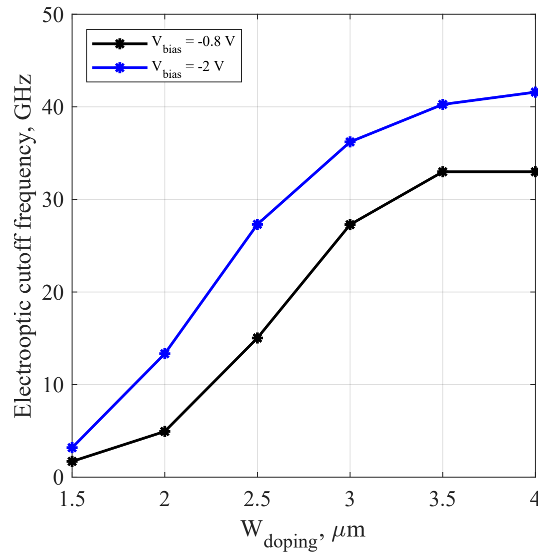

Fig. 4.13 Variation of the electro-optical bandwidth as a function of the extension (width) of the germanium implanted region W_{doping}, for fixed doping implantation height $H_{\text{Ge}} = 50\,\text{nm}$ and two bias voltages. Both the $-0.8\,\text{V}$ (black) and $-2\,\text{V}$ (blue) curve shows significant bandwidth drop close to $W_{\text{doping}} = 3\,\mu\text{m}$.

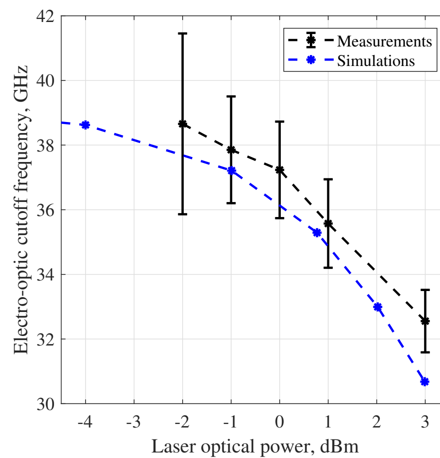

Fig. 4.14 Electro-optic cutoff frequency as a function of the optical power measured at the laser output.

Fig. 4.14 compares measurements and simulations of the electro-optic cutoff frequency at a reverse bias of $3\,\text{V}$ and at different optical powers as measured at the laser output. (The optical power assigned in the simulations takes into account the losses between laser and detector due to fiber coupling and waveguide propagation, estimated to be $3\,\text{dB}$ overall.)

In the figure, along with the simulation results (blue dots), are reported the mean values of the experimental electro-optic cutoff frequencies over five nominally identical devices (black dots), while the error bars represent the standard deviation of the measurements. An excellent match between measurements and simulations is observed for all the measured powers.

Increasing the optical power from −2 dBm to 3 dBm, the electro-optic cutoff frequency is reduced by more than 20 %. This decrease can be explained in terms of a reduction of the carrier velocity due to a screening of the electric field in Ge by the photogenerated carriers. The magnitude of this effect is shown in Fig. 4.15, which reports the absolute value of the electric field evaluated along a 1D vertical cut, from metal to silicon substrate, near the beginning of the absorber. At low input optical power (10 µW) the electric field is coincident with its profile in dark. On the contrary, at an optical power of 500 µW, the peak value of the electric field is reduced by a factor 3. This drop affects the device performance since the photogenerated carriers do not reach the saturation velocity, hence decreasing the electro-optic cutoff frequency.

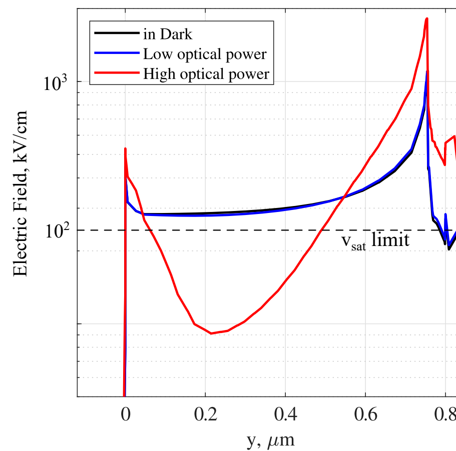

Fig. 4.15 Magnitude of the electric field in Ge along a 1D vertical cut between the center of the top metal contact and the silicon waveguide, at a distance of 1 µm from the front section of the absorber.

The screening effect we have observed is a nonnegligible limitation to the performance of waveguide photodetectors in the O-band and should be taken into account in the device design. The excellent match demonstrated here between measurements and simulations suggests that the multiphysics 3D

modeling approach provides a realistic description of this effect and can be used as an effective tool in device optimization towards the new device generation.

4.7 Design guidelines

From the results of our simulation campaign, we summarize in this Section some design guidelines that can lead to the development of Ge-on-Si VPIN WPDs compatible with 200 Gbit/s communication systems, *i.e.*, with a bandwidth in excess of 60 GHz, even without recourse to extrinsic parameter engineering.

The first guideline regards the width of the doping implantation region at the metal–Ge contact. From Fig. 4.12 one may observe that Device 1 has a wider bandwidth than Device 2, and the same can be said for Device 3 with respect to Device 4. Each pair has the same W_{Ge} but a different W_{doping}, as reported in Table 4.2, and a better performance is observed when the ratio $W_{\mathrm{doping}}/W_{\mathrm{Ge}}$ is closer to 1. In general, one should aim at a dopant implantation area which extends as much as possible to the whole upper surface of the absorber, since in the ideal case $W_{\mathrm{doping}} \approx W_{\mathrm{Ge}}$ one would observe an almost vertical electric field everywhere in Ge, favorably impacting the carrier velocity distribution.

Additional recommendations come from a set of simulations focused on the effects of W_{Ge} and H_{Ge} on f_{cutoff} and $\mathcal{R}$, for different values of the bias voltage in the interval $[-2,\, 0]$ V.

Fig. 4.16a shows the variation of f_{cutoff} for $W_{\mathrm{Ge}} \in [1,\, 6]$ µm, With W_{doping} adjusted to maintain a constant ratio $W_{\mathrm{doping}}/W_{\mathrm{Ge}}$, and all other dimensions equal to the reference. The bandwidth dependence on W_{Ge} observed in Fig. 4.16a is weakly non-monotonic, and f_{cutoff} reaches a maximum for $W_{\mathrm{Ge}} \approx 3$ µm.

The effect of H_{Ge} is more significant, as shown in Fig. 4.16b, where f_{cutoff} is reported for $H_{\mathrm{Ge}} \in [0.2,\, 1.2]$ µm, while keeping all other dimensions as in Device 2. Fig. 4.16b suggests that reducing H_{Ge} should prove convenient, since an electro-optic cutoff frequency above 60 GHz is obtained for $H_{\mathrm{Ge}} = 0.3$ µm at a bias voltage of -2 V.

The behavior of f_{cutoff} as a function of W_{Ge} and H_{Ge} in Fig. 4.16 is qualitatively consistent with the closed-form study in [1], where the transit time and

the parasitic RC product are presented as the two main elements that limit the bandwidth. For the device under study, when H_{Ge} is decreased from 1.2 µm to 0.3 µm, the bandwidth becomes wider according to $f_{\mathrm{cutoff}} \propto v_{\mathrm{sat}}/H_{\mathrm{Ge}}$ as a result of a reduction of the transit time, which is the limiting factor in this region of the parameter space [1, Sec. 4.9.3]. Conversely, when H_{Ge} is further decreased below 0.3 µm, the observed bandwidth reduction can be attributed to the RC product, since $f_{\mathrm{cutoff}} \propto H_{\mathrm{Ge}}/S$ [1, Sec. 4.9.4], where S is the Ge detector area in the xy plane.

The detector geometry corresponding to the maximum value of f_{cutoff} is determined by the interplay between transit time and RC limits. However, when aiming at an overall device optimization, a careful balance is required to achieve high-speed operation while preserving light detection efficiency, a critical requirement for limiting the power consumption of SOI platforms. For this purpose, Fig. 4.17 allows to assess the impact of W_{Ge} and H_{Ge} on the detector responsivity.The responsivity is closely related to another important figure of merit, the energy consumption per bit e_c [68]. In the devices considered here, since the measured current exhibits a low sensitivity to the applied bias, e_c is proportional to $\mathcal{R}$. As a reference, the energy consumption per bit for a 10 Gbits modulation on Device 2 under an applied reverse bias of 2 V is of the order of $e_c = 35\,\mathrm{fJ/bit}$, comparable with the values reported in [68, Sec. III-D].

From Fig. 4.17a one may observe that the nominal H_{Ge} of Device 2 is near-optimal, since the marginal increase in f_{cutoff} that could be achieved by reducing the absorber width would be accompanied by a 12–15% decrease of $\mathcal{R}$. Conversely, Fig. 4.17b shows that halving the absorber thickness from 0.8 µm to 0.4 µm would provide an increase of about 25 GHz to f_{cutoff} at the cost of a 9% penalty on $\mathcal{R}$. Remarkably, a device with $W_{\mathrm{Ge}} \approx 4$ µm and $H_{\mathrm{Ge}} \approx 0.4$ µm should have an intrinsic bandwidth larger than 40 GHz even at very low or zero bias, which promises the possibility for an optimized device to operate at high speed with very low power consumption.

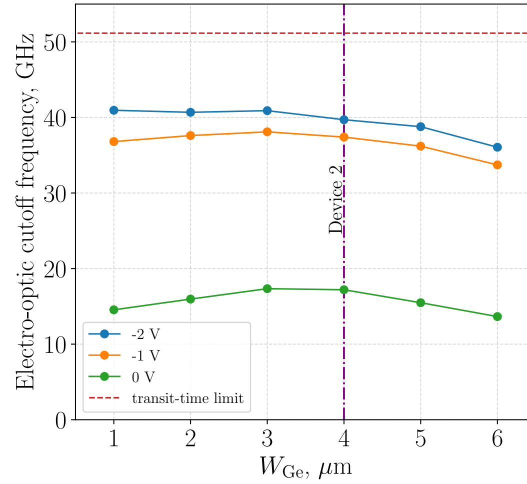

(a)

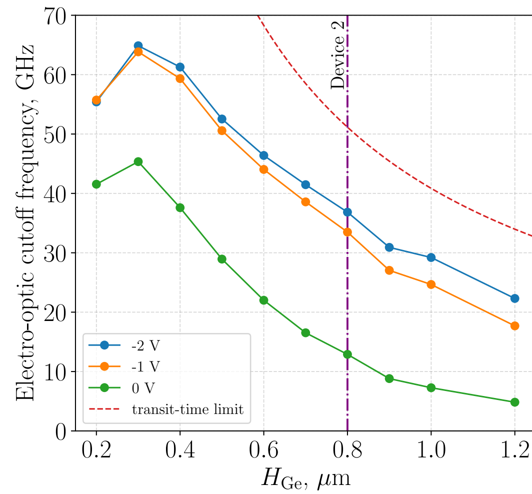

(b)

Fig. 4.16 Dependence of f_{cutoff} on (a) W_{Ge} and (b) H_{Ge}, starting from Device 2 (vertical dashed-dotted line), for input optical power 200 µW and bias voltage $[-2, -1, 0]$ V. The upper bound provided by the transit-time limit [1, Sec. 4.10.1] is reported as a reference (red dashed line).

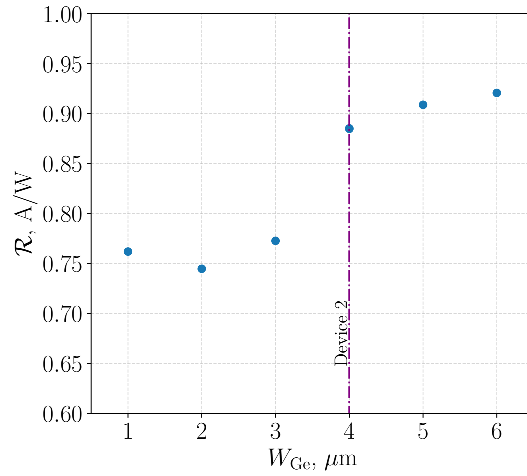

(a)

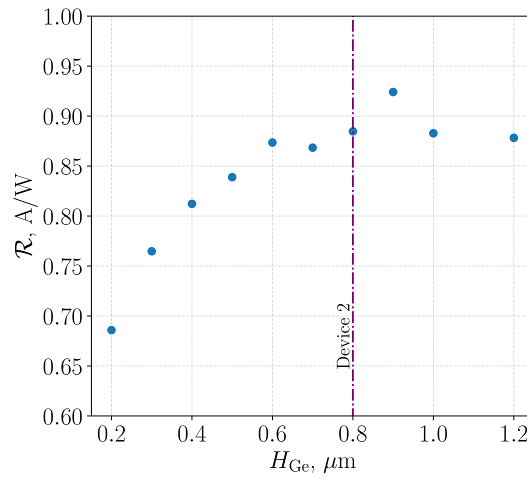

(b)

Fig. 4.17 Dependence of $\mathcal{R}$ on (a) W_{Ge} and (b) H_{Ge}, starting from Device 2 (vertical dashed-dotted line), for input optical power 200 µW and bias voltage −2 V. On the present plot, the values of $\mathcal{R}$ at lower bias (−1 V and 0 V) would be superimposed to the reported data points.

Chapter 5

Lateral *p-i-n* Ge-on-Si waveguide photodetectors

The results presented in this chapter have been in part already reported during my PhD [69, 70]. The lateral *p-i-n* WPDs under study are inspired by the the work of Lischke et al. [7], an example of an innovative fabrication technique that provides significant advancement in the field.

LPIN WPDs differ from the vertical devices studied in Chap. 4 due to the presence of silicon regions doped with opposite polarity surrounding the intrinsic germanium absorber region. This region, fabricated with FinFET-like processes, enables the creation of an extremely thin area, which reduces the time needed for photogenerated carriers to travel and exit the device, i.e. the transit time, consequently increasing the bandwidth. However, this also negatively impacts the responsivity of the device. When the width of the absorber is decreased in the lateral configuration, the interface with the substrate (through which light is evanescently coupled) also becomes smaller. This has an effect on the quantum efficiency and the responsivity (see Sec. 2.4).

Indeed, Lischke et al. [7] report an electro-optic bandwidth exceeding 200 GHz, but at the cost of a responsivity of approximately 0.3 A/W, significantly lower than that of vertical devices.

This structure is fascinating for investigating the dominant physical mechanisms within this compact device. However, it also raises several questions regarding the approach that should be employed for the simulation. The pri-

mary unresolved question pertains to the speed at which the photogenerated carriers move inside the device, specifically in the active region, and how they are influenced by the processes of generation and recombination. Moreover, how does the device react to various applied biases? What is the optimal voltage that maximizes both responsivity and electro-optic bandwidth?

I start this chapter by examining, as for the VPIN, the device in dark, followed by an analysis under illumination and concluding with an investigation of the dynamic characteristics, specifically focusing on the effects that germanium width has on the bandwidth, a crucial geometric parameter. All experimental data used for comparisons are extracted from [7].

Fig. 5.1 displays a cross-section view of the device, with the main geometric quantities labeled.

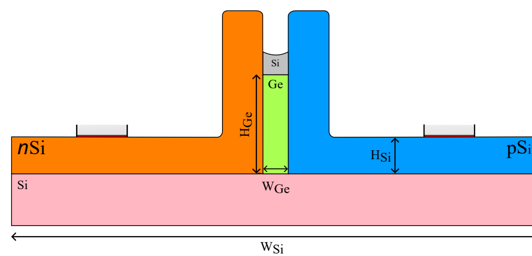

Fig. 5.1 Cross section of the lateral Ge-on-Si photodetector. The light is coupled with the absorber like for the vertical case, i.e. with a waveguide connected with a taper to the silicon substrate.

In Table 5.1 the quantities quoted in Fig. 5.4 are reported.

Table 5.1 Main geometrical quantity

Parameters	**Values, μm**
W_{Ge}	0.1
H_{Ge}	0.4
H_{Si}	0.15
W_{Si}	2.1
$H_{substrate}$	0.2

5.1 Device in dark

This section illustrate the device at equilibrium and under bias condition, *in-dark*. First we discuss the band diagram at equilibrium, then the IV curve and the generation mechanism.

Fig. 5.2 reports the band diagram at equilibrium both with (Fig. 5.2b) and without (Fig. 5.2a) a graded interface between germanium and (p)silicon. This device includes the germanium-(p)silicon and germanium-(n)silicon interface simultaneously, requiring the introduction of a graded interface for the presence of a valence band discontinuity in the germanium-(p)silicon junction, that represents challenges for the convergence of the model. However, the graded interface introduces a linear interpolated molar fraction profile between silicon and germanium of approximately 5 nm and it removes effectively the discontinuity. The graded layer is made as small as possible. [71]

Fig. 5.3 illustrates the comparison between the simulations and the values reported in the literature. The difference in magnitudes is expected due to the assumption made in our simulation model, which do not take into account interface and germanium epitaxial growth defect, adding traps and tuning SRH parameters. In fact, Fig. 5.4 illustrates the behavior of various mechanisms under −2 V using solid curves to represent recombination rates and dashed curves to represent generation rates.

Among all the generation-recombination mechanisms, SRH is shown to be the most prominent, which confirms the assumptions made about the dark current shown in Fig. 5.3. The dominating mechanism is the primary factor contributing to the I_{dark} current and it can be used to fit the dark current. Unlike SRH, Auger and Radiative recombinations have much lower magnitudes, and they do not represent a major contribution to the current. In the silicon regions, instead, there are typical values of recombination rate are smaller, due to the high doping present in the regions.

Summarizing, even if the IV dark current is not fitted by the model, I decided to stick to the literature data for germanium and silicon SRH. Nevertheless the main mechanism responsible for driving the magnitude of the dark current is identified, and with more information on the fabrication process it is possible to fit also the dark current, for a comprehensive model.

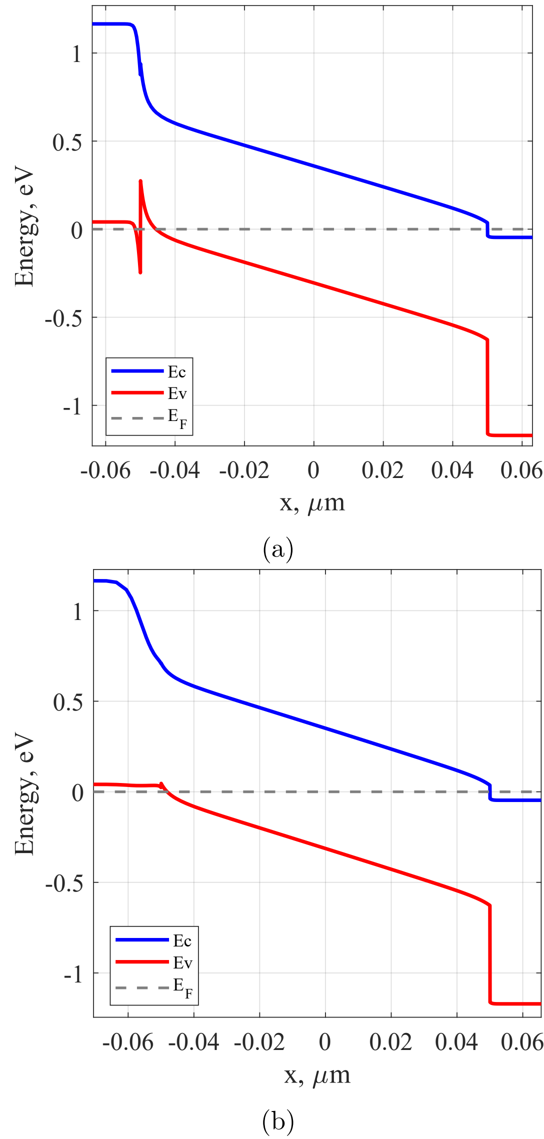

Fig. 5.2 Band diagram at equilibrium of the device in a 1D cut evaluated in 1D cut along the (n)silicon-germanium-(p)silicon junctions. (a) without graded interfaces, (b) adding a small linearly interpolated graded profile. The introduction of the graded profile remove the valence band discontinuity at $x \approx -50\,\text{nm}$, improving convergence. The other region are not affected by the graded region.

5.2 Device under illumination

To analyze the device under illumination, I will first present the results of the Finite-Difference Time-Domain (FDTD) simulation as the optical generation rate, shown in Fig. 5.5. Despite the device's small profile, the light can be

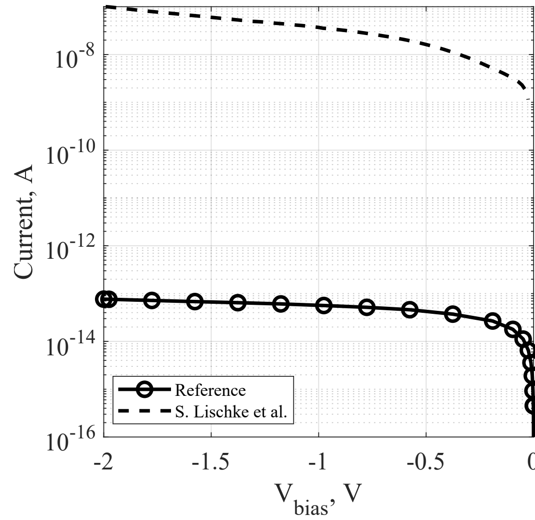

Fig. 5.3 IV characteristics of the device simulated compared with [7] data. A difference of several orders of magnitude are present, but comparing with Fig. 5.4, it is clear that defects not included in the model are the responsible for the difference.

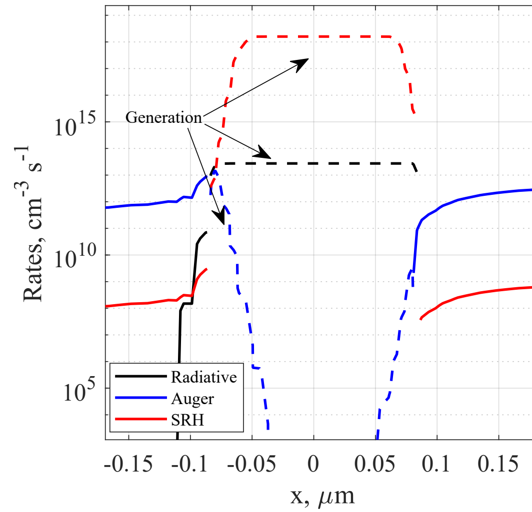

Fig. 5.4 Generation and recombination rate evaluated in 1D cut along the (n)silicon-germanium-(p)silicon junctions under $-2\,\mathrm{V}$ of applied bias. Solid lines represent recombination contribution, while dashed lines represents generative contribution. The depleted germanium shows high values of SRH generation, indicating that is the main actor also in the contribution of the IV curve.

effectively evanescently coupled within the active region. At the beginning of the device, there is a noticeable increase in the generation rate, but unlike the vertical device, the generation takes place more uniformly along the whole device. The simulations need significantly more time than the vertical counterpart, due

to the necessity of employing a sufficiently refined mesh to accurately depict the light's propagation and for the more distributed light, resulting in more scatterings and reflections. Fig. 5.5 illustrates a longitudinal cut seen from the top and laterally aligned on the same z-axis.

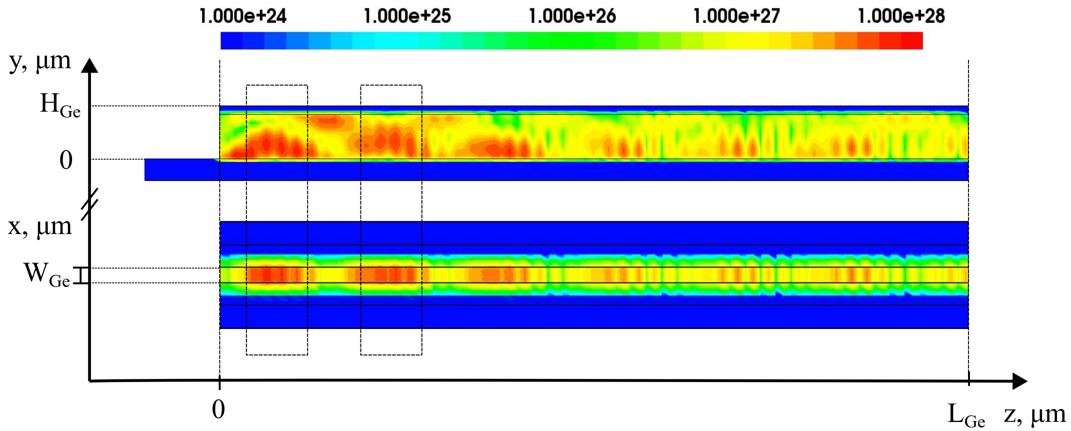

Fig. 5.5 Longitudinal cross section for the optical generation rate, with (top) a lateral cut, and (bottom) a top cut, aligned on the same axis.Even if there is an higher concentration of photogenerated carriers, the rate is distributed vertically and longitudinally more evenly with respecto to the VPIN.

Fig. 5.6 shows the photocurrent as function of the input optical power (PI curve), with the progressively raised optical power from 10 µW to a magnitude of 2 mW. The device exhibits linear behavior up to higher input optical powers, with a bias of -2 V. The measurements from the literature shows a difference with respect to the simulation. The simulation are carried out at a wavelength $\lambda = 1.31$ µm, where the absoption coefficient is well defined in the literature, while the measurements are carried out for $\lambda = 1.55$ µm. The absorption profile in the latter is right close to the edge of the absorption and Soriamello et al. [25] shows the dependencies of the absorption coefficient on the fabrication process. This effect is more and more evident as we approach the cutoff absorption above $\lambda = 1.55$ µm. So, a responsivity $\mathcal{R} \approx 0.7$ A/W can be determined from the simulation, overestimating the metrics. But the responsivity is dependent on the generation rate calculated with FDTD, that is linearly dependent on the absorption coefficient (see Appendix B).

Even if the model does not match the responsivity at the moment, it is possible to tune the input parameters, fitting the responsivity as well, for the chosen wavelength.

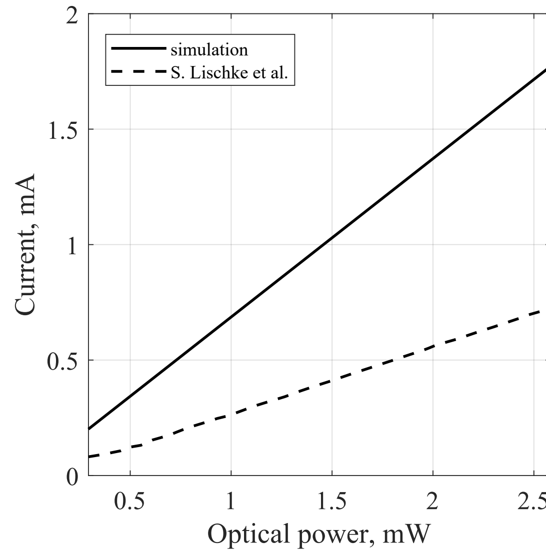

Fig. 5.6 PI curve for a bias of $-2\,\mathrm{V}$ compared with data from [7]. The difference between the simulation and the measurement is dependent on the sensitivity of germanium to the absorption coefficient close to the cutoff of $\lambda = 1.55\,\mu\mathrm{m}$.

Fig. 5.7 displays the electro-optic frequency response of the device, where $-3\,\mathrm{dB}$ is reported with a deshed line emphasising the cutoff frequency f_{cutoff}. Here the frequency response is compared with values obtained from the literature [7]. As mentioned in the paper, acquiring experimental data under these ultrawide band conditions is extremely challenging, leading to observations which are affected by so much noise that it can be hard to reduce the standard deviation of the measured cutoff frequency. Nevertheless, the model is capable of accurately replicating the behavior of the system and it reaches the experimental cutoff frequency of approximately 265 GHz. Sec. 5.4 will provide an explanation of the uncertainty regarding the cutoff frequency. It involves an examination of carrier saturation velocities, a quantity that is closely linked to the cutoff frequency throgh transit time. The simulation are performed with an applied bias of $-2\,\mathrm{V}$ for $\lambda = 1.31\,\mu\mathrm{m}$ and $\lambda = 1.55\,\mu\mathrm{m}$, but there are no significant difference between the two wavelengths, since the frequency response is almost only affected by the transit time.

To summarize this section, while the model does not accurately predict the exact value of dark-current and responsivity, it does demonstrate how generation and recombination factors contribute to these variations and their influence on

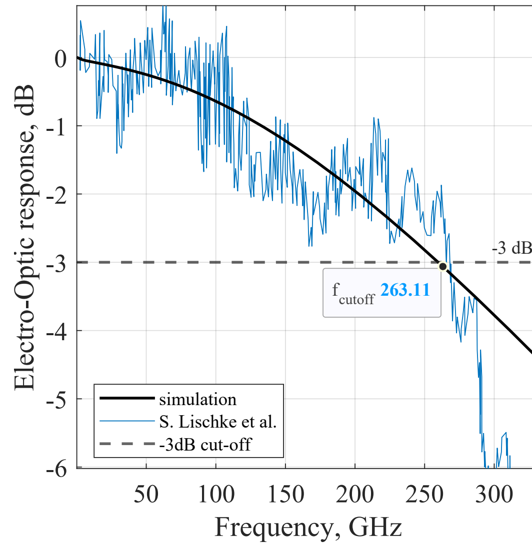

Fig. 5.7 Electro-optic frequency response at $V_{\text{bias}} = -2\,\text{V}$ compared with the literature [7]. The simulated response fit the measured data up to the cutoff frequency $f_{\text{cutoff}} \approx 265\,\text{GHz}$. Despite the noise superimposed to the measurements, due to the ultrawide bandwidth of the device, make hard to extract the exact cutoff frequency. Simulation are performed at $\lambda = 1.31\,\mu\text{m}$ and $\lambda = 1.55\,\mu\text{m}$ but no significant difference has been observed, due to the low responsivity values and the strong dependance on the saturation velocity (indipendent of the wavelength).

device performance. Nevertheless, the electro-optic frequency response and the cutoff frequency can be accurately predicted and studied under different bias condition. Finally, comprehending the microscopic functioning of the device enables the design process to be focused on industrial requirements, thereby optimizing the device while considering its overall performance.

5.3 Ge width investigation

Due to the device's thin dimensions, it is crucial to analyze the effects of the germanium width on the dynamic behavior. Lischke et al. [7] demonstrates an achievement that is challenging to overcome, but it comes at the expense of the device's responsivity. Using the model, we can now investigate and suggest solutions with varying germanium width W_{Ge} in order to identify a viable width that fulfills all the industry objectives and requirements.

Fig. 5.8 illustrates the correlation between the width of the device and the ratio between some generation recombination rate and the total generation-recombination rate. This graph displays the total amount of generation and recombination rates within the device, at $-2\,\text{V}$, as the width of the germanium material changes. The minimum efficiency corresponds to $W_{\text{Ge}} = 100\,\text{nm}$, while an increase of W_{Ge} leads to an increment of the efficiency. Conversely, if we decrease the width even more, for example if our focus is to increase even more the bandwidth, the ratio became more predomint in the favor of the avalanche generation rate. When comparing the results to the overall avalanche contribution, it becomes evident that the impact ionization is not only significant but also potentially greater than the contribution from optical generation. This suggests that although only a small amount of light is captured, the photogenerated carriers experience a strong electric field that facilitates impact ionization.

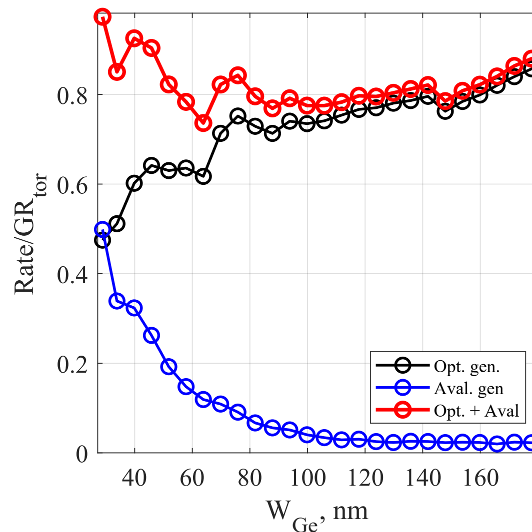

Fig. 5.8 Comparison on the quantum efficiency vs the Ge width.

Fig. 5.9 demonstrates the relationship between the cutoff frequency and the width of germanium. It is evident that this aligns with the analytical model depicted in Fig. 2.8. The margin and sensitivity to the width decrease inversely proportional to $1/W_{\text{Ge}}$, enabling us to identify tradeoffs in the design of these devices with exceptionally high bandwidth and quantum efficiency (and hence, responsivity). Expanding the active region really results in a substantial loss in bandwidth. However, even with a width of approximately

120 nm, the bandwidth remains within the range of 200 GHz. In contrast, when the thickness is significantly reduced below the nominal size, we see a quick fall in both RC contributions and generation-recombination rates.

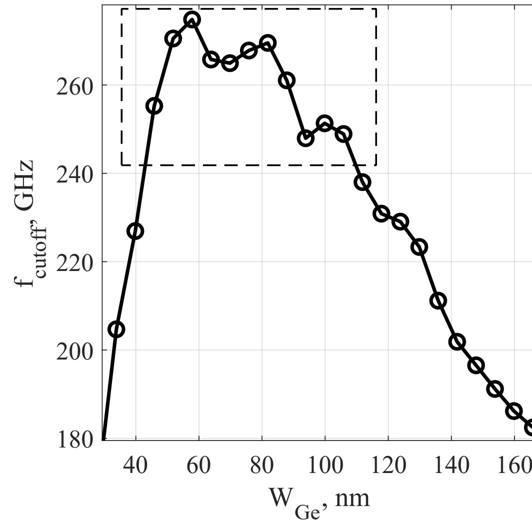

Fig. 5.9 Cutoff frequency as a function of the width of the device.

This effect can be seen in Fig. 5.10, where the quantum efficency is reported as a function of the width of the germanium. The nominal width of 100 nm corresponds to the minimum value of quantum efficiency, but increasing the width of the device results in a significant and even bigger rise, surpassing 15 %. Decreasing the width of germanium leads to a rise in quantum efficiency, which may be attributed to the occurrence of avalanche generating processes shown in Fig. 5.8. Here we can see that for larger width the quantum efficiency increase as well, due to the larger interface area between the silicon and the germanium, leading to more efficient light coupling.

5.4 Carrier velocities and frequency response

The last aspect to be explored is if the choice of drift diffusion as the modeling tool for this kind of devices is effective, or more complex simulation tools are required. In fact, the germanium layer, where the carriers are photogenerated, it is very small and carriers require time to reach the saturation velocity, that is what drift diffusion assumes.

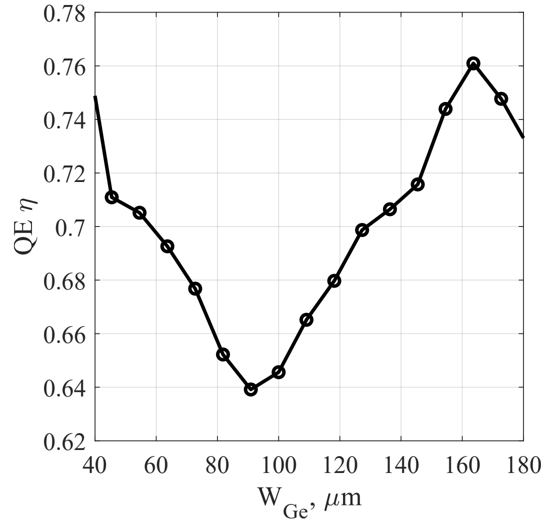

Fig. 5.10 Quantum efficiency η as a function of the width of the device.

Fig. 5.11 compares the calculated electro-optic frequency response with corresponding experimental data, for several values of the saturation velocity. As described in Sec. 2.4, a strong correlation between the frequency response and the saturation velocities is present, and that simple analytic model can be used also here. An increase from 0.74×10^7 cm/s to 0.84×10^7 cm/s makes the cutoff frequency to overcome $f_{\text{cutoff}} > 300$ GHz. Conversely, $V_{\text{sat}} = 0.64 \times 10^7$ cm/s make the cutoff frequency to overcome $f_{\text{cutoff}} < 250$ GHz, indicating a strong relationship.

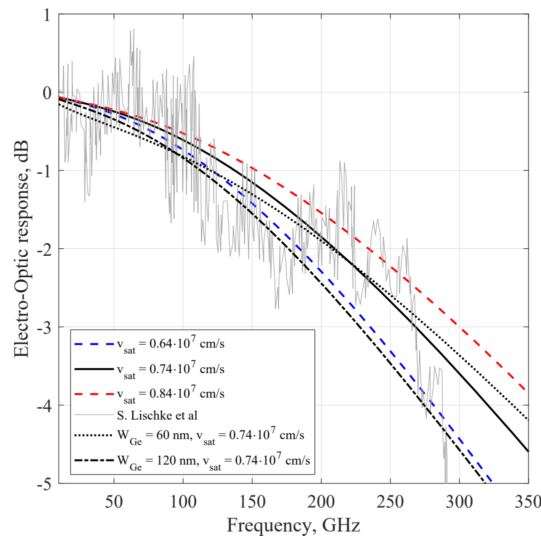

Fig. 5.11 Frequency response with different v_{sat} applied.

The f_{cutoff} are collected for several values of the saturation velocities for two different devices (nominal and with $W_{\text{Ge}} = 150\,\text{nm}$) and reported in Fig. 5.12. This plot demonstrates the relationship also in the 3D model between the two quantities, leading to devices highly sensitive to v_{sat}.

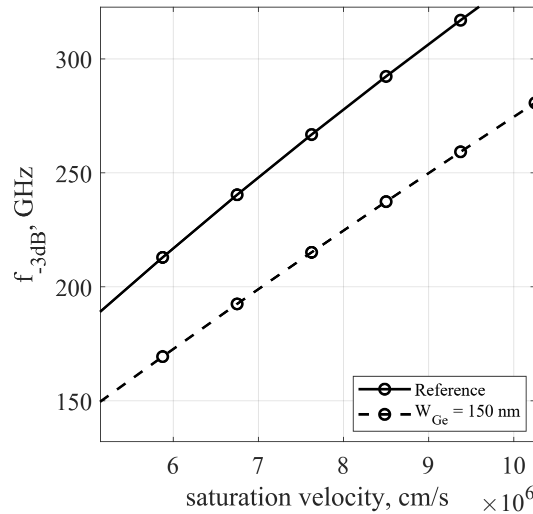

Fig. 5.12 Cutoff frequency as a function of v_{sat}, set equal for electrons and holes.

To prove this correlation, the discussion presents simulations using the novel Monte Carlo simulator developed by Professor Bellotti Lab at Boston University. This work has been presented in [70].

The simulation method changes drastically the paradigm of the simulation, introducing charge transport driven by the electric field and ruled by the Boltzmann transport equation (BTE). This innovative simulation method takes into account the full band energy dispersion relation of silicon and germanium, and it is particularly useful under high electric field condition, where particles scatter frequently.

The tool has been used to simulate the average velocity of an ensables of particles at specific point in space over the number of particles.

The velocity distribution, averaged on the particles ensemble, is presented in Fig. 5.13, with Fig. 5.13a reporting on electron velocities compared with drift diffusion saturation velocity, and Fig. 5.13b showing the averaged hole velocities compared with the drift diffusion velocity.

In both cases, the overshoot is significant, particularly in relation to the low dimension of the device. We simulated both the best and the worst case, i.e. a generation rate situated in the center of the germanium and at the silicon-germanium interface opposite to the carrier polarity. In this way there is the case where carries drift both for electrons and holes for the minimum space, and the case in which electrons and holes drift for the worst case.

Among the two carriers, holes show the higher average velocity, resulting in an overshoot that keeps the average of the carries over the saturation velocity for approximately 50 nm, namely half the width of the germanium absorber.

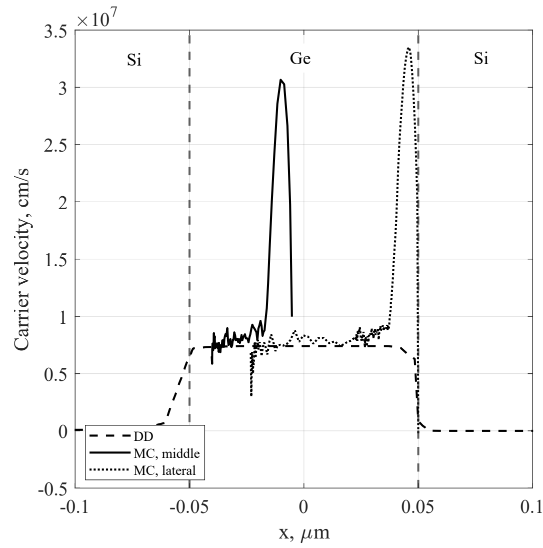

(a)

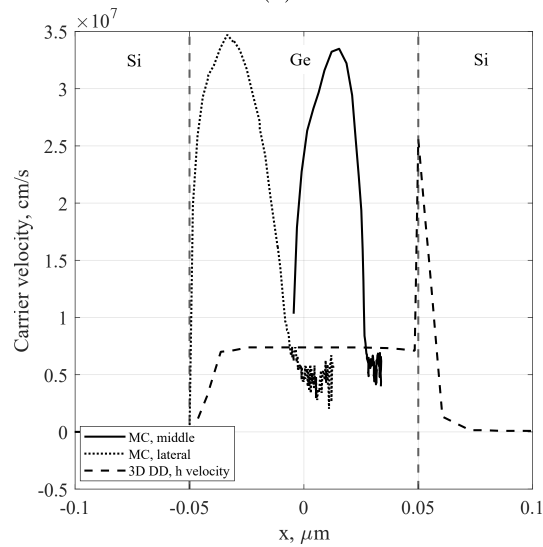

(b)

Fig. 5.13 Monte Carlo simulation of carriers in devices, comparing two cases fof electron and holes to the saturation velocity of drift diffusion. (a) electrons, (b) holes.

Chapter 6

Conclusions

This dissertation investigates the modeling of Ge-on-Si WPDs for data communications with the aim of maximizing their intrinsic frequency response and the bandwidth, involving both "conventional" VPIN devices that can be further optimized thanks to TCAD-assisted modeling, and innovative LPIN devices fabricated in a FinFET-like fashion, leading to impressive bandwidths, but at the cost of lowered responsivity and quantum efficiency.

In VPINs, initially the in-dark condition were studied, both at equilibrium for the two possible doping configuration, and for the IV characteristics, concluding with the extraction of the small signal parameters. Six device variants were characterized by Cisco System, proving that all variants achieved an electro-optic bandwidth of 40 GHz or more at $\lambda = 1310\,\mathrm{nm}$ for a reverse bias of $-2\,\mathrm{V}$, with the 3D multiphysics model capable of reproducing all the results.

In fact, the experimental results were used to validate the numerical model that combines a 3D FDTD electromagnetic solver and a electrical transport simulation based on drift diffusion. Since the multiphysics model was able to reproduce the experimental behavior with good accuracy, an extensive simulation campaign was carried our to identify design guidelines leading to maximum bandwidth. This campaign enabled the determination of values for W_{Ge}, W_{doping}, H_{Ge} that should provide the best performance from a trade-off between transit time and capacitive (RC) effects, while keeping the responsivity and the quantum efficiency at high standards.

Within this optimization campaign, the model predicts at zero bias a maximum intrinsic bandwidth close to the remarkable value of 45 GHz, allowing to employ Ge-on-Si VPIN WPDs in SOI platforms with the goal of reduced (or even zero) power consumption for the detector in the receiver block of the communication chain.

Using a higher but moderate bias voltage (*e.g.*, -2 V), a cutoff frequency larger than 60 GHz is expected, and the 4-level Pulse Amplitude Modulation (PAM-4) coding scheme should enable data transmission in excess of 200 Gbit/s.

The model also enable the understanding and the possibility to fit dark current and responsivity data, under more in-depth knowledge of the fabrication process, identifying the main mechanisms contributing to both dark current and photocurrent.

In LPIN devices, the simulations were carried out following the same path, but with experimental data taken from the literature. The ultrawide bandwidth can be predicted by the model, showing also the possible limitation of the approach, particularly in Fig. 5.13, where novel 3D Full Band Monte Calro aproach has been used to conduct a preliminary study on the effects of the overshoot velocity that the average of the carriers experience.

The validated model is then employed to extend the investigation of the detailed behavior of microscopic quantities, such as the velocities of photogenerated carriers, and will support further performance improvements, like the investigation proposed as a function of the germanium width, but also the generation and recombination mechanism that are involved as a function of the applied bias, leading to significant avalanche even under modest applied bias.

In conclusion, this 3D multiphysics model, that couples FDTD and 3D drift-diffusion simulations, paves the way to the design of novel photodetectors for silicon photonics platforms, with solutions that contribute to the reduction of power consumption and at the same time increase the transmission rate to address the new demands on data transfer rates, driven by AI and cloud computing.

References

[1] G. Ghione, *Semiconductor Devices for High-Speed Optoelectronics.* Cambridge, U.K.: Cambridge University Press, 2009.

[2] S. Y. Siew, B. Li, F. Gao, H. Y. Zheng, W. Zhang, P. Guo, S. W. Xie, A. Song, B. Dong, L. W. Luo *et al.*, "Review of silicon photonics technology and platform development," *Journal of Lightwave Technology*, vol. 39, no. 13, pp. 4374–4389, Jul. 2021. doi: 10.1109/JLT.2021.3066203

[3] T. Yin, R. Cohen, M. M. Morse, G. Sarid, Y. Chetrit, D. Rubin, and M. J. Paniccia, "31 GHz Ge *n-i-p* waveguide photodetectors on silicon-on-insulator substrate," *Optics Express*, vol. 15, no. 21, pp. 13 965–13 971, Oct. 2007. doi: 10.1364/OE.15.013965

[4] S. Fama, L. Colace, G. Masini, G. Assanto, and H.-C. Luan, "High performance germanium-on-silicon detectors for optical communications," *Applied Physics Letters*, vol. 81, no. 4, pp. 586–588, Jul. 2002. doi: 10.1063/1.1496492

[5] M. J. Byrd, E. Timurdogan, Z. Su, C. V. Poulton, N. M. Fahrenkopf, G. Leake, D. D. Coolbaugh, and M. R. Watts, "Mode-evolution-based coupler for high saturation power Ge-on-Si photodetectors," *Optics Letters*, vol. 42, no. 4, pp. 851–854, Feb. 2017. doi: 10.1364/OL.42.000851

[6] H. Cao, Y. Xiang, W. Sun, J. Xie, J. Guo, Z. Yu, L. Liu, Y. Shi, and D. Dai, "High-power ge/si waveguide photodetector," *ACS Photonics*, 2024.

[7] S. Lischke, A. Peczek, J. S. Morgan, K. Sun, D. Steckler, Y. Yamamoto, F. Korndörfer, C. Mai, S. Marschmeyer, M. Fraschke, A. Krüger, A. Beling, and L. Zimmermann, "Ultra-fast germanium photodiode with 3-dB bandwidth of 265 GHz," *Nature Photonics*, vol. 15, no. 12, pp. 925–931, Dec. 2021. doi: 10.1038/s41566-021-00893-w

[8] M. Poulin, C. Latrasse, M.-J. Picard, Y. Painchaud, F. Pelletier, and M. Guy, "Development of silicon photonic products for telecom & datacom," in *2015 IEEE 12th International Conference on Group IV Photonics (GFP)*, Vancouver, Canada, Aug. 2015. doi: 10.1109/Group4.2015.7305899

[9] L. Pavesi and D. J. Lockwood, *Silicon Photonics.* Berlin: Springer-Verlag, 2004.

[10] ——, *Silicon Photonics III. Systems and Applications.* Berlin: Springer-Verlag, 2016.

[11] D. Thomson, A. Zilkie, J. E. Bowers, T. Komljenovic, G. T. Reed, L. Vivien, D. Marris-Morini, E. Cassan, L. Virot, J. Fédéli, J. Hartmann, J. H. Schmid, D. X. Xu, F. Boeuf, P. O'Brien, G. Z. Mashanovich, and M. Nedeljkovic, "Roadmap on silicon photonics," *Journal of Optics*, vol. 18, no. 7, p. 073003, 2016. doi: 10.1088/2040-8978/18/7/073003

[12] L. Vivien and L. Pavesi, *Handbook of Silicon Photonics.* Taylor & Francis, 2013.

[13] M. Tada, J.-H. Park, D. Kuzum, G. Thareja, J. R. Jain, Y. Nishi, and K. C. Saraswat, "Low temperature germanium growth on silicon oxide using boron seed layer and in situ dopant activation," *Journal of Electrochemical Society*, vol. 157, no. 3, p. H371, Feb. 2010. doi: 10.1149/1.3295703

[14] A. E.-J. Lim, J. Song, Q. Fang, C. Li, X. Tu, N. Duan, K. K. Chen, R. P.-C. Tern, and T.-Y. Liow, "Review of silicon photonics foundry efforts," *IEEE Journal of Selected Topics in Quantum Electronics*, vol. 20, no. 4, pp. 405–416, 2014. doi: 10.1109/JSTQE.2013.2293274

[15] K. Research. (2023, June) Global silicon photonics market size, share & industry trends analysis report. KBV Research. Report Id: KBV-16086. Publication Date: June-2023. Number of Pages: 214. [Online]. Available: https://www.kbvresearch.com/silicon-photonics-market/

[16] W. Hu, X. Xie, Q. Xu, W. Zhang, and H. Song, "Research progress of SiGe heterojunction photodetectors," in *Seventh Symposium on Novel Photoelectronic Detection Technology and Applications*, vol. 11763, Proceedings of the SPIE, Kunming, China, Mar. 2021. doi: 10.1117/12.2588373 p. 11763A4.

[17] D. Chen, H. Zhang, M. Liu, X. Hu, Y. Zhang, D. Wu, P. Zhou, S. Chang, L. Wang, and X. Xiao, "67 GHz light-trapping-structure germanium photodetector supporting 240 Gb/s PAM-4 transmission," *Photonics Research*, vol. 10, no. 9, pp. 2165–2171, 2022. doi: 10.1364/PRJ.455291

[18] M. M. P. Fard, G. Cowan, and O. Liboiron-Ladouceur, "Responsivity optimization of a high-speed germanium-on-silicon photodetector," *Optics Express*, vol. 24, no. 24, pp. 27 738–27 752, Nov. 2016. doi: 10.1364/OE.24.027738

[19] B. E. Saleh and M. C. Teich, *Fundamentals of photonics.* john Wiley & sons, 2019.

[20] X. Chen, M. M. Milosevic, S. Stankovic, S. Reynolds, T. D. Bucio, K. Li, D. J. Thomson, F. Gardes, and G. T. Reed, "The emergence of silicon photonics as a flexible technology platform," *Proceedings of the IEEE*, vol. 106, no. 12, pp. 2101–2116, Dec. 2018. doi: 10.1109/JPROC.2018.2854372

[21] N. Izhaky, M. T. Morse, S. Koehl, O. Cohen, D. Rubin, A. Barkai, G. Sarid, R. Cohen, and M. J. Paniccia, "Development of cmos-compatible integrated silicon photonics devices," *IEEE Journal of Selected Topics in Quantum Electronics*, vol. 12, no. 6, pp. 1688–1698, 2006.

[22] M. Rouviere, M. Halbwax, J.-L. Cercus, E. Cassan, L. Vivien, D. Pascal, M. Heitzmann, J.-M. Hartmann, and S. Laval, "Integration of germanium waveguide photodetectors for intrachip optical interconnects," *Optical Engineering*, vol. 44, no. 7, pp. 075 402–075 402, 2005.

[23] L. Colace and G. Assanto, "Germanium on silicon for near-infrared light sensing," *IEEE Photonics Journal*, vol. 1, no. 2, pp. 69–79, Aug. 2009. doi: 10.1109/JPHOT.2009.2025516

[24] A. Aliane, J. Ouvrier-Buffet, W. Ludurczak, L. André, H. Kaya, C. Vialle, M. Benwadih, V. Goudon, S. Becker, and J. Hartmann, "Fabrication and characterization of sensitive vertical pin germanium photodiodes as infrared detectors," *Semiconductor Science and Technology*, vol. 35, no. 3, p. 035013, 2020.

[25] V. Sorianello, L. Colace, N. Armani, F. Rossi, C. Ferrari, L. Lazzarini, and G. Assanto, "Low-temperature germanium thin films on silicon," *Optical Materials Express*, vol. 1, no. 5, pp. 856–865, Sep. 2011. doi: 10.1364/OME.1.000856

[26] M. Gould, T. Baehr-Jones, R. Ding, and M. Hochberg, "Bandwidth enhancement of waveguide-coupled photodetectors with inductive gain peaking," *Optics Express*, vol. 20, no. 7, pp. 7101–7111, Mar. 2012. doi: 10.1364/OE.20.007101

[27] A. Novack, M. Gould, Y. Yang, Z. Xuan, M. Streshinsky, Y. Liu, G. Capellini, A. E.-J. Lim, G.-Q. Lo, T. Baehr-Jones, and M. Hochberg, "Germanium photodetector with 60 GHz bandwidth using inductive gain peaking," *Optics Express*, vol. 21, no. 23, Nov. 2013. doi: 10.1364/OE.21.028387

[28] D. Wu, X. Hu, W. Li, D. Chen, L. Wang, and X. Xiao, "62 GHz germanium photodetector with inductive gain peaking electrode for photonic receiving beyond 100 Gbaud," *Journal of Semiconductors*, vol. 42, no. 2, p. 020502, Feb. 2021. doi: 10.1088/1674-4926/42/2/020502

[29] *Sentaurus Device User Guide. Version N-2017.09*, Synopsys, Inc., Mountain View, CA, Sep. 2017.

[30] T. Pinguet, S. Denton, S. Gloeckner, M. Mack, G. Masini, A. Mekis, S. Pang, M. Peterson, S. Sahni, and P. D. Dobbelaere, "High-volume manufacturing platform for silicon photonics," *Proceedings of the IEEE*, vol. 106, no. 12, Dec. 2018. doi: 10.1109/JPROC.2018.2859198

[31] R. Sabella, "Silicon photonics for 5G and future networks," *IEEE Journal of Selected Topics in Quantum Electronics*, vol. 26, no. 2, pp. 1–11, Mar./Apr. 2020. doi: 10.1109/JSTQE.2019.2948501

[32] J. Michel, J. Liu, and L. C. Kimerling, "High-performance Ge-on-Si photodetectors," *Nature Photonics*, vol. 4, no. 8, pp. 527–534, 2010. doi: 10.1038/nphoton.2010.157

[33] F. Boeuf, S. Crémer, E. Temporiti, M. Ferè, M. Shaw, C. Baudot, N. Vulliet, T. Pinguet, A. Mekis, G. Masini, H. Petiton, P. Le Maitre, M. Traldi, and L. Maggi, "Silicon photonics R&D and manufacturing on 300-mm wafer platform," *Journal of Lightwave Technology*, vol. 34, no. 2, pp. 286–295, Jan. 2016. doi: 10.1109/JLT.2015.2481602

[34] N. Margalit, C. Xiang, S. M. Bowers, A. Bjorlin, R. Blum, and J. E. Bowers, "Perspective on the future of silicon photonics and electronics," *Applied Physics Letters*, vol. 118, no. 22, p. 220501, May 2021. doi: 10.1063/5.0050117

[35] L. Colace, G. Masini, F. Galluzzi, G. Assanto, G. Capellini, L. Di Gaspare, E. Palange, and F. Evangelisti, "Metal-semiconductor-metal near-infrared light detector based on epitaxial Ge/si," *Applied Physics Letters*, vol. 72, no. 24, pp. 3175–3177, Jun. 1998. doi: 10.1063/1.121584

[36] L. Virot, L. Vivien, A. Polzer, D. Marris-Morini, J. Osmond, J. M. Hartmann, P. Crozat, E. Cassan, C. Baudot, C. Kopp *et al.*, "40 Gbit/s germanium waveguide photodetector on silicon," in *Silicon Photonics and Photonic Integrated Circuits III*, vol. 8431, 2012. doi: 10.1117/12.923854 p. 84310A.

[37] D. Benedikovic, L. Virot, G. Aubin, F. Amar, B. Szelag, B. Karakus, J.-M. Hartmann, C. Alonso-Ramos, X. L. Roux, P. Crozat, E. Cassan, D. Marris-Morini, C. Baudot, F. Boeuf, J.-M. Fédéli, C. Kopp, and L. Vivien, "25 Gbps low-voltage hetero-structured silicon-germanium waveguide pin photodetectors for monolithic on-chip nanophotonic architectures," *Photonics Research*, vol. 7, no. 4, pp. 437–444, Apr. 2019. doi: 10.1364/PRJ.7.000437

[38] Y. Zuo, Y. Yu, Y. Zhang, D. Zhou, and X. Zhang, "Integrated high-power germanium photodetectors assisted by light field manipulation," *Optics Letters*, vol. 44, no. 13, pp. 3338–3341, 2019.

[39] Y. Shi, Y. Zhang, Y. Wan, Y. Yu, Y. Zhang, X. Hu, X. Xiao, H. Xu, L. Zhang, and B. Pan, "Silicon photonics for high-capacity data communications," *Photonics Research*, vol. 10, no. 9, pp. A106–A134, Sep. 2022. doi: 10.1364/PRJ.456772

[40] C. G. Littlejohns, Y. Hu, F. Y. Gardes, D. J. Thomson, S. A. Reynolds, G. Z. Mashanovich, and G. T. Reed, "50 Gb/s silicon photonics receiver with low insertion loss," *IEEE Photonics Technology Letters*, vol. 26, no. 7, pp. 714–717, Apr. 2014. doi: 10.1109/LPT.2014.2303578

[41] E. Kasper and M. Oehme, "High speed germanium detectors on Si," *Physica Status Solidi C*, vol. 5, no. 9, pp. 3144–3149, 2008. doi: 10.1002/pssc.200779301

[42] M. de Cea, D. Van Orden, J. Fini, M. Wade, and R. J. Ram, "High-speed, zero-biased silicon-germanium photodetector," *APL Photonics*, vol. 6, no. 4, p. 041302, 2021. doi: 10.1063/5.0047037

[43] M. J. Byrd, E. Timurdogan, Z. Su, C. V. Poulton, D. Coleman, N. M. Fahrenkopf, T. N. Adam, G. Leake, D. D. Coolbaugh, and M. R. Watts, "Mode-evolution based coupler for Ge-on-Si photodetectors," in *2016 IEEE Photonics Conference (IPC)*, Waikoloa, HI, USA, Oct. 2016. doi: 10.1109/IPCon.2016.7831065

[44] J. Liu, J. Michel, W. Giziewicz, D. Pan, K. Wada, D. D. Cannon, S. Jongthammanurak, D. T. Danielson, L. C. Kimerling, J. Chen *et al.*, "High-performance, tensile-strained Ge p-i-n photodetectors on a Si platform," *Applied Physics Letters*, vol. 87, no. 10, p. 103501, Aug. 2005. doi: 10.1063/1.2037200

[45] C. Chang, X. Xie, T. Li, and J. Cui, "Configuration of the active region for the Ge-on-Si photodetector based on carrier mobility," *Frontiers in Physics*, vol. 11, p. 1150684, 2023. doi: 10.3389/fphy.2023.1150684

[46] Y. Zhu, Z. Liu, C. Niu, Y. Pang, D. Zhang, X. Liu, J. Zheng, Y. Zuo, H. Xue, and B. Cheng, "High-speed and high-power germanium photodetector based on a trapezoidal absorber," *Optics Letters*, vol. 47, no. 13, pp. 3263–3266, Jul. 2022. doi: 10.1364/OL.461673

[47] Y. Shi, X. Li, M. Zou, Y. Yu, and X. Zhang, "103 GHz germanium-on-silicon photodiode enabled by an optimized U-shaped electrode," *Photonics Research*, vol. 12, no. 1, pp. 1–6, Jan. 2024. doi: 10.1364/PRJ.495958

[48] J.-Y. Su, K.-F. Chung, S.-C. Kao, C.-H. Cheng, C.-T. Tsai, T.-H. Liu, H.-T. Cheng, C.-H. Wu, T.-T. Shih, D.-W. Huang, and G.-R. Lin, "Ge p-i-n photodiode as 60-Gbit/s optical NRZ-OOK data receiver," *Journal of Lightwave Technology*, vol. 40, no. 13, pp. 4326–4336, Jul. 2022. doi: 10.1109/JLT.2022.3161011

[49] A. Jungel, *Transport Equations for Semiconductors*, 1st ed. Heidelberg: Springer Berlin, 2019.

[50] G. Ghione, *Dispositivi per la microelettronica.* Milano: McGraw-Hill, 1998.

[51] D. L. Scharfetter and H. K. Gummel, "Large-signal analysis of a silicon read diode transistor," *IEEE Transactions on Electron Devices*, vol. ED-16, no. 1, pp. 64–77, Jan. 1969.

[52] P. A. Markowich, *The Stationary Semiconductor Device Equations*, ser. Computational Microelectronics. Wien: Springer-Verlag, 1986.

[53] C. Canali, G. Majni, R. Minder, and G. Ottaviani, "Electron and hole drift velocity measurements in silicon and their empirical relation to electric field and temperature," *IEEE Transactions on Electron Devices*, vol. 22, no. 11, pp. 1045–1047, Aug. 1975. doi: 10.1109/T-ED.1975.18267

[54] W. Yu, *Electromagnetic Simulation Techniques Based on the FDTD Method*, ser. Wiley Series in Microwave and Optical Engineering. Wiley, 2009. ISBN 9780470502037

[55] K. Yee, "Numerical solution of initial boundary value problems involving Maxwell's equations in isotropic media," *IEEE Transactions on Antennas and Propagation*, vol. 14, no. 3, pp. 302–307, May 1966. doi: 10.1109/TAP.1966.1138693

[56] *RSoft FullWAVE User Guide, v2019.09*, Synopsys, Inc., Optical Solutions Group, Ossining, NY, 2019.

[57] M. G. C. Alasio, M. Goano, A. Tibaldi, F. Bertazzi, S. Namnabat, D. Adams, P. Gothoskar, F. Forghieri, G. Ghione, and M. Vallone, "Ge-on-Si waveguide photodetectors: multiphysics modeling and experimental validation," in *21st International Conference on Numerical Simulation of Optoelectronic Devices (NUSOD 2021)*, online, Sep. 2021. doi: 10.1109/NUSOD52207.2021.9541424. ISBN 978-1-6654-4836-9 pp. 37–38.

[58] ——, "Bias effects on the electro-optic response of Ge-on-Si waveguide photodetectors," in *IEEE Photonics Conference*, online, Oct. 2021. doi: 10.1109/IPC48725.2021.9592968. ISBN 978-1-6654-4676-1

[59] M. G. C. Alasio, P. Franco, A. Tibaldi, F. Bertazzi, S. Namnabat, D. Adams, P. Gothoskar, G. Masini, F. Forghieri, G. Ghione, and M. Goano, "3D multiphysics transient modeling of vertical Ge-on-Si *pin* waveguide photodetectors," in *22nd International Conference on Numerical Simulation of Optoelectronic Devices (NUSOD 2022)*, online, Sep. 2022. doi: 10.1109/NUSOD54938.2022.9894739. ISBN 978-1-6654-7898-4 pp. 5–6.

[60] ——, “Optical power screening effects in Ge-on-Si vertical *pin* photodetectors,” in *Proceedings of SIE 2022. 53rd Annual Meeting of the Italian Electronics Society*, ser. Lecture Notes on Electrical Engineering, G. Cocorullo, F. Crupi, and E. Limiti, Eds. Cham, Switzerland: Springer Nature Switzerland AG, 2023, vol. 1005, pp. 155–159. ISBN 978-3-031-26065-0

[61] M. G. C. Alasio, M. Vallone, A. Tibaldi, S. Namnabat, D. Adams, P. Gothoskar, F. Forghieri, G. Masini, F. Bertazzi, G. Ghione, M. Gioannini, and M. Goano, “TCAD-assisted progress on the Cisco platform towards low-bias 200 Gbit/s vertical-*pin* Ge-on-Si waveguide photodetectors,” *Journal of Lightwave Technology*, vol. 42, no. 9, pp. 3269–3276, May 2024. doi: 10.1109/JLT.2024.3352437

[62] C. G. Van de Walle and R. M. Martin, “Theoretical calculations of heterojunction discontinuities in the si/ge system,” *Phys. Rev. B*, vol. 34, pp. 5621–5634, Oct 1986. doi: 10.1103/PhysRevB.34.5621

[63] A. Palmieri, M. Vallone, M. Calciati, A. Tibaldi, F. Bertazzi, G. Ghione, and M. Goano, “Heterostructure modeling considerations for Ge-on-Si waveguide photodetectors,” *Optical and Quantum Electronics*, vol. 50, no. 2, p. 71, Feb. 2018. doi: 10.1007/s11082-018-1338-y

[64] F. Gity, J. M. Hayes, B. Corbett, and A. P. Morrison, “Modeling the effects of interface traps on the static and dynamic characteristics of ge/si avalanche photodiodes,” *IEEE Journal of Quantum Electronics*, vol. 47, no. 6, pp. 849–857, 2011. doi: 10.1109/JQE.2011.2123872

[65] C. Masini, L. Calace, G. Assanto, H.-C. Luan, and L. Kimerling, “High-performance p-i-n ge on si photodetectors for the near infrared: from model to demonstration,” *IEEE Transactions on Electron Devices*, vol. 48, no. 6, pp. 1092–1096, 2001. doi: 10.1109/16.925232

[66] Y. Wei, X. Cai, J. Ran, and J. Yang, “Analysis of dark current dependent upon threading dislocations in ge/si heterojunction photodetectors,” *Microelectronics international*, vol. 29, no. 3, pp. 136–140, 2012.

[67] *Lightwave Component Analyzer application notes*, Keysight Technologies, Santa Rosa, CA, Dec. 2017.

[68] D. Benedikovic, L. Virot, G. Aubin, J.-M. Hartmann, F. Amar, B. Szelag, X. Le Roux, C. Alonso-Ramos, P. Crozat, É. Cassan, D. Marris-Morini, C. Baudot, F. Boeuf, J.-M. Fédéli, C. Kopp, and L. Vivien, “Comprehensive study on chip-integrated germanium pin photodetectors for energy-efficient silicon interconnects,” *IEEE Journal of Quantum Electronics*, vol. 56, no. 1, p. 8400409, Feb. 2020. doi: 10.1109/JQE.2019.2954355

[69] M. G. C. Alasio, M. Vallone, A. Tibaldi, F. Bertazzi, S. Namnabat, D. Adams, P. Gothoskar, F. Forghieri, G. Masini, G. Ghione, and M. Goano, “Modeling the frequency response of vertical and lateral Ge-on-Si waveguide

photodetectors: Is 3D simulation unavoidable?" in *2022 Conference on Lasers and Electro-Optics (CLEO)*, San Jose, CA, May 2022. doi: 10.1364/CLEO_AT.2022.JW3A.28. ISBN 978-1-957171-05-0 p. JW3A.28.

[70] M. G. C. Alasio, M. Zhu, A. Fronteddu, A. Cardinale, A. Ballarati, E. Bellotti, G. Ghione, A. Tibaldi, F. Bertazzi, M. Vallone, and M. Goano, "Modeling the electronic transport in FinFET-like lateral Ge-on-Si *pin* waveguide photodetectors for ultra-wide bandwidth applications," in *23rd International Conference on Numerical Simulation of Optoelectronic Devices (NUSOD 2023)*, Torino, Italy, Sep. 2023. doi: 10.1109/NUSOD59562.2023.10273560. ISBN 979-8-3503-1429-8 pp. 107–108.

[71] H. H. Silvestri, H. Bracht, J. L. Hansen, A. N. Larsen, and E. E. Haller, "Diffusion of silicon in crystalline germanium," *Semiconductor Science and Technology*, vol. 21, no. 6, p. 758, apr 2006. doi: 10.1088/0268-1242/21/6/008

[72] M. Cohen and J. Chelikowsky, *Electronic Structure and Optical Properties of Semiconductors*, ser. Springer Series in Solid-State Sciences. Springer Berlin Heidelberg, 2012. ISBN 9783642613388

Appendix A

Semiconductor modeling

An analytic model, even if approximate, is fundamental for understanding the relationships between quantities, even if the numerical approach proposed is more comprehensive and can be applied to more cases. Here, the basic definitions and concepts are reported.

Semiconductors are materials which have electrical properties between conductors and insulators. They can conduct under certain conditions or insulate in others.

Solid state physics is the foundation of this field, and the band structure, with the energy dispersion relation, describes the range of energy levels that electrons may have inside the lattice, for every k-vectors.

In most cases, two energy bands, namely the valence band and the conduction band, separated by the energy gap E_g, are enogh for the description of charge transport in low field conditions. Summarizing, this is an assumption of all the carriers to be located at the minimum o fthe conduction band, or the maximum of the valence band.

At room temperature, around $T = 300\,\mathrm{K}$, a portion of electrons have enough thermal energy to be promoted from the valence to the conduction band, leaving behind positive charges called holes.

Electron located at minimum of the conduction band and holes located at the maximum of the valence band, allow for the effective mass approximation to be used, and holds for quasi-thermodynamic equilibrium, or simply equilibrium

conditions. This model fit an effective mass for electrons and holes, with both carriers travelling in the lattice as if they have this effective mass. The effective mass can be derived from the energy dispersion relationship as

$$\frac{\partial^2 E}{\partial k^2} = \frac{1}{m_e} h^2 \tag{A.1}$$

This description provides an electron energy-momentum relation that fully characterizes the semiconductor's electronic band structure. Possible methods to evaluate the band structure of a semiconductor can be found in [72]. Fig. A.1 reports an example of the band structure of a diamond.

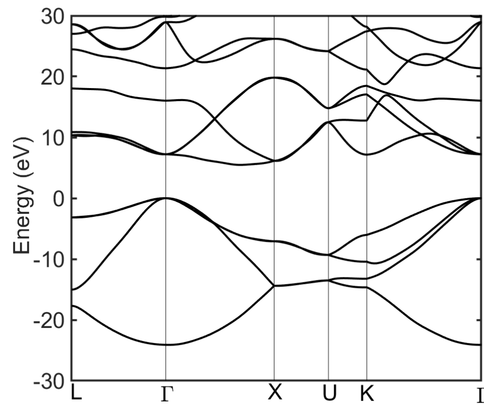

Fig. A.1 Electronic band structure of diamond, evaluated with DFT.

Under conditions of low energy, the majority of electrons and holes occupy the lowest point of the conduction band (E_c) and the highest point of the valence band (E_v), respectively. These points, along with their adjacent points, can be approximated using a parabolic function, which is known as the effective mass approximation.

The number of states per unit volume for electrons in the conduction band is denoted as N_c, and the number of states per unit volume for holes in the valence band is denoted as N_v. Both of these quantities are dependent on the energy level. Fig. A.2 shows a qualitative behavior of the density of states.

In a bulk semiconductor, it can be shown that

$$N_c(E) = \frac{4\pi}{h^3} \left(2m^*_{n,D}\right)^{3/2} \sqrt{E - E_c}, \tag{A.2}$$

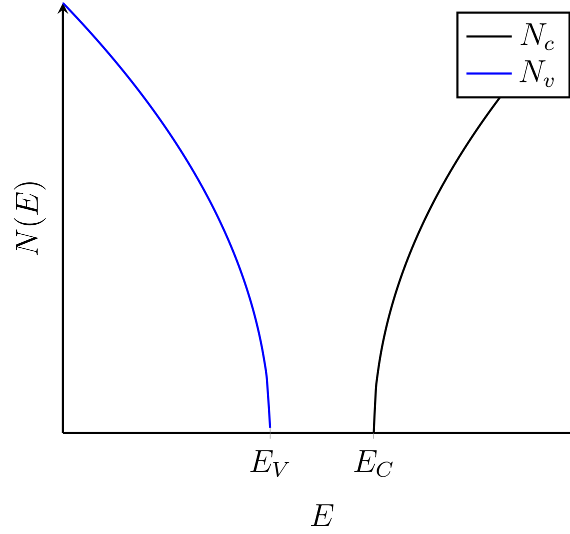

Fig. A.2 Qualitative plot of the dependence of the density of states with respect to energy.

$$N_v(E) = \frac{4\pi}{h^3}\left(2m^*_{h,D}\right)^{3/2}\sqrt{E_v - E}. \tag{A.3}$$

At equilibrium, electrons and holes follow the Fermi-Dirac distribution, which describes the occupation of electrons and holes in equilibrium.

$$f_n(E) = \frac{1}{1 + \exp\left(\frac{E - E_F}{k_B, T}\right)} \tag{A.4}$$

$$f_h(E) = \frac{1}{1 + \exp\left(\frac{E_F - E}{k_B T}\right)}, \tag{A.5}$$

Fig. A.3 shows the Fermi-Dirac distribution for two distinct temperatures, for both electrons and holes.

In the electron Fermi-Dirac distribution, at $T = 0\,\mathrm{K}$ electrons do not have sufficient energy above the Fermi level E_F. While increasing temperature, the probability to find electrons with energy above the Fermi level (i.e. in the conduction band) increases. The same applies to holes.

Now, it is possible to define the carrier concentration n and p, multiplying the density of states and the Fermi-Dirac distributions, integrating over the energy:

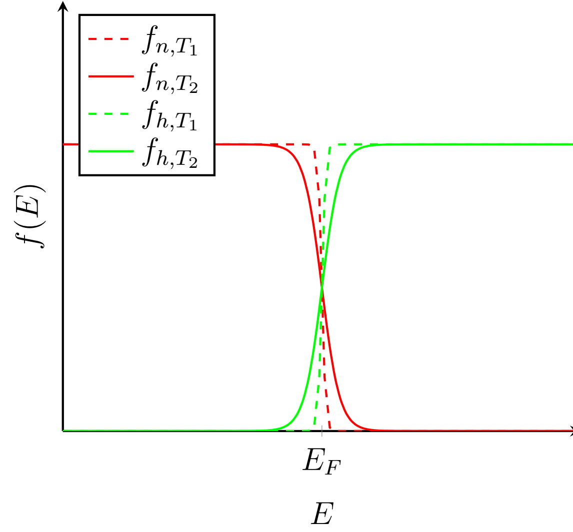

Fig. A.3 Fermi-Dirac Statistic for electrons with different temperature as a function of the difference between the energy of the particle and the Fermi level E_F.

$$n = \int_{E_c}^{\infty} N_c(E) f_n(E) \mathrm{d}E, \tag{A.6}$$

$$p = \int_{-\infty}^{E_v} N_v(E) f_h(E) \mathrm{d}E, \tag{A.7}$$

with integral domain starting from the edge of the corresponding band for both n and p. In other words Eq. (A.6) and Eq. (A.7) are the product of the all possible states and the probability that those states are occupied.

n and p describe by means of densities (or concentration) electrons and holes in the semiconductor, typically in cm^{-3}. Electrons and holes then interacts with different phenomena, like an externally applied voltage, photons or phonons.

Eq. (A.6) and Eq. (A.7) do not have a analytic solution, so either a numerical solution or an approximation must be used.

If the semiconductor is not degenerate, i.e. if the Fermi level is away from the band edges, within the energy gap, the Fermi-Dirac distribution can be approximated with the Boltzmann approximation:

$$f_n(E) \underset{E \gg E_F}{\approx} \exp \frac{E_F - E}{k_B T}, \tag{A.8}$$

$$f_h(E) \underset{E \ll E_F}{\approx} \exp\left(\frac{E - E_F}{k_B T}\right). \tag{A.9}$$

and Eq. (A.8) and Eq. (A.9) substituting in Eq. (A.6) and Eq. (A.7)

$$n = \int_{E_c}^{\infty} N_c(E) f_n(E) \mathrm{d}E = N_c \exp\left(\frac{E_F - E_c}{k_B T}\right) \tag{A.10}$$

$$p = \int_{-\infty}^{E_v} N_v(E) f_h(E) \mathrm{d}E = N_v \exp\left(\frac{E_v - E_F}{k_B T}\right) \tag{A.11}$$

with effective density of states defined as

$$N_c = 2\frac{\left(2\pi m^*_{n,D} k_B T\right)^{3/2}}{h^3}, \tag{A.12}$$

$$N_v = 2\frac{\left(2\pi m^*_{h,D} k_B T\right)^{3/2}}{h^3}. \tag{A.13}$$

An undoped semiconductor is defined intrinsic, and at equilibrium, electron and holes have the same concentrations, due to neautrality, leading to $p = n = n_i$. So

$$n_i = N_c \exp\left(\frac{E_{Fi} - E_c}{k_B T}\right) = p_i = N_v \exp\left(\frac{E_v - E_{Fi}}{k_B T}\right). \tag{A.14}$$

Fig. A.4 shows a plot of the silicon intrinsic carrier density as a function of the temperature.

A semiconductor can be doped, a process that substitutes lattice atoms with other elements of the periodic table, that can donate (donor dopants) or accept (acceptor dopants) a charge to the semiconductor. Donors density is denoted by N_D and the extra electron is weakly bounded to the donor atom and easily ionized to contribute to electrons in the conduction band. This semiconductor is called n-type. Acceptors concentration is denoted by N_A, with opposite behaviour with respect to donors capturing electron from the valence band generateing a hole. This semiconductor is called p-type.

Multiplying Eq. (A.8) and Eq. (A.9)

$$n_i p_i = n_i^2 = N_c N_v \exp\left(-\frac{E_g}{k_B T}\right). \tag{A.15}$$

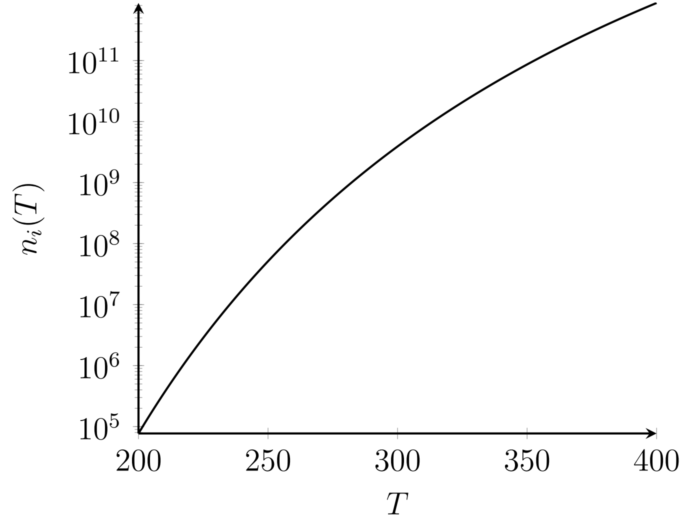

Fig. A.4 Intrinsic carrier density for Silicon as a function of the temperature

The *mass action law* states that, under equilibrium conditions, regardless of doping, the multiplication of the concentrations n and p remains unaffected by the position of the Fermi level.

$$np = n_i^2 \tag{A.16}$$

The Fermi level can be calculated using the expressions for electron and hole densities. In n-type semiconductors, the Fermi level increases with respect to E_{Fi}, becoming closer to the conduction band edge and for p-type semiconductors the Fermi level decreases and becomes closer to the valence band edge.

The concept of quasi-Fermi levels is introduced to describe the behavior of electron and hole concentrations. Instead of using a single Fermi level, two separate quasi-Fermi levels, denoted as E_{Fn} and E_{Fh}, are used. With these definitions, the derivation of all the quantities can be written as

$$f_n\left(E, E_{Fn}\right) = \frac{1}{1 + \exp\left(\frac{E-E_{Fn}}{k_B T}\right)}_{E \gg E_{Fn}}, \tag{A.17}$$

$$f_h\left(E, E_{Fh}\right) = \frac{1}{1 + \exp\left(\frac{E_{Fh}-E}{k_B T}\right)} \approx_{E \ll E_{Fh}}. \tag{A.18}$$

And using Boltzann approximation

$$f_n\left(E,E_{Fn}\right)\approx\exp\left(\frac{E_{Fn}-E}{k_BT}\right), \tag{A.19}$$

$$f_h\left(E,E_{Fh}\right)\approx\exp\left(\frac{E-E_{Fh}}{k_BT}\right). \tag{A.20}$$

leading to

$$n=N_c\exp\left(\frac{E_{Fn}-E_c}{k_BT}\right),\quad p=N_v\exp\left(\frac{E_v-E_{Fh}}{k_BT}\right), \tag{A.21}$$

Also the mass action law changes

$$np=n_i^2\exp\left(\frac{E_{Fn}-E_{Fh}}{k_BT}\right). \tag{A.22}$$

It is important to observe that the equilibrium case, when using the new quantity definitions, is simply a specific scenario. In this scenario, at equilibrium, the value of E_F remains constant throughout the defined region. This implies that if $E_{F,n}=E_{F,h}$, the semiconductor is in equilibrium.

In the presence of an applied field, the ensemble average velocity assumes a value proportional to the electric field:

$$\underline{v}_{n,av}=-\mu_n\underline{\mathcal{E}},\quad \underline{v}_{h,av}=\mu_h\underline{\mathcal{E}}. \tag{A.23}$$

where μ_n and μ_h are the electron and hole mobilities, measured in $\mathrm{cm}^2/\mathrm{Vs}$.

If the applied electric field is low with respect to the saturation electric field value, the mobility is called *low-field mobility* and it does not depends on the interaction with lattice vibrations (phonons), impurities etc. Typically, it decreases with increasing doping and increasing temperature. For very large electric fields (with values depending on the semiconductor) the average velocity saturates:

$$v_{n,av}\rightarrow v_{n,\,\mathrm{sat}}\ ,\quad v_{h,av}\rightarrow v_{h,\,\mathrm{sat}} \tag{A.24}$$

where the saturation velocities have magnitude around $10^7\mathrm{cm/s}$.

The motion of electrons and holes due to the presence of an electric field is called the drift motion and gives rise to the drift current density:

$$\begin{aligned} \underline{J}_{n,\mathrm{dr}} &= -qn\underline{v}_{n,av} = qn\mu_n\underline{\mathcal{E}}, \\ \underline{J}_{h,\mathrm{dr}} &= qp\underline{v}_{h,av} = qp\mu_h\underline{\mathcal{E}}. \end{aligned} \tag{A.25}$$

When a carriers concentration gradient is present, carriers tends to eliminate the gradient, leading to a diffusion current, that can be define as

$$\underline{J}_{n,\mathrm{d}} = qD_n\nabla n, \tag{A.26}$$

$$\underline{J}_{h,\mathrm{d}} = -qD_h\nabla p. \tag{A.27}$$

where D_n and D_h are the electron and hole diffusivities, respectively. At equilibrium the diffusivities and mobilities follow the Einstein relation $D_{n,p} = (k_BT/q)\,\mu_{n,p}$.

Appendix B

Optical generation rate

As described in the Synopsys manuals [29, 56], the optical generation rate is computed after the solution of the FDTD method converged. FDTD output consists of the electric and magnetic field $\vec{E}$ and $\vec{H}$ in steady state condition, with continuous wave illumination.

RSoft FullWave uses n and k values for each material,but defining the conductivity σ is useful for a simplified formula.

An absorbing medium is described by a complex refractive index $n = n' + jn'' = \sqrt{\varepsilon}$, and the light that propagates in this medium has a k-vector also complex given by:

$$\boldsymbol{k}^2 = n^2 \boldsymbol{k}_0^2 = (n' + jn'')^2 \boldsymbol{k}_0^2 = (\varepsilon' + j\varepsilon'') \boldsymbol{k}_0^2 \tag{B.1}$$

with vacuum wave vector $\boldsymbol{k}_0$.

But the k-vector can be written as

$$k^2 = \omega^2 \varepsilon \mu + j\omega\mu\sigma = \omega^2 \varepsilon \mu \left(1 + j\frac{\sigma}{\omega\varepsilon}\right) = k_0^2 \mu_\mathrm{r} \left(\varepsilon_\mathrm{r} + j\frac{\sigma}{\omega\varepsilon_0}\right) \tag{B.2}$$

and the complex refractive index is correctly modeled if you set:

$$\sigma = \frac{2\pi c_0 \varepsilon_0 \varepsilon''}{\lambda_0 \mu_\mathrm{r}} \tag{B.3}$$

with vacuum wavelength λ_0 and vacuum speed of light c_0 .

The absorbed power density is then derived from the time-averaged Poynting vector:

$$\boldsymbol{S}_{\mathrm{av}} = \frac{1}{2}\Re(\boldsymbol{E} \times \overline{\boldsymbol{H}}) \tag{B.4}$$

The intensity distribution corresponds to the magnitude of the Poynting vector $|S_{\mathrm{av}}|$. and the absorbed power density at each point is computed as:

$$W = -\nabla \cdot \boldsymbol{S}_{\mathrm{av}} = \frac{1}{2}\sigma|\boldsymbol{E}|^2 \tag{B.5}$$

The absorbed photon density is given by the absorbed power density divided by the photon energy. So, the optical carrier generation rate G_{opt} can be computed as:

$$G_{\mathrm{opt}} = \frac{W}{E_{\mathrm{ph}}} \tag{B.6}$$

with $E_{\mathrm{ph}} = hf$ being the photon energy.

A factor representing the quantum yield η can be atdded to Eq. (B.6), describing the average number of charge carriers generated by a single photon.

Appendix C

Material parameters

Table C.1 Material parameters for silicon and germanium in the drift-diffusion model

Parameter	Si		Ge	
	Electron	**Hole**	**Electron**	**Hole**
E_g (eV)	1.12		0.66	
χ (eV)	4.05		4.0	
ϵ_r	11.7		16.2	
μ ($\mathrm{cm^2/(V\,s)}$)	1350	480	3900	1900
τ_{SRH} (s)	10^{-5}	3×10^{-6}	10^{-5}	10^{-6}
C_{Auger} ($\mathrm{cm^6/s}$)	2.8×10^{-31}	10.1×10^{-32}	1.5×10^{-34}	1.05×10^{-32}
$C_{\mathrm{Radiative}}$ ($\mathrm{cm^3/s}$)	-		6.4×10^{-14}	

Table C.2 Wavelength, refractive index (n), and extinction coefficient (k) of Ge.

Wavelength (μm)	n **(Refractive Index)**	k
1.0300	4.4200	0.1230
1.1300	4.3850	0.1030
1.2400	4.3250	0.0810
1.4000	4.2380	0.0670
1.5500	4.2750	0.0057
1.6000	4.1730	0.0008
1.8000	4.1320	0.0000